

Geometry and topology of deformation band networks in wall damage zones and intersection damage zones

Master in Earth Science

Bjørn Martin Vika Gjesteland



Department of Earth Science

University of Bergen

June 2020

Abstract

This thesis presents an integrated analysis of deformation band networks within the Jurassic Navajo and Moab Member aeolian sandstones in the Colorado Plateau, SE Utah. Deformation bands are sub-seismic structures that commonly occur as interconnected networks in fault damage zones. Associated with permeability reductions, where a single band commonly displays 2-4 orders of magnitude reduction compared to the host rock, these sub-seismic structures may represent a significant controlling factor on effective permeability. Knowledge about the geometry, distribution, and connectivity of deformation bands is therefore crucial when predicting fluid flow patterns in subsurface reservoirs. This study quantifies deformation band network properties in intersection damage zones and wall damage zones outcropped in the Paradox Basin and in the San Rafael Swell.

A thorough topological analysis of deformation band networks was carried out to assess the connectivity and the characteristics of these networks. Topology is a method used for characterizing complex networks, here using endpoints and intersections to quantify the relationship between deformation bands in deformation band networks. The results show overall similar topological characteristics and high connectivity for deformation band networks in the two different damage zones with some significant observations; An increased strain can be associated with bifurcating, splaying, abutting, and shorter deformation bands, thus resulting in a high connectivity. Crossing deformation bands, however, rarely occur within a deformation band network, indicating that high strain causes deformation bands to overlap and link to form more connected networks. Moreover, observations demonstrate that short soft-linked deformation bands commonly develop within these high strain areas.

A detailed analysis of the spatial distribution of deformation bands in clusters reveal that the deformation bands intensity varies along clusters. Furthermore, quantitative analysis of orientation spread in deformation bands suggest that intersecting damage zones are more complex as they display a wider range in deformation band orientation compared to wall damage zones. This study revealed no clear correlation between increased deformation band intensity and orientation spread. The results do, however, support the theory that the formation of new clusters and maturation of already established clusters are more or less synchronic. Further supporting the theory that established damage zones grow through continual formation of deformation bands within the existing damage zone and outside the damage zone. This is presented in a model for the sequential growth of deformation band networks with emphasis on topology. The findings of this study can thus be of importance for predicting fluid flow patterns in subsurface reservoirs.

Acknowledgments

First and foremost, I would like to express my deepest gratitude to my main supervisor Prof. Atle Rotevatn (University of Bergen) for his unwavering guidance and insightful suggestions - both in the field, in the office, and on Zoom. I would like to extend my sincere thanks to my co-supervisor Prof. John Howell (University of Aberdeen) for his guidance in the field, and for providing virtual outcrop models. I am highly appreciative to my co-supervisor Assoc. Prof. David Peacock (University of Bergen) for practical suggestions regarding drone flying and for teaching me how to make virtual outcrop models. I am grateful for the opportunity to conduct fieldwork in Utah, and thus extend a great thanks to Wintershall DEA for funding this project.

I am grateful to Bjørn Nyberg and Casey Nixon for teaching me QGIS and NetworkGT. A special thanks to Bjørn for patient guidance and support in NetworkGT. In addition, I would like to extend my deepest appreciation to the IT department, and especially to Leo, for setting up and arranging remote desktop access, which has been invaluable during the strange situation resulting from the COVID-19 outbreak.

MSc Eivind Block Vagle and Ph.d. Sophie Behrendsen are thanked for good spirit in the field. Fruitful discussions with Eivind, in field and office, are highly appreciated as well as his dry-wit humour, which can light up any situation. I would like to extend my sincere thanks to Alma, Torgeir and Hugo for proofreading the thesis, and to Lise Nakken for continuous support, fruitful discussions and advice. Additionally, my fellow students in Grotten and Feltstyrke are thanked for great discussions, support and good atmosphere during the last year.

Finally, I would like to thank my family and non-academic friends for great support throughout these five years of study. Special thanks to Camilla for upholding my motivation and providing invaluable help in my thesis writing.

Contents

- 1 INTRODUCTION 1**
 - 1.1 RATIONALE 1
 - 1.2 AIMS AND OBJECTIVES 1
 - 1.3 STUDY AREA..... 2
- 2 GEOLOGICAL BACKGROUND 4**
 - 2.1 KEY TECTONIC ELEMENTS 4
 - 2.2 SALT VALLEY ANTICLINE: KLONDIKE BLUFFS FAULTS 6
 - 2.3 CHIMNEY ROCK FAULT ARRAY: BIG HOLE FAULT 7
 - 2.4 REGIONAL STRATIGRAPHY 8
 - 2.4.1 *Glen Canyon Group – Navajo Sandstone* 8
 - 2.4.2 *San Rafael Group – The Moab Member of the Curtis Formation*..... 9
- 3 THEORETICAL BACKGROUND 10**
 - 3.1 FAULT ZONES 10
 - 3.1.1 *Fault interactions* 11
 - 3.1.2 *Damage Zones and Classification* 11
 - 3.2 DEFORMATION BANDS 13
 - 3.2.1 *Mechanisms and host rock properties* 15
 - 3.2.2 *Deformation Band Classification*..... 16
 - 3.2.3 *Deformation bands and fluid flow* 21
 - 3.3 TOPOLOGY 21
- 4 DATA AND METHODOLOGY 24**
 - 4.1 DATA ACQUISITION: FIELDWORK 25
 - 4.2 DATA PROCESSING 27
 - 4.2.1 *Analysis of network topology using QGIS and NetworkGT* 27
- 5 RESULTS..... 32**
 - 5.1 KLONDIKE BLUFFS 32
 - 5.1.1 *Klondike West* 33
 - 5.1.2 *Klondike East*..... 39
 - 5.2 BIG HOLE FAULT 44
 - 5.2.1 *BC1 and BC2 clusters*..... 46
 - 5.2.2 *BC3 cluster* 52
- 6 DISCUSSION 56**
 - 6.1 GEOMETRICAL AND TOPOLOGICAL SIMILARITIES AND DIFFERENCES BETWEEN DEFORMATION BAND NETWORKS IN INTERSECTION DAMAGE ZONES AND WALL DAMAGE ZONES. 56
 - 6.2 SEQUENTIAL GROWTH OF DEFORMATION BAND NETWORKS 63
 - 6.3 HOW DOES THE TOPOLOGY OF A DEFORMATION BAND NETWORK COMPARE TO OTHER STRUCTURAL NETWORKS? 65
 - 6.4 IMPLICATIONS FOR FLUID FLOW 65
 - 6.5 THE APPLICABILITY OF TOPOLOGY IN WELL DATA ANALYSIS 68
- 7 CONCLUSIONS AND FURTHER WORK 69**
 - 7.1 CONCLUSIONS 69
 - 7.2 FURTHER WORK..... 70
- 8 REFERENCES..... 71**
- APPENDIX I: ABBREVIATIONS AND CALULATIONS IN NETWORKGT..... 78**
- APPENDIX II: GEOMETRICAL AND TOPOLOGICAL DATA..... 80**

1 Introduction

1.1 Rationale

Aeolian sandstone reservoirs can host a variety of structures that may affect fluid flow and subsurface reservoir performance. One such structure is deformation bands, which is a common type of strain localization in deformed, porous sandstones (e.g. Aydin & Johnson, 1978; Antonellini et al., 1994; Shipton & Cowie, 2001; Fossen et al., 2007). Deformation bands can occur as single bands, in clusters, or as networks (Aydin & Johnson, 1978; Schuller et al., 2013). The bands are known to alter the host rock properties and cause a reduction in permeability and porosity (e.g. Aydin & Johnson, 1978; Antonellini et al., 1994; Fossen & Bale, 2007). Several studies have focused upon the petrophysical properties and thickness variation of these bands with regards to fluid flow (e.g. Fossen & Bale, 2007; Rotevatn et al., 2013; Ballas et al., 2015). There is, however, a limited amount of studies that have thoroughly characterized the configuration and connectivity of these networks/zones, which can play a significant role in controlling the effective permeability in subsurface reservoirs (Rotevatn et al., 2013). Deformation band network properties can be quantified through topology analysis (Sanderson & Nixon, 2015), which is a method for quantifying the network properties of structural networks, and has recently gained traction (Manzocchi, 2002; Sanderson & Nixon, 2015; Morley & Nixon, 2016; Nyberg et al., 2018). Since there is limited knowledge about deformation band network properties, this study aims to quantify this by using a topological approach. This topological approach could lead to a better understanding of deformation band networks and how deformation bands grow and intersect within a network. Furthermore, it may add valuable insights to predictions of fluid flow in reservoirs.

1.2 Aims and objectives

The aim of this thesis is to increase the understanding of the *network properties* (node and branch topology, connectivity) of deformation band networks, with emphasis on networks within wall damage zones and intersection damage zones. For this purpose, a detailed study on deformation band networks in such damage zones was conducted on the Colorado Plateau, SE Utah (Fig. 1.1). The following objectives were set in order to achieve the aim stated above:

- Obtain high resolution outcrop photos of deformation band networks in intersection damage zones and wall damage zones.

- Use topological analysis to quantify the network properties of the studied deformation band networks using QGIS (an open-source GIS software) and NetworkGT (a plugin to QGIS for the analysis of network topology; see Nyberg et al., 2018).
- Quantify and discuss the variations in connectivity and topology of networks found in intersection damage zones and wall damage zones, and the implications thereof.

1.3 Study area

This study is focused in SE Utah (US), northwest on the Colorado Plateau (Fig. 1.1). The Colorado Plateau is a complex structural region that feature uplifts, depressions, faults and folds (e.g. Baker, 1935; Budnik, 1986; Hintze & Kowallis, 2009; Trudgill, 2011). The study was conducted in two different regions at the Colorado Plateau; wall damage zones were studied within the San Rafael Swell monocline, located approximately 30 km northwest of Green River. Intersection damage zones were studied at the southwestern flank of the collapsed crest of the Salt Valley Anticline, ca. 20 km southeast of Green River, in the Paradox Basin (Fig. 1.1). The studied structures are hosted in Jurassic aeolian sandstone units belonging to the Navajo Sandstone and Moab Member (Curtis Formation) (Fig. 2.3). The sandstones show exceptional exposures of deformation bands, which allow for detailed mapping of these. An elaboration on the geology of Utah and the key structural features of the study area are presented in the coming chapter (Chapter 2).

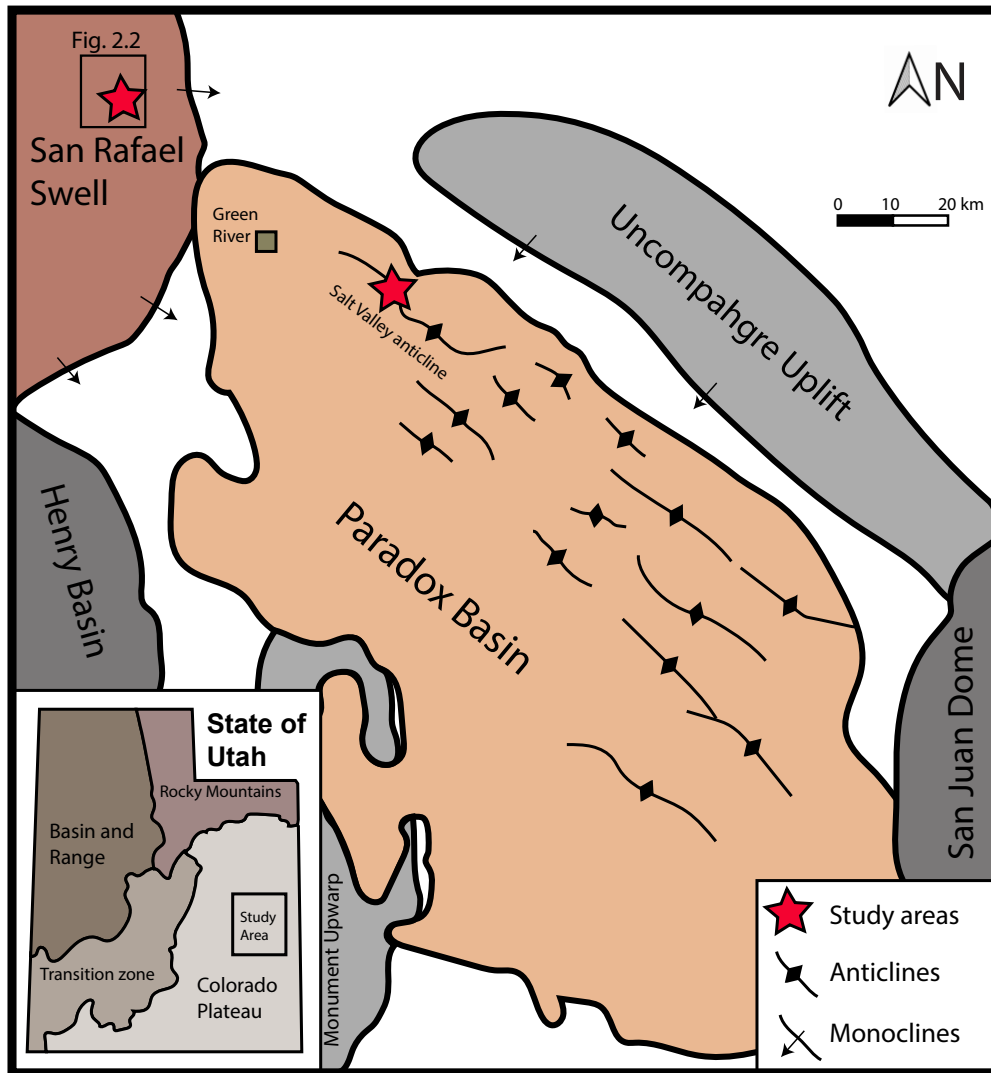


Figure 1.1: Inset map of Utah displaying the four main physiographic provinces and a simplified map of important structural elements surrounding the study area. Intersection damage zones are studied at the flank of the collapsed crest of the Salt Valley Anticline, while wall damage zones are studied within the San Rafael Swell. Modified from (Nuccio & Condon, 1996).

2 Geological Background

The state of Utah is comprised of four main physiographic provinces: (1) The Basin and Range Province, (2) Middle Rocky Mountains, (3) The Colorado Plateau, and (4) The Colorado and Basin and Range transition zone (Fig. 1.1) (Eaton, 1982; Morgan & Swanberg, 1985; Hintze & Kowallis, 2009; Trudgill, 2011). The Colorado Plateau forms the eastern part of Utah and extends into Arizona, Colorado and New Mexico. The stratigraphy of the plateau comprises rocks of Precambrian to Paleogene age (Hintze & Kowallis, 2009). This chapter introduces the geological framework and history of Utah with emphasis on the development of the Colorado Plateau, and key structural elements comprised in the Paradox Basin and San Rafael Swell, both situated in the NW Colorado Plateau (Fig. 1.1).

2.1 Key tectonic elements

A major control on the structural setting seen today in the Colorado Plateau can be dated back to the Palaeozoic era and the formation of the Ancestral Rockies, a series of intracratonic basement uplifts shaped by the collision and suturing of North America and South America-Africa (Kluth, 1986; Hintze & Kowallis, 2009). The orogenic event resulted in a number of uplifted intracratonic blocks and accompanying basins (e.g. Budnik, 1986; Barbeau, 2003). The Uncompahgre uplift and the Paradox Basin, east on the Colorado Plateau are examples of this configuration (Fig. 1.1)

The Paradox Basin, in which one of the study areas of this thesis is located, is an elongated, intracratonic basin trending dominantly northwest (Fig. 1.1). The basin boundaries are determined by the extent of the salt-rich Paradox Member of Mid-Pennsylvanian age, which is the source to extensive halokinesis (salt tectonism) in the area (Hite, 1968; Baars & Stevenson, 1981; Hintze & Kowallis, 2009; Trudgill, 2011). Several salt walls, salt diapirs and salt-cored anticlines are located within the Paradox Basin (Fig. 1.1) (Hite, 1968; Doelling et al., 2002; Trudgill, 2011). The halokinesis initiated in mid-Pennsylvanian times, shortly after deposition of the Paradox Member (Hintze & Kowallis, 2009; Trudgill, 2011). Increased uplift rate of the Uncompahgre uplift in Late Pennsylvanian and Early Permian increased the sediment supply and thereby increased the loading of the underlying mobile salt, causing the gradual growth of salt structures. Halokinetic movement within the Paradox Basin is thus closely linked to pulses of uplift of the Uncompahgre uplift (Elston et al., 1962; Trudgill, 2011). Today, the anticlines

within the basin strike roughly northwest, parallel with the Uncompahgre uplift (Fig. 1.1) (Trudgill, 2011).

Stevenson & Baars (1986) defined the Paradox Basin as a pull-apart basin of Pennsylvanian age, while more recent studies define the Paradox Basin as an immobile foreland basin, as a result of flexural subsidence in the footwall, influenced by loading of the uplifted crystalline Uncompahgre block (Barbeau, 2003; Trudgill, 2011). Later tectonic events have altered the basin geometry, in particular the development of the North American Cordillera, which can be defined as a series of overlapping orogenies formed by repeated collisions of island arc systems and micro continents during the Mesozoic to Paleogene (Armstrong, 1968; Dickinson, 2004; Hintze & Kowallis, 2009). The shape and extent of the North American Cordillera is influenced by the geometry of the steep subducting slab along the western margin of North America (Dumitru et al., 1991; Hintze & Kowallis, 2009). The subduction zone initiated as the North American continental plate collided with the oceanic Farallon plate in the Late Jurassic (Hintze & Kowallis, 2009). Throughout the Mesozoic, the dip of the subducting slab decreased, causing deformation to reach further inland, forming the Laramide orogeny. Basement faults were reactivated, and major monoclines across the Colorado Plateau formed, including the San Rafael Swell (Fig. 1.1) (Dickinson, 2004; Sundal et al., 2017).

The San Rafael Swell, where the second study area is located, is a 120 km long and 50 km wide monocline located northwest of the Paradox Basin (Fig. 1.1) (Johnson & Johnson, 2000). The east-vergent monoclinical flexure formed during fault-propagation folding above basement-rooted thrusts induced by the emerging Laramide orogeny in Late Cretaceous to Palaeogene times (e.g. Baker, 1935; Maerten, 2000; Hintze & Kowallis, 2009; Zuluaga et al., 2014; Sundal et al., 2017).

Overall tectonic quiescence the past 50 million years was interrupted by major uplift of the Colorado Plateau relative to the Basin and Range Province in the Cenozoic (Morgan & Swanberg, 1985; Spencer, 1996). The uplift caused erosion of Late Jurassic to Holocene strata across the Paradox Basin (Hintze & Kowallis, 2009).

2.2 Salt Valley Anticline: Klondike Bluffs faults

Salt Valley Anticline is a NW-trending breached asymmetric diapiric anticline situated at the northeastern edge of the Paradox Basin (Fig. 2.1) (Nuccio & Condon, 1996; Doelling et al., 2002; Trudgill, 2011). The flanks expose sedimentary rocks of Jurassic and Cretaceous age, such as the aeolian Entrada Sandstone and the aeolian Moab Member of the Curtis Formation (Elston et al., 1962; Cruikshank & Aydin, 1995; Hanke et al., 2018). The faults and deformation bands situated on the flanks are related to crestal collapse of salt walls (e.g. Randles et al., 2012). Klondike Bluffs is an area located on the southwest limb of Salt Valley anticline, dominated by cross-cutting NE- and SW-striking normal faults (the Klondike Bluffs faults; see Fig 2.1). Networks of deformation bands in the damage zones associated with two fault intersections are studied in this area (see Chapter 5).

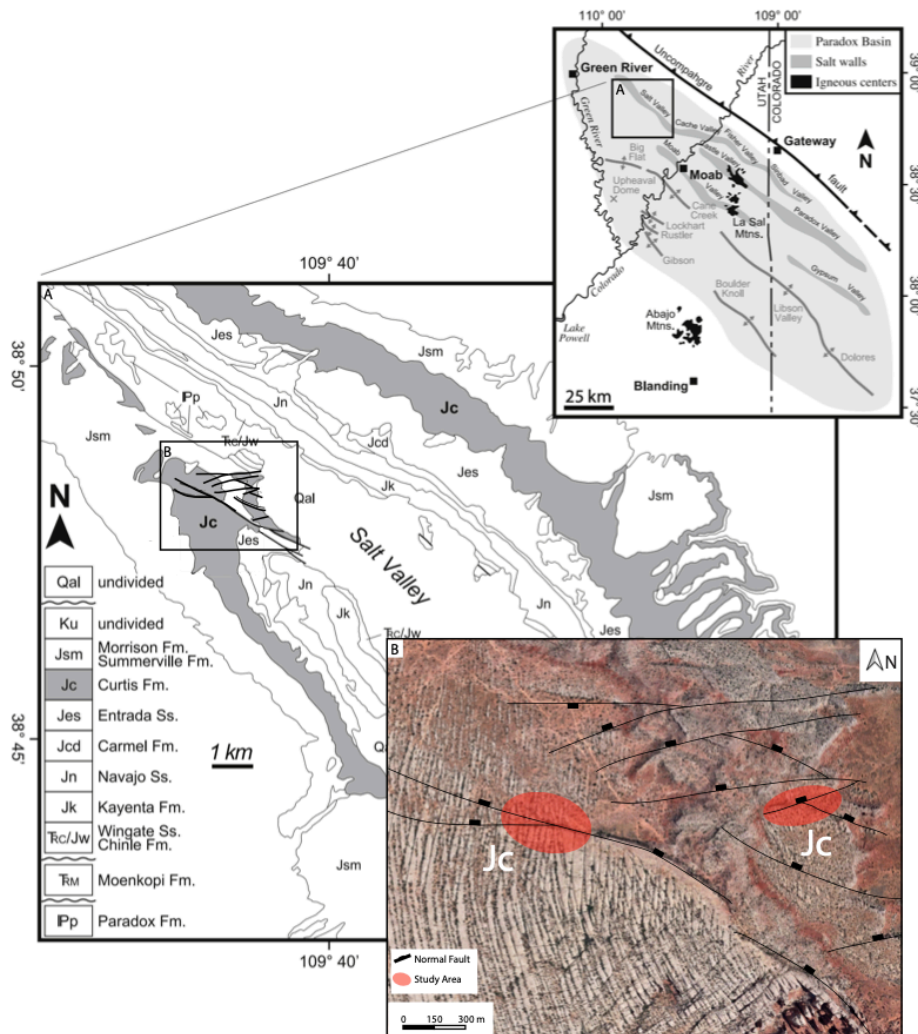


Figure 2.1: Geological map of the Paradox Basin, eastern Utah, with an inset of the Salt Valley anticline in A). Main structural features are included, and the areas where the Curtis Formation outcrops are shown in darker colour. Modified from Hanke et al. (2018). In B) is a zoom in on the Klondike Bluffs east and west study areas highlighting the main faults and the studied fault intersections in red. Aerial photo from Google Earth.

2.3 Chimney Rock Fault array: Big Hole Fault

The Chimney Rock Fault array is located in the northeastern part of the San Rafael Swell (Maerten, 2000; Shipton, 1999) (Fig. 1.1 and Fig. 2.2). The array comprises sets of cross-cutting WSW- and WNW-striking normal faults with oppositely dipping fault pairs arranged in an orthorhombic geometry that accommodate N-S extension (Krantz, 1988; Shipton & Cowie, 2001). The origin of the fault array is uncertain, but is likely related to the uplift of San Rafael Swell (Shipton & Cowie, 2001; Shipton et al., 2002). Shipton (1999) suggests that faulting may have been caused by extension parallel to the fold axis in regions of maximum plunge, possibly at depths between 1.5 and 3.0 km.

Two distinct fault architectures are recognized in the Chimney Fault Array: (1) faults formed by deformation bands, and (2) faults formed by shearing of joints and splay jointing. The WSW striking faults initially developed by the formation of deformation bands, while joint-based faulting dominates fault development along WNW striking faults. The normal faults vary between 100 m to 6 km in length. One of the study areas in this thesis is the WSW striking Big

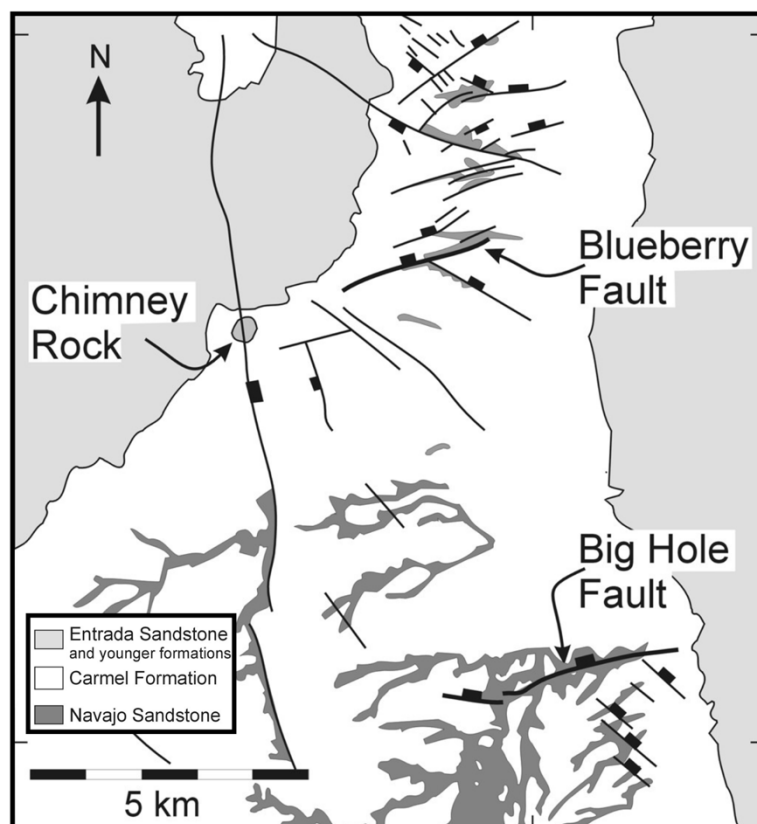


Figure 2.2: The Chimney Rock Fault Array with its characteristic cross-cutting fault sets. Located on the NE flank of the San Rafael Swell. The Big Hole Fault represents the southernmost fault in the fault array. Modified from Shipton & Cowie (2001). For position of figure, see Fig. 1.1.

Hole Fault, which is the southernmost fault in the Chimney Fault Array (Fig. 2.2). The fault is 4.1 km long and cut the aeolian Navajo Sandstone (Krantz, 1988; Maerten, 2000; Shipton & Cowie, 2001; Shipton et al., 2002). More detailed structural configurations for the Big Hole Fault are presented in the results (Chapter 5).

2.4 Regional Stratigraphy

The oldest rocks comprised in the Colorado Plateau geological province are granites and metamorphic rocks of Pre-Cambrian age exposed in the Uncompahgre uplift (Case, 1991). In the Paradox Basin, the exposed stratigraphic sequence comprises sedimentary rocks ranging in age from Carboniferous to Quaternary (Hintze & Kowallis, 2009; Trudgill, 2011). The sediments reflect a dominantly continental depositional environment, with the exception of Pennsylvanian and Cretaceous stratal units, which are of marine origin (Nuccio & Condon, 1996; Doelling et al., 2002; Trudgill, 2011). Characteristic for the area are the Jurassic cliff-forming sandstones outcropped in scenic rock formations. The Early Jurassic depositional sequence mainly consists of non-marine sandstones laid down in an arid continental basin that formed a depression between the Meso-Cordilleran High in central Utah and the remnants of the Ancestral Rockies in western Colorado (Hintze & Kowallis, 2009). The massive aeolian units are stratigraphically termed the Wingate, Navajo and Entrada formations (Fig. 2.3) (Hintze & Kowallis, 2009). This study targets the Navajo sandstone and the Moab Member of the Curtis Formation.

2.4.1 Glen Canyon Group – Navajo Sandstone

Early Jurassic sandstones of the Glen Canyon Group are subdivided into three formations: (1) the aeolian Wingate Formation, (2) the fluvial Kayenta Formation, and (3) the aeolian Navajo Sandstone (Fig 2.3), the latter of which is one of the key units hosting studied faults and deformation bands. Characteristic for the aeolian derived Navajo Sandstone are highly porous (20-25%) medium-grained arenite sandstones, arranged in large scale cross-beds (Freeman & Visser, 1975; Shipton & Cowie, 2001; Fossen et al., 2011). The colouration of the units is often red but varies from grey to light brown in the San Rafael Swell (Shipton & Cowie, 2001; Hintze & Kowallis, 2009). The sandstones were deposited in large windblown dunes in Lower to Middle Jurassic, when a widespread desert occupied large parts of the North American continent (Hintze & Kowallis, 2009). The Navajo Sandstone is overlain by the shallow marine Carmel Formation of the San Rafael Group (Fig. 2.3).

2.4.2 San Rafael Group – The Moab Member of the Curtis Formation

The eastern extent of the San Rafael Group (Fig 2.3) is comprised of (1) the tidally deposited Carmel Formation (Dewey Bridge Member); (2) the aeolian Entrada Sandstone (Slick Rock Member), characterized by alternating dune and interdune flat deposits; and (3) the Moab Member of the Curtis Formation (Doelling et al., 2002; Hintze & Kowallis, 2009). The Moab Member (previously part of the Entrada Sandstone) is one of the key units hosting the studied faults and deformation bands (Doelling et al., 2002). It comprises the aeolian derived sandstones outcropped in Klondike Bluffs, ranging in thickness from 18-30 m. The massive, cliff-forming sandstones are predominantly fine to medium grained, porous (20-25%), calcareous, and varying in colouration from pale-orange, grey, yellowish-brown to light-grey. Low-angle cross-stratification and intensive jointing are commonly observed in outcrops (Antonellini & Ayidin, 1994; Johansen et al., 2005). The Moab Member was deposited as coastal sand dunes on the southern and eastern margin of the restricted Jurassic seaway (Blakey, 1989; Crabaugh & Kocurek, 1993).

AGE		FORMATIONS AND MEMBERS	DEPOSITIONAL ENVIRONMENT	LITHOLOGY
CRETACEOUS	Mancos Shale	Upper shale member (Blue Gate Member)	Marine	
		Ferron Sandstone Member		
		Tununk Shale Member		
JURASSIC	Cedar Mtn. and Morrison Fms	Dakota Sandstone	Mixed continental, lacustrine, fluvial	
		Cedar Mtn. Fm		
		Brushy Basin Member		
		Salt Wash Member		
		Tidwell Member		
	San Rafael Group	Summerville Formation	Aeolian dune	
		Curtis Fm. Moab Member		
		Entrada Sst Slick Rock Member		
	Glen Canyon Group	Upper Carmel Dewey Bridge	Intertidal?	
		Lower Carmel		
Navajo Sandstone		Aeolian dune and interdune		
TRIASSIC		Kayenta Formation	Sandy fluvial systems	
		Wingate Sandstone	Aeolian dune and interdune	
		Chinle Formation	Alluvial plain deposits with soil horizons, and stream channels	
		Moenkopi Formation	Marine/terrestrial shallow near shore, tidal flats, flood plains	

Figure 2.3: Stratigraphic column of Triassic to Cretaceous in the northern Paradox Basin. Highlighting (red) studied units, coupled with depositional environment and lithology. Modified from Trudgill (2011).

3 Theoretical background

This chapter provides an introduction to the theory, which forms the foundation of this study. Before presenting the results and the methodological approach, it is important to understand the subsisting knowledge on deformation bands and their characteristics, and also understand the locus in which these commonly occur. An introduction to structural setting is thus provided in this chapter. The concept of topology analysis, which is the main applied methodology in this study, is also presented.

3.1 Fault Zones

A fault zone in the brittle domain can be subdivided into two distinct components: The fault core, which is a high-strain zone where most of the displacement is accommodated, and the enveloping low-strain zone. The latter is related to the growth and evolution of the fault and is more commonly termed the damage zone (e.g. Sibson, 1977; Caine et al., 1996; Peacock et al., 2000; Childs et al., 2009). The damage zone is characterized by a number of discrete structures, such as joints, fractures, deformation bands, and minor faults (e.g. Caine et al., 1996; Mollema & Antonellini 1999; Kim et al., 2004; Rotevatn et al., 2016). The width of the damage zone is determined by the frequency distribution of discrete structures. Commonly, the frequency distribution decreases with distance away from the fault core. The area where the frequency distribution drops down to a minimum defines the outer boundary of the damage zone (e.g. Chester & Logan, 1986; Beach et al., 1999; Kim et al., 2004; Gudmundsson et al., 2010).

The scaling relationship between fault displacement and damage zone thickness is in general positive (e.g. Evans, 1990; Beach et al., 1999; Fossen & Hesthammer, 2000; Shipton & Cowie, 2003). However, plots often show a scattered distribution (Cowie & Scholz, 1992; Choi et al., 2016). A considerable amount of studies have looked at the statistical variability and point to a variety of different parameters affecting the data, such as lithology, diagenesis, structural setting, depth of faulting, fault size, damage zone architecture, and deformation mechanisms (e.g. Evans, 1990; Cowie & Scholz, 1992; Fossen & Hesthammer, 2000; Berg & Skar, 2005; Torabi & Berg, 2011). However, the scattered distribution is still poorly understood. Choi et al. (2016) emphasize the importance of defining the width of the damage zone, suggesting that the inconsistencies may be caused by different ways of defining the width of the damage zone. Faults are though rarely single features, but most often sets of fault segments, which link up to

form more extensive fault zones (e.g. Pollard & Aydin, 1984; Biddle & Christie-Blick, 1985; Peacock & Sanderson, 1991; Fossen et al., 2005; Rotevatn et al., 2007; Fossen et al., 2016). The areas where fault segments are interacting are more complex when it comes to the rate of displacement, stress field, and the attributes of the resulting damage zone (Segall & Pollard, 1980; Fossen et al., 2005).

3.1.1 Fault interactions

The evolution from overstepping faults to linkage involves strain accumulation and development of several discrete structures, such as fractures and deformation bands, commonly with different orientation patterns from those seen farther from fault interactions (Fossen et al., 2005; Fossen & Rotevatn, 2016). Fault tips and fault interaction points are associated with stress increase and stress perturbation, which can explain the rotation of discrete structures (e.g. Segall & Pollard, 1980; Childs et al., 1995; Johansen et al., 2005; Fossen et al., 2005). Faults are commonly found in sets or networks, with faults abutting, splaying, and crossing, resulting in different types of damage zones (e.g. Duffy et al., 2015; Peacock et al. 2017b).

3.1.2 Damage Zones and Classification

Damage zones develop as a result of fault initiation, propagation, linkage, and displacement accumulation (Peacock, 2002; Shipton & Cowie, 2003; Fossen et al., 2005; Faulkner et al., 2011). Damage zones exist at a range of different scales and still show very similar geometries (Kim & Sanderson, 2006; Faulkner et al., 2011). Kim et al. (2004) provide a general classification of damage zones, dividing these into three main zones based on their location: the tip damage zone, linking damage zone, and the wall damage zone. Although the classification is based on a study of strike-slip faults it can be further extended to normal and reverse faults (Kim et al., 2004). Peacock et al. (2017a) suggest interaction damage zones as a broader term for linkage damage zones and further subdivide interaction damage zones in approaching- and intersecting damage zones (Fig. 3.1).

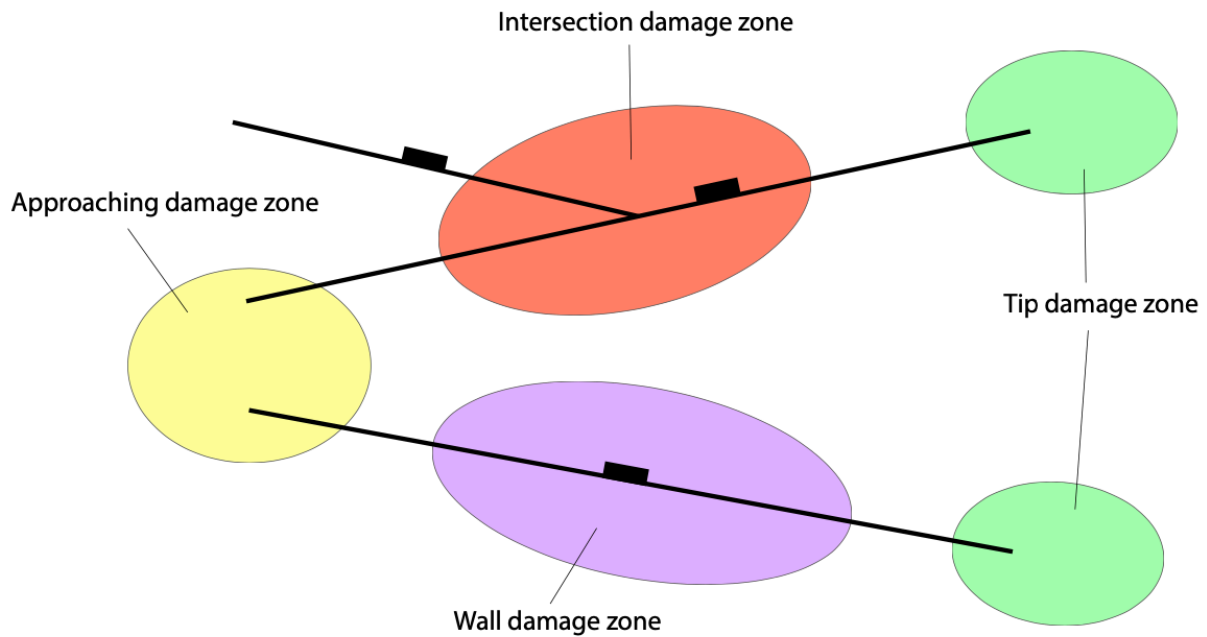


Figure 3.1: Conceptual presentation of the different types of damage zones forming around faults. Terminology from Kim et al. (2004) and Peacock et al. (2017a).

The approaching damage zone is the area of deformation caused by two or more faults that kinematically interact, without intersecting, whereas an intersection damage zone encompasses the deformation around the intersection point of two or more faults (Fig.3.1) (Peacock et al., 2017b). An intersection point is where a fault cross-cut, abuts or displace an older fault (Horsfield, 1980; Fossen et al., 2005). However, it is important to consider the 3D geometry of an interaction damage zone, as an approaching damage zone seen in outcrop can possibly be intersecting elsewhere on the fault plane (e.g. Walsh et al., 2003; Peacock et al., 2017a). It is further emphasised that different damage zones can overlap; a fault tip damage zone can for example develop into an interaction damage zone as a result of fault propagation (Kim et al., 2004; Choi et al., 2016; Peacock et al., 2017a).

The tip damage zone is the area of deformation surrounding the tip of a fault, resulting from higher stress concentration at the fault tip of a growing fault (e.g. Cowie & Scholz, 1992b; Shipton & Cowie, 2003). A tip damage zone, also known as the process zone, evolve from fault initiation and propagation (e.g. Vermilye & Scholz, 1998; Kim et al., 2004). McGrath & Davison (1995) document that strike-slip and thrust faults produce a more variable damage zone geometry compared to normal fault tip damage zones. Thus, two main types of fault tip

damage zones can be recognized: (1) Branching fractures from the fault tip, and (2) en-echelon array of fractures, disconnected from the fault tip. Kim et al. (2004) propose a subdivision of tip damage zones based on slip mode, distinguishing between mode II and mode III tip damage zones, and a mixed slip mode. Mode II tip damage zones are typically asymmetrical with horsetail fractures, wing cracks, antithetic faults, and synthetic faults, with both contraction and extensional zones across the fault trace. Mode III fault tip damage zones are typically symmetrical with synthetic and antithetic faults (Kim et al., 2004). Choi et al. (2016) highlight the importance of considering the relationship between slip mode and the location of damage zone structures around the fault tip, as the 3D architecture of damage zone structures can bring forward important information about fault evolution and propagation (e.g. Childs et al., 1995).

The wall damage zone is the damaged area caused by either fault propagation or increased slip on a fault (Peacock et al., 2017a). The wall damage zone can be situated along the whole fault trace and include structures, such as extensional fractures, antithetic and synthetic faults, rotated fault blocks, and deformation bands (Kim et al., 2004; Shipton & Cowie, 2001). A common internal feature for damage zones in high porosity sandstones are deformation bands (Fossen et al., 2007).

3.2 Deformation bands

Deformation bands are common structures in porous sandstones formed by localized shear and/or volume change in mm to cm thick tabular zones (e.g. Aydin, 1978; Antonellini et al., 1994; Fossen & Bale, 2007; Rotevatn et al., 2016). These structural features were first described by Aydin (1978), and has since been extensively studied, especially in sandstones. In the past two decades, deformation bands formed in carbonates and volcanoclastics have gained more attention (e.g. Wilson et al., 2003; Evans & Bradbury, 2004; Tondi et al., 2006; Rath et al., 2011; Cavailhes & Rotevatn, 2018). This thesis focus on deformation bands in siliciclastic rocks. Deformation bands in carbonates and volcanoclastics will therefore not be further addressed.

Deformation bands can occur as single structures, clusters, or networks of individual bands (Aydin & Johnson, 1978) (Fig. 3.2). The growth from single bands to swarms of bands is associated with strain hardening mechanisms (Aydin, 1978). Strain in high porosity sandstones is accommodated by the formation of deformation bands, whereas strain in low porosity rocks

is associated with extensional fractures or slip surfaces (Fossen et al., 2007). Deformation bands do not develop any discrete slip surface and form relatively small offsets (mm to dm) compared to their length (Fossen & Hesthammer, 1997). Furthermore, the formation of these alter the permeability and porosity of the host rock, commonly causing a reduction in porosity and permeability (one to six orders of magnitude) and an increased cohesion (Fossen et al., 2007). This places deformation bands in a separate category relative to faults and fractures, which commonly contribute to increased permeability and porosity (Aydin & Johnson, 1978; Aydin & Johnson, 1983; Antonellini et al., 1994; Fossen & Bale, 2007).

Field observations document how faults form in or along deformation band zones (e.g. Aydin & Johnson, 1978; Shipton & Cowie 2001). Mair et al. (2000) studied the sequential growth of deformation bands in the laboratory and found evidence for an increased number of discrete deformation bands with increased strain. Furthermore, Shipton & Cowie (2001) noticed that slip surfaces in porous sandstones tend to nucleate from an area with an increasing amount of deformation bands, also known as the process zone. This suggests that the accumulation of strain will form more deformation bands, which ultimately can form a through-going slip surface. The deformation band process zone can be up to 100 m ahead of the fault tip, but

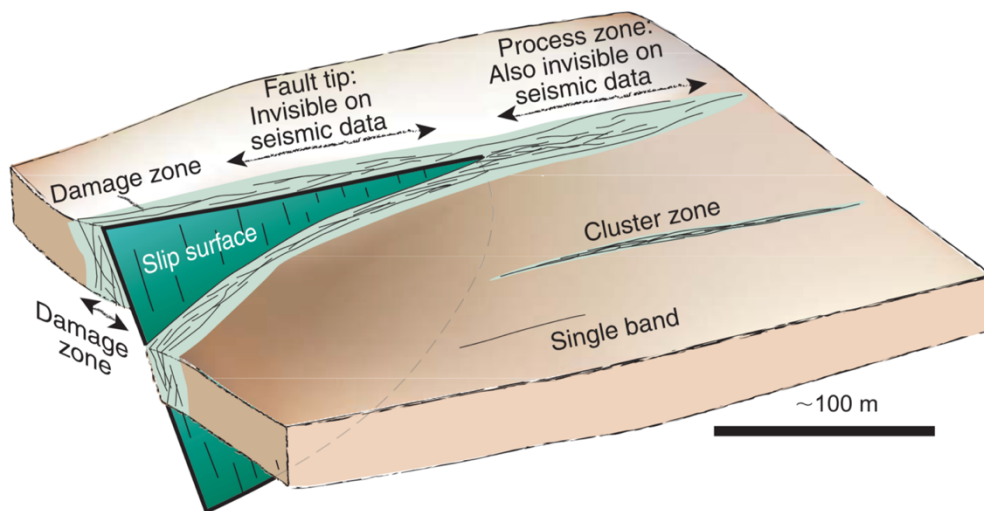


Figure 3.2: Conceptual illustration of a fault slip surface with associated damage zone, cluster zone and single bands in porous sandstone. From Fossen et al. (2007).

depends heavily on lithology (Fossen et al., 2007); A well-sorted porous sandstone will favour the development of long process zones (Fig. 3.2), such as the Entrada and Navajo sandstones found in Southern Utah (Shipton & Cowie, 2001; Rotevatn et al., 2007). The damage zone widens as new deformation bands form within and outside the process zone (Schueller et al., 2013). This is explained by strain hardening and strain softening mechanisms where strain hardening cause deformation to be extended into undeformed host rock (Shipton & Cowie,

2003). Once a slip-surface nucleates, the mechanism shifts to strain softening (Mair et al., 2000; Shipton & Cowie 2001). Schueller et al., (2013) observed that the density of bands is independent of fault displacement and revealed a non-linear relationship between damage zone width and fault throw, with a corresponding power-law exponent close to 0.5. Furthermore, the results showed a statistically wider hangingwall damage zone compared to footwall damage zone (Schueller et al., 2013). The degree of clustering is also considered to be independent of fault displacement and should therefore be more or less similar along a fault trace (Du Bernard et al., 2002; Schueller et al., 2013).

3.2.1 Mechanisms and host rock properties

Deformation band formation is controlled both by external conditions and internal properties within the host rock (Fossen et al., 2018). Internal host rock properties involve the degree of lithification, mineralogy, grain size, sorting, and grain shape. External factors include confining pressure (burial depth), deviatoric stress (tectonic regime), and pore – fluid pressure (Fossen et al., 2007) (Fig. 3.3A). These factors may vary; e.g. The confining pressure increases with burial depth, while the deviatoric stress depends on the tectonic regime (Fossen et al., 2018). Antonellini et al. (1994) documented a temporal evolution of deformation bands at the Colorado Plateau, showing disaggregation bands at shallow burial depth developing into cataclastic bands at greater depth (Fig. 3.3B).

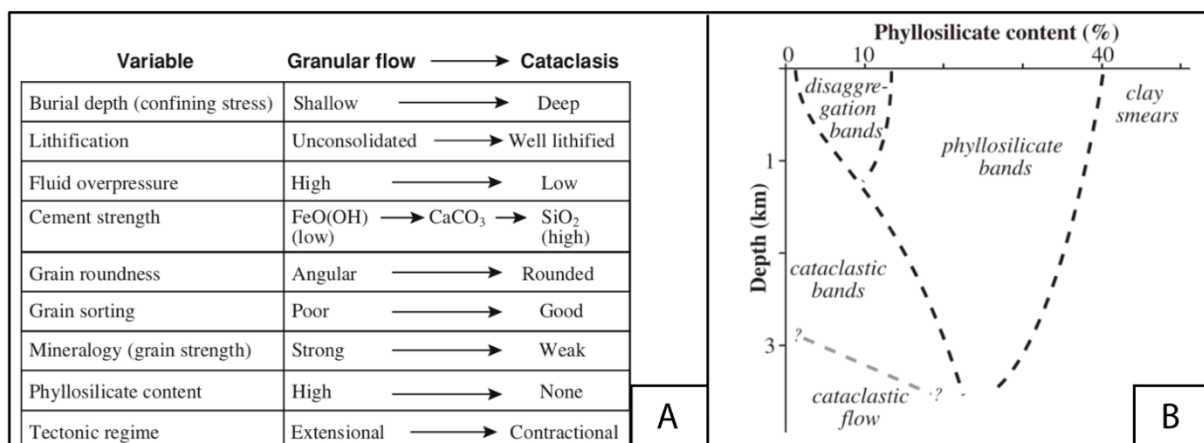


Figure 3.3: A) Table listing factors that influence the degree of cataclasis in deformation bands. From Fossen et al. (2018). B) Diagram showing how the relation between burial depth and phyllosilicate content can influence deformation band mechanisms. From Fossen et al. (2007)

In an extensional regime, the overall horizontal stress is reduced, thereby prompting a non-cataclastic grain-flow at more shallow burial depths, whereas a compressional regime increases the overall mean stress and may cause cataclasis at shallower burial depths (Solvia et al., 2013).

Simple shear kinematics, non-cataclastic deformation, pure compaction, and dilation tend to materialize at shallow burial depths in unconsolidated and poorly consolidated sandstones (Fossen et al., 2018). In granular rocks, the stress is concentrated at grain contacts (Antonellini et al., 1994). Consequently, low confining stresses will favour granular flow (disaggregation bands), while high confining pressures will promote cataclasis (cataclastic bands). A well-sorted host rock is likely to enhance cataclasis, as fewer grain-contact points increase the overall stress on each contact point (Antonellini & Pollard, 1995; Cheung et al., 2012). High fluid pressure, however, can counteract cataclasis and enhance the formation of disaggregation bands and dilational bands at greater depths (Fossen et al., 2018).

3.2.2 Deformation Band Classification

Deformation bands can be classified based on kinematics or by the dominant mechanism active during the formation (Aydin et al., 2006; Fossen et al., 2007). Based on kinematics, deformation bands can be divided into three end-members (Fig. 3.4): (1) Dilation bands (DSB); (2) compactional shear bands (CSB); (3) pure compaction bands (PCB) or a combination (dilational shear bands, compactional shear bands, shear enhanced compaction bands and shear enhanced dilation bands) (Du Bernard et al., 2002; Aydin et al., 2006; Fossen et al., 2007). CSB is a common type of deformation band, which forms by grain reorganization (Fossen et al., 2007). Dilational shear bands are uncommon, but they have been observed in laboratory experiments and in the field (Antonellini et al., 1994; Du Bernard et al., 2002). Dilation can occur at an early stage of compactional shear band development (Bésuelle, 2001).

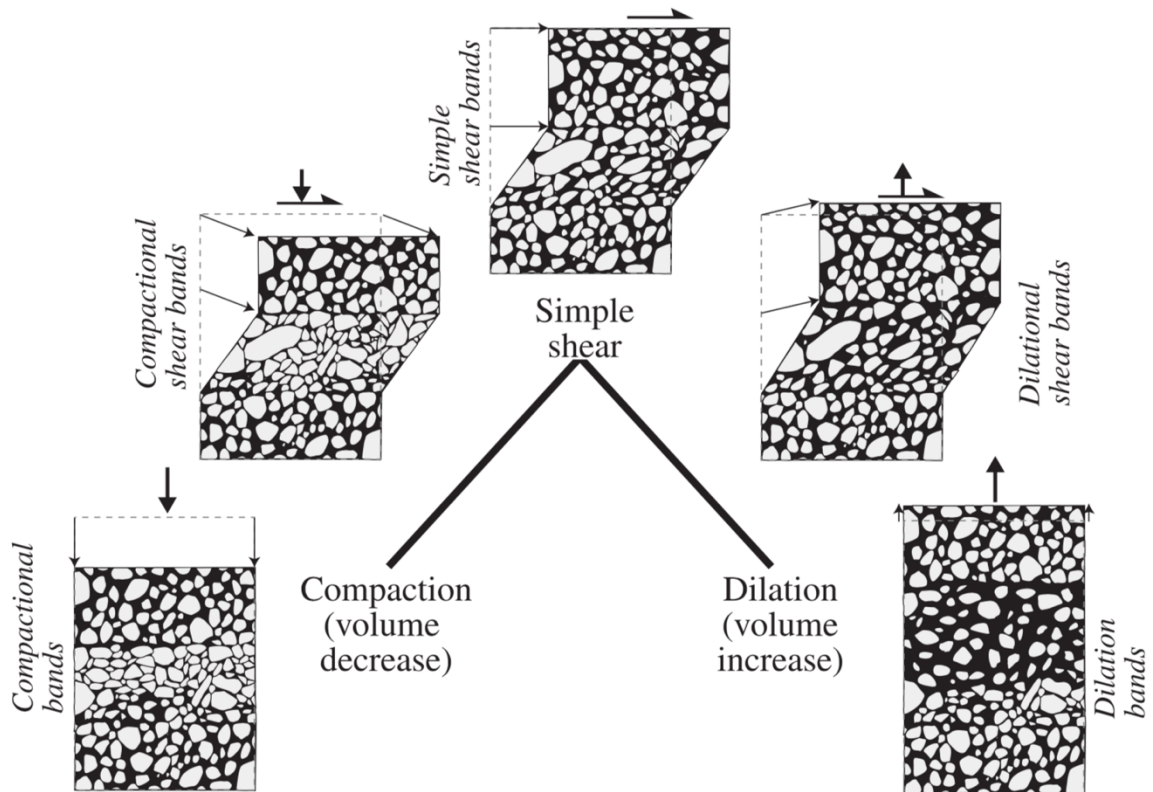


Figure 3.4: Kinematic classification diagram for deformation bands. From Fossen et al., (2007).

External and internal conditions within the host rock favours different types of deformation mechanisms, which will result in different petrophysical properties (Fossen et al., 2018). It is therefore useful to categorize deformation bands based on the dominating deformation mechanism: (1) Disaggregation bands (granular flow); (2) Phyllosilicate bands (Phyllosilicate smearing); (3) Cataclastic bands (grain fracturing); (4) Dissolution and cementation bands (Fossen et al., 2007).

Disaggregation Bands

Disaggregation bands develop as a result of granular flow: a process that involves grain rolling, grain boundary sliding, and breaking of grain bonding cement (Fig. 3.5A) (Fossen et al., 2007). Disaggregation processes are commonly active and dominating at shallow burial depths (<1km) in sands and poorly consolidated sandstones (Mandl et al., 1977; Knipe et al., 1997; Du Bernard et al, 2002). With greater stress, the shearing can be accompanied by grain crushing (Mandl et al., 1977), causing cataclasis. However, high fluid pressure can counteract cataclasis and favour disaggregation mechanisms at greater depths (Fossen et al., 2018).

Disaggregation bands do not involve any fracturing of grains and often appear as invisible bands, as only the orientation and position of the grain is altered (Fossen et al., 2007). These types of bands do not modify the permeability and porosity of the host rock to a large extent and are therefore not considered important barriers to fluid flow (Knipe et al., 1997).

Phyllosilicate bands

Phyllosilicate bands, also referred to as framework phyllosilicate bands, develop in sandstones with a significant amount of platy minerals (>10-15%) (Knipe et al., 1997; Fossen et al., 2007). Phyllosilicate bands form under the same conditions as disaggregation bands (Fig. 2.6B). However, the platy minerals prompt frictional boundary sliding and can therefore be considered a sub-group of disaggregation bands (Fig. 3.5B) (Fossen et al., 2003; Fossen et al., 2007). The platy minerals in the phyllosilicate bands counteracts strain hardening and causes a smearing effect. Consequently, phyllosilicate bands may develop quite big offsets compared to other types of deformation bands (Fossen et al., 2007)

The permeability reduction caused by phyllosilicate bands is dependent on the abundance, distribution, type, and grain size of the phyllosilicates, as well as the amount of displacement (Knipe, 1992). The mixing and alignment of the platy minerals normally varies within a single band. For this reason, the effective permeability of a single phyllosilicate band also tends to vary (Knipe et al., 1997; Fossen et al., 2007). Fisher & Knipe (2001) observed a reduction in permeability between two and five orders of magnitude in siliciclastic petroleum reservoirs in the North Sea.

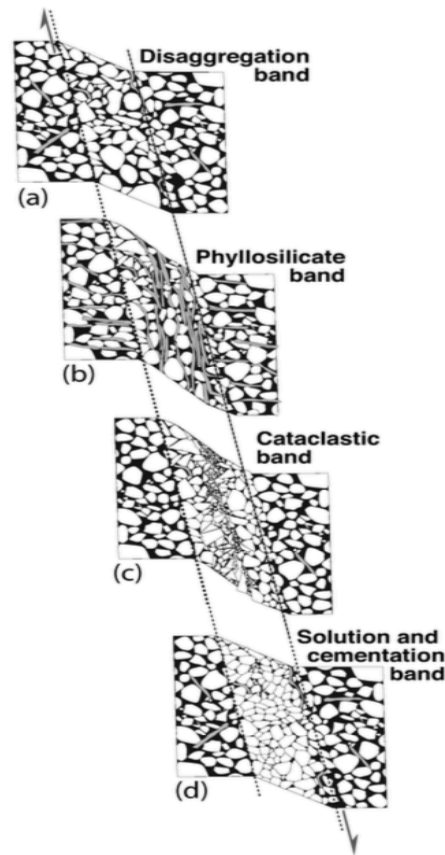


Figure 3.5: Illustrative presentation of the different types of deformation bands. The classification of is based on the dominating deformation mechanism. From Fossen et al. (2007).

Cataclastic Deformation Bands

Cataclastic bands form as a result of grain fracturing (cataclasis) due to concentrated stress at grain contact points (Fig. 3.5C) (Aydin, 1978). Cataclastic deformation bands can be divided into a core and a transition zone (Fossen et al., 2007). The core is commonly characterized by grain size reduction, lack of pore space, angular grains, and a high matrix content (Fossen et al., 2007). The transition zone, also referred to as deformation band outer zone by Aydin (1978), is characterized by compaction (granular flow) and a smaller amount of grain fracturing.

The porosity of a single band is commonly reduced by up to one order of magnitude (Antonellini & Aydin, 1994), while the permeability on average is reduced about three orders of magnitude (Antonellini & Aydin, 1994; Jourde et al., 2002; Fossen et al., 2007). The permeability is reduced more in shear bands than in compaction bands (Ballas et al., 2015).

Cataclastic deformation bands tend to develop smaller offsets compared to disaggregation bands, which might be explained by the extensive interlocking of grains, prompting strain

hardening (Fossen et al., 2007). Ballas et al. (2015) proved a correlation between grain crushing intensity increase and permeability decrease. Normal faults typically lead to the formation of cataclastic shear bands, with intense cataclasis and high permeability reductions, while cataclastic bands in a thrust fault regime show a more moderate decrease in permeability. Generally, this shows that permeability is greater reduced in shear bands than compaction bands (Ballas et al., 2015; Soliva et al., 2016)

Cataclastic deformation bands commonly develop in, but are not restricted to sandstones at depths 1,5-2,5 km (Fossen et al., 2007). Cataclastic deformation bands have additionally been observed in unconsolidated sands in accretionary prism sediments (Ujiie et al., 2004), in volcanoclastics (Wilson et al., 2003) and in limestones (Rotevatn et al., 2016). Cataclastic deformation bands and their effect on fluid flow is well documented in geological literature and will be further discussed in the following subchapter (e.g. Sternlof, 2006; Fossen & Bale, 2007; Rotevatn et al., 2013)

Studies have shown that cataclasis localization is highly dependent on the tectonic regime (Fossen et al., 2018). Extensional tectonics tend to prompt the formation of clusters of deformation bands, whereas contractional tectonics tend to result in larger distribution of bands, commonly forming arrays of conjugate sets (Ballas et al., 2015; Soliva et al., 2016).

Dissolution and Cementation Bands

The formation of dissolution and cementation bands is related to the mineral coating on the grains and chemical compaction or pressure solution (Fig. 3.5D). Dissolution and cementation mechanisms can be active both during and after deformation (Fossen et al., 2007; Ballas et al., 2015). Clay minerals at grain boundaries typically promote dissolution (Fossen et al., 2007). Dissolution bands in siliciclastic rocks commonly form at shallower depths and are typically characterized by tightly packed quartz grains surrounded by a coarser matrix with a serrated and irregular grain boundary and little evidence of cataclasis (Fossen et al., 2007). Cementation processes are related to cataclasis and grain boundary sliding, revealing fresh reactive grain surfaces, which then further enhance cementation (Fossen et al., 2007).

3.2.3 Deformation bands and fluid flow

Deformation bands and their effect on fluid flow in reservoirs is heavily debated in geological literature (e.g. Rotevatn et al., 2007; Fossen & Bale, 2007; Rotevatn et al., 2013; Ballas et al., 2015). It is well documented that the majority of deformation bands show a reduction in permeability and porosity (Antonellini & Aydin, 1994; Jourde et al., 2002; Fossen & Bale, 2007). However, the actual impact on fluid flow is still debated; Fossen & Bale (2007) modelled the effect of deformation bands with respect to fluid flow. The results showed that deformation bands may influence flow pattern within a reservoir, implying that the overall effect is closely linked to the arrangement and the orientation of deformation bands (Fossen & Bale, 2007).

The thickness, porosity, permeability, and the continuity of single deformation bands and clusters vary significantly (Fossen et al., 2007). Rotevatn et al. (2013) demonstrated with simulations that the thickness variations along bands overall had a negligible effect on fluid flow, further demonstrating that the configuration and connectivity of deformation bands are more important controls for the effective permeability, along with the permeability contrast between bands and host rock, and the mean band thickness. A damage zone comprised of deformation bands with low permeability contrasts will have limited or no effect on fluid flow, while high permeability contrast can (three orders of magnitude or more) affect the flow tortuosity and sweep efficiency, or act as a barrier to fluid flow (Rotevatn et al., 2009).

3.3 Topology

Topology has been used to describe complex networks in engineering, communication, and social sciences (e.g. Latora & Marchiori, 2002; Boccaletti et al., 2006). In the last two decades topology analysis has become a useful tool for characterization and visualization of fracture networks, as it describes the geometric relationship and connectivity between fractures within a network (e.g. Manzocchi, 2002; Sanderson & Nixon, 2015). Deformation bands can occur as interconnected networks (Aydin & Johnson, 1978). A thorough topology analysis on deformation bands has not yet been conducted. Therefore, the concept of topology analysis is here explained for fracture/fault networks. Nevertheless, the concept is the same.

In two dimensions, a fracture network can be characterized as an arrangement of branches and nodes (Sanderson & Nixon, 2015). A branch is a continuous fracture that is bounded by a node

on each end, while nodes represent the intersection points along a fracture. Manzocchi (2002) defines three different types of nodes: I-, Y-, X-nodes (Fig. 2.6); An I – node (isolated tips) represents the point where a fracture terminates; a Y-node is the point where a fracture abuts, splay or cross-cut; and an X-node represents a fracture that cuts straight through another fracture with no offset. Nodes can further be used to distinguish three different types of branches (Fig. 2.6), hence: I-I branch (isolated), I-C branch (partly connected), and C-C branches (doubly connected) (Sanderson & Nixon, 2015).

Further enhancement in software has made it easy to extract statistics of fracture networks. For example, triangular plots can be made from the proportions of branches and nodes. The average number of nodes per branch provides a measure for the connectivity (connection per branch) of the network. In addition, the frequency and intensity of fractures can be extracted from nodes (Sanderson & Nixon, 2015).

Two fracture networks can have the same fracture intensity, orientation and length but show different topological characteristics (Sanderson & Nixon, 2015), which can result in different fluid flow properties. NetworkGT, a toolkit developed by Nyberg et al. (2018), can derive statistics from fracture networks, and can generate a range of different data plots; a spatial distribution of clusters and blocks within a network. This clustering and block analysis can, together with an analysis of nodes and branches, provide valuable information about potential fluid flow behaviour within a fracture network (Nyberg et al., 2018), as clusters can be pathways and/or barriers to fluid flow (Adler & Thovert, 1999)

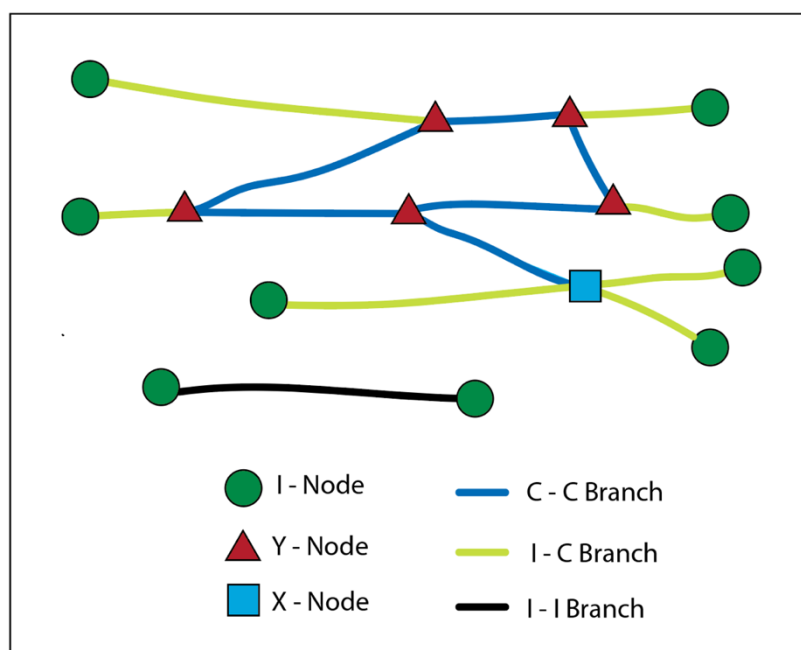


Figure 3.6: Conceptual illustration a network characterized by branches and nodes. Terminology from Sanderson and Nixon (2015).

Topology has been used to describe fracture and fault networks (Huseby et al., 1997; Manzocchi, 2002; Sanderson & Nixon, 2015; Morley & Nixon, 2016). Fault networks will normally show a higher proportion of Y-nodes than X-nodes due to preservation problems; cross-cutting faults are often offset by the recent active fault, resulting in two Y-nodes, instead of one X-node. For this reason, X-nodes are mainly observed in joint and fracture arrays (Morley & Nixon, 2016). Manzocchi (2002) presents a triangular plot, showing deformation bands with a high proportion of Y-nodes. Topology can though be quantified and visualized in various ways, which are explained in the methodology chapter (Chapter 4).

4 Data and Methodology

This chapter elaborates on the methods used in the data collection and -analysis in this thesis. Outcrop data was collected during two field campaigns in Utah in May 2019 and October 2019. The study-areas were selected based on the relevance and quality of the exposures, and their accessibility. Table 4.1 presents a summary of the applied methodologies, aims and datasets, which are explained in detail subsequently.

Table 4.1: Summary of methods used in this study, with their aims and resolution.

	Method	Aim	Dataset	Resolution
Fault analysis	Structural mapping: quantification of fault orientation (strike/dip) and displacement	Constrain damage zone extend, fault displacement	Outcrop data Virtual outcrop models	1-300m
Deformation band analysis	Circle sampling	Deformation band orientation, - length and topological attributes (connectivity, nodes etc.)	54 circle samples (Fig. 5.3 and 5.7)	cm-mm
	Line sampling	Deformation band frequency distribution	53 Line samples (Fig. 5.11 and 5.18)	cm-mm
	Network grid sampling	Sample spatial variation In geometry and topology throughout deformation band network	3 orthomosaics (Fig. 5.14, 5.15, and 5.20)	cm-mm
Virtual outcrop models	Fault and deformation band analyses (digital)	Determine type of fault interaction, -displacement and the overall orientation of deformation band clusters	2 outcrop models (Fig. 5.11b,c)	1-100m

4.1 Data acquisition: Fieldwork

Three weeks of fieldwork in Utah was carried out during two field campaigns in 2019, May and October. Firstly, a regional understanding of the structural setting and geology of the study was achieved through structural mapping, mainly using Fieldmove Clino, which is a practical instrument for measuring structural inclinations (strike/dip) and constrain the extend and displacement of faults and deformation bands. The application contains a digital compass–clinometer that stores the GPS positions of measurements and allows for attachment of photos and observatory notes to these. To avoid measurements error, strike/dip measurements were carried out with a physical compass with clinometer. For the purpose of building virtual outcrop models (3D models), aerial drone photos were acquired with a DJI Mavic Pro drone; with exception of the Klondike Bluffs region, where strict UAV restrictions prohibit drone flying.

Secondly, deformation band networks, the key focus of this thesis, were studied on cm scale. The most fundamental data type for the study of deformation band networks in this thesis are high-resolution outcrop photos. Mapping of total deformation band networks can though prove difficult as it requires a continuously good exposure. The sampling strategy thus depend largely on scale, spatial extent and exposure quality. Photos of deformation band networks were captured both by drone and handheld camera. Essentially, the resolution of the drone photos was not high enough to capture detailed deformation band networks and has therefore not been utilized for this purpose in the study. Aerial drone photos are though used for building outcrop 3D models. The handheld camera photos were shot approximately 1-1.5 m above ground. To ensure minor orientation bias, the photos were shot perpendicular to the exposed rock surface. Continuous photo transects were captured in areas with laterally extensive exposure. These were stitched together and geometrically corrected in Agisoft Metashape, which was further used to build virtual outcrop 3D models. Details on data processing are elaborated in section 4.2.

In the field, photos of deformation bands were acquired in two different ways; continual photo transects and circle sampling. Continual photo transects were acquired in areas with extensive exposure. Circle sampling has been used to sample deformation band networks in areas with limited exposure, thus allowing for a larger areal coverage when recording general geometric- and topologic trends. The circle samples (Fig. 4.2a,b) are one m in diameter and placed in intervals of one to twenty m depending on the exposure quality and size of the field locality.

Sampling at constant intervals proved challenging, due to occasional poor exposure or no display of deformation bands. To eliminate this issue, a more selective approach was implemented in the systematic data acquisition: in sample areas with poor exposure, circle samples were placed with up to three m deviation from the planned path to ensure low bias.

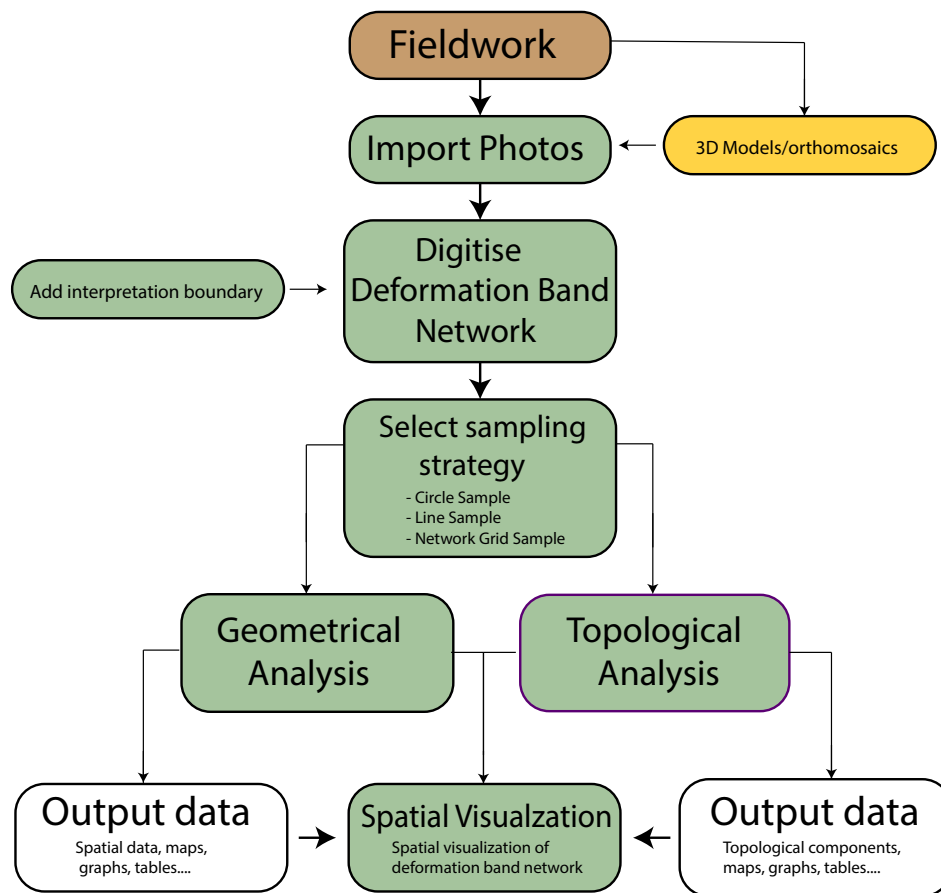


Figure 4.1: Flowchart displaying the workflow from data acquisition to digitalisation, analysis and spatial visualization of deformation band networks. Photos and/or orthomosaics acquired in the field are imported to QGIS and georeferenced. Deformation bands are then digitised manually, and a sampling method is chosen. A geometrical- and topological analysis is then conducted, which provides output data and a spatial visualization of the deformation band network. The brown colour represents data acquired in the field, while yellow indicates data processed in Agisoft Metashape. The green colour is data processed in QGIS. Modified from Nyberg et al. (2018).

4.2 Data processing

Fig. 4.1 presents a detailed workflow. The first step was to process the photos acquired with manual photography and Unmanned Aerial Vehicles (UAVs), which represents a simple, efficient and low-cost method for acquiring virtual outcrop data, compared to the older Light Detection and Ranging (LiDAR) scan. The photos were processed in Agisoft Metashape, where digital photos can be shaped into 3D models and/or 2D surfaces for use in GIS applications. The software utilizes a photogrammetry technique called Structure from Motion (SfM), in which continuous movement of the drone provides depth information. The SfM algorithm recognizes common features in overlapping pictures and assigns a 3D coordinate to every single matched point. Next, a multi-view stereo algorithm is used to generate a dense cloud that fill the empty space surrounding the matched points (e.g. Hirschmuller, 2007; Cawood et al. 2017). Agisoft Metashape was primarily also used to make high resolution orthomosaics: detailed maps generated from several stitched and geometrically corrected photos processed with a given projection to achieve a uniform scale and provide high-resolution photos of deformation band networks (Fig. 4.4A).

4.2.1 Analysis of network topology using QGIS and NetworkGT

Photos and orthomosaics of outcrops exhibiting deformation band networks were mapped and digitised with QGIS, which is an open-source Geographic Information System (GIS) for viewing, editing and analysing geospatial data. Sampling, analysis, and spatial mapping of topological attributes was performed with a NetworkGT (toolbox) plugin in QGIS, developed by Nyberg et al. (2018).

For the purpose of characterizing and describing deformation band networks, a topological and geometrical approach was used. A geometrical approach provides information on deformation band orientations (rose diagrams), lengths and intensity variations (line frequency plots) (Nyberg et al., 2018). The topological analysis introduced for fractures in chapter 3 can also be applied for deformation bands. Deformation bands can be viewed as networks of branches and nodes that are categorized based on their connection points and number of bifurcations. The

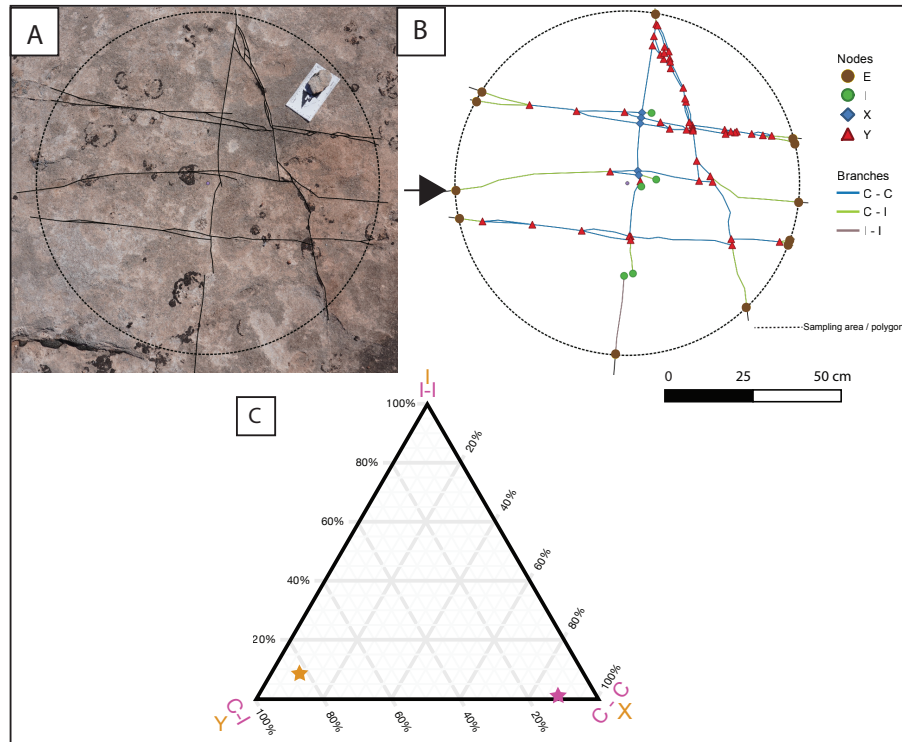


Figure 4.2: Figure demonstrating an example of the digitalization process of an acquired photo in the field and the extraction of topological and geometrical data from this: A) Circle sample with mapped deformation bands (black lines). B) Identification of topological data within the circle sample with the NetworkGT toolkit. C) Distribution of Nodes and Branches plotted in a ternary diagram.

features distinguished in this study are I-nodes, Y-nodes, X-nodes, and branches. I-node represents the tip of a deformation band, while a Y-node is the point where a deformation band splay or abut against another deformation band. When a deformation band cross-cut another deformation band and show no offset it is called an X-node. A branch is limited by a node in each end and three types are recognized: Isolated branches (I-I), partly connected branches (I-C), and doubly connected branches (C-C) (Ortega & Marrett, 2000; Sanderson & Nixon, 2015).

Three digital sampling methods were applied in this study, all provided in the NetworkGT toolkit: (1) circle sampling, (2) line sampling, and (3) network grid sampling. Line sampling extracts data in one-dimension and is used to extract information on deformation band frequency by counting intersections along a line. Sampling is preferably perpendicular to the trend of the deformation bands to prevent under sampling (Nyberg et al., 2018). This sampling method provide valuable information on deformation band frequency but can be subject to orientation and length bias. The use of circle samples eliminates this orientation bias in the plane and has been utilized in areas with limited exposure (Mauldon et al., 2001). The topological and geometrical analysis is applied to the sampling area, which is defined by a

polygon (interpretation boundary) (Fig. 4.2A). When a deformation band (branch) intersects with the polygon the intersection point is marked as an edge-node (E-node), and branches intersecting the polygon are counted as half branches (4.2B). The proportions of branches and nodes can be plotted in ternary plots for characterizing topology (Fig. 4.2C). The third sampling method, Network Grid Sampling, maps the spatial variation within a deformation band network. This sampling method is only applicable for areas where orthomosaics were acquired. NetworkGT generates a square grid with a given size within a given interpretation boundary. Subsamples (circle samples) are generated by assigning a centroid point and radius to every grid cell (Fig. 4.3). Topological and geometric variations in a deformation band network can then be visualized in a wide range of intensity maps (Fig 4.4D), such as 2D intensity and node distribution. 2D intensity refers to the sum of branches divided by the size of the sample area, which provides a measure of the deformation band intensity within the sample area (see Table 4.2). A wide range of data can be extracted from combining topological and geometrical data, such as information regarding the average branch lengths from each sample. Connections per branch provides a dimensionless measure of the connectivity in a network, which ranges from a minimum of 0 to a maximum of 2 connections per branch (Sanderson & Nixon, 2015). Furthermore, the block analysis tool in NetworkGT allows for assessment of the average block size (areas that are fully enclosed by deformation bands) (Fig. 4.4C). A summary of all parameters with formulas and abbreviations are listed in table 4.2.

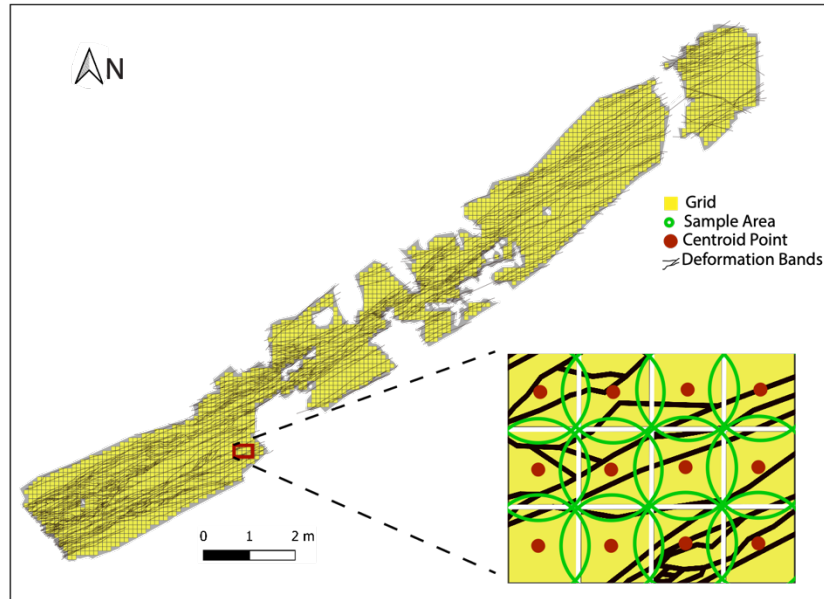


Figure 4.3: Figure demonstrating the network grid sampling method. Every block/cell is assigned a centroid point and a given radius. The network grid sample area is thus composed of several circle samples, which simplifies the visualization of changes in topology within a deformation band network. See figure 4.4D for an example.

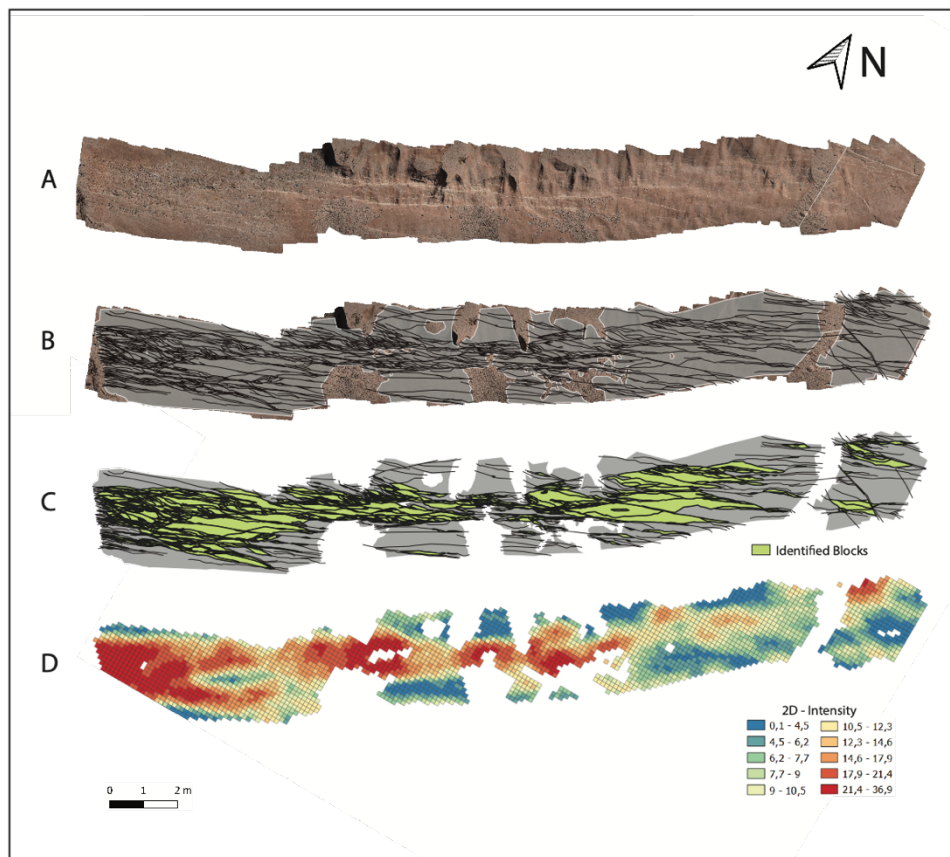


Figure 4.4: A-D Showcase the process from mapping deformation bands in QGIS, to visualization and data analysis. A) Orthomosaic, composed of 103 stitched and geometrically corrected photos. B) The black lines indicate deformation bands, while the grey bounding polygon is the interpretation boundary/sampling area. C) The green colour highlight blocks within the deformation band network. D) 2D intensity map showing the intensity variation within a deformation band network, composed of grid cells with circle samples, as shown in Fig. 4.3.

Table 4.2: This table presents a summary of abbreviations and formulas used to calculate various parameters in a digitised deformation band network, all provided in the NetworkGT toolkit. Modified from Nyberg et al. (2018).

Parameter	Description	Calculation
Area (A)	Sample area	A
Number of nodes (N_n)	Number of I, Y and X nodes	$N_I + N_Y + N_X$
Number of connections (N_c)	Number of X and Y nodes	$N_Y + N_X$
Connection/branch (C_B) (Connectivity)	Connections per branch (Connectivity), min = 0, max = 2	$\frac{3N_Y + 4N_X}{N_B}$
Total trace length $\sum L$	Sum of branch lengths	$\sum L$
Average branch length (B_c)	Average branch length	$\frac{\sum L}{N_B}$
2D intensity	Intensity of deformation bands within a sample area	$\frac{\sum L}{A}$
Block analysis		
Number of intersecting clusters (K_i)	Number of clusters that intersects the bounding polygon	K_i
Number of branches (block calculation) (B)	Number of branches, calculated from nodes and E nodes	$\frac{N_I + N_E + 3N_Y + 4N_X}{2}$
Number of nodes (block calculation) (block calculation) (N)	Number of I, Y, X and E nodes	$N_I + N_E + N_Y + N_X$
Number of whole blocks (W_b)	Whole blocks within the sample area	$B - N + K_{ij}$
Number of half blocks (H_b)	Potential blocks that are only partially within the sample area	$\frac{N_E - K_i + 1}{2}$
Number of theoretical blocks (T_b)	Total number of whole and half blocks	$W_b + H_b$
Theoretical block size	Average area of theoretical block	$\frac{T_b}{A}$

5 Results

Five deformation band networks have been studied in detail: three cluster zones in the wall damage zone of the Big Hole Fault, and two intersection damage zones in the Klondike Bluffs area (Table 5.1). A summary of the acquired data and applied method is presented in Table 4.1. The geometric and topological data and characteristics of the studied deformation band networks are presented and visualized below. For the full field datasets, including all geometrical and topological data, see Appendix II.

Table 5.1: Table listing the study areas, associated stratigraphic units, the sample numbers collected in said area, and the utilized sampling method.

Study areas	Stratigraphic (Fm./Mb)	Unit	Locality/Sample Names	Sampling method
Klondike East (Intersection damage zone)	Curtis Fm. /Moab Mb		1A – 41A	Circle sampling
Klondike West (Intersection damage zone)	Curtis Fm./Moab Mb		1B – 13B	Circle sampling
Big Hole Fault cluster I	Navajo Sandstone		BC1	Network grid saampling+ line sampling
Big Hole Fault cluster II	Navajo Sandstone		BC2	Network grid sampling + line sampling
Big Hole Fault cluster III	Navajo Sandstone		BC3	Network grid sampling + line sampling

5.1 Klondike Bluffs

Klondike Bluffs is situated on the SW limb of the Salt Valley anticline (Fig. 2.1). Structurally the area is dominated by cross-cutting normal faults (Fig. 5.1). The data from Klondike Bluffs is divided into Klondike West and East; each of these areas feature two intersecting faults (Fig. 5.1). It is the damage zones of these intersecting faults that are the features of interest here. The observations from each intersection are presented individually.

In both fault intersections, the aeolian Moab Member is offset by the faults. The Moab Member in Klondike Bluffs is a fine- to medium-grained sandstone ranging in colour from light grey to pale orange. The exposed cataclastic deformation band networks in the Moab Member are similar in characteristics to the thick deformation bands described by Fossen & Hesthammer

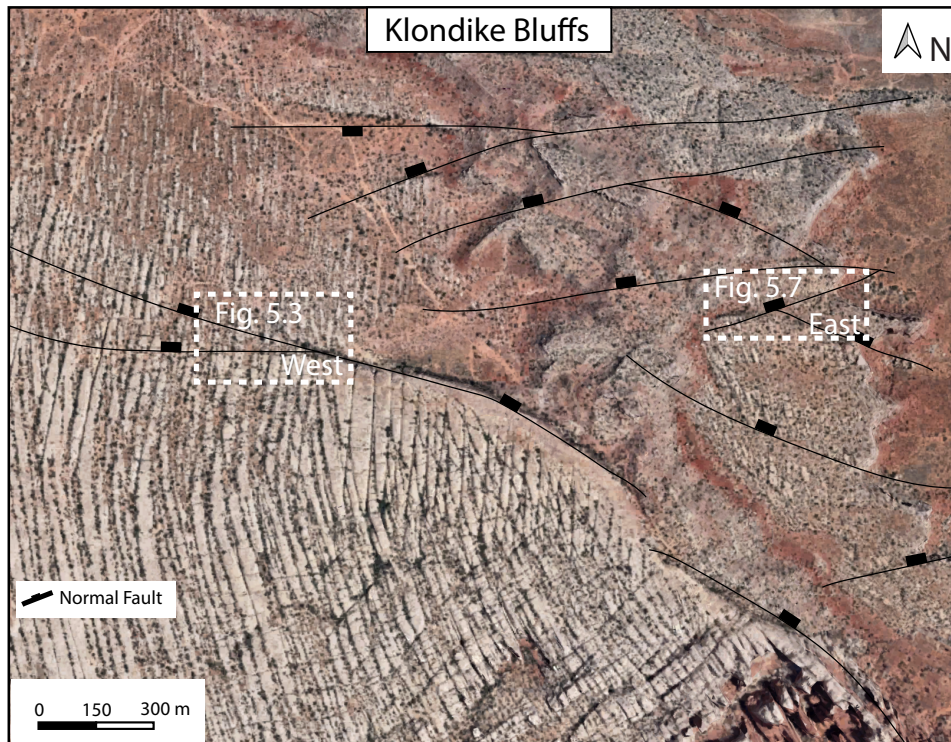


Figure 5.1: Aerial photo of Klondike Bluffs displaying the two studied fault intersections and other major faults within the area. The pale and light-colored outcrops expose the Moab Mb. of the Curtis Formation. The Entrada Sandstone is outcropped in red to brown colour. Aerial photo from Google Earth.

(1997) in San Rafael desert, and by Johansen et al. (2005) in the Arches area; The bands are commonly 1-1.5mm in thickness and tend to cluster in cm-wide zones, forming a raised relief in the outcrop (Fig. 5.2). The cataclastic deformation bands are generally well exposed, except where these are highly jointed or covered by vegetation.

5.1.1 Klondike West

Klondike West is characterised by a NW-striking normal fault, which dips c. 60° to the NE, intersected by a W-striking normal fault with a c. 75° N-ward dip (Fig 5.3). At the intersection point the displacement is approximately 10 m for the NW-striking fault and approximately 5 m for the abutting W-striking fault. The displacement along the NW-striking fault increases to a maximum displacement of c. 15 m 300 m SE of the intersection; NW of the intersection point, the NW-striking fault gradually decrease in displacement. The W-striking fault has a displacement of c. 5 m near the intersection point, gradually decreasing towards west.

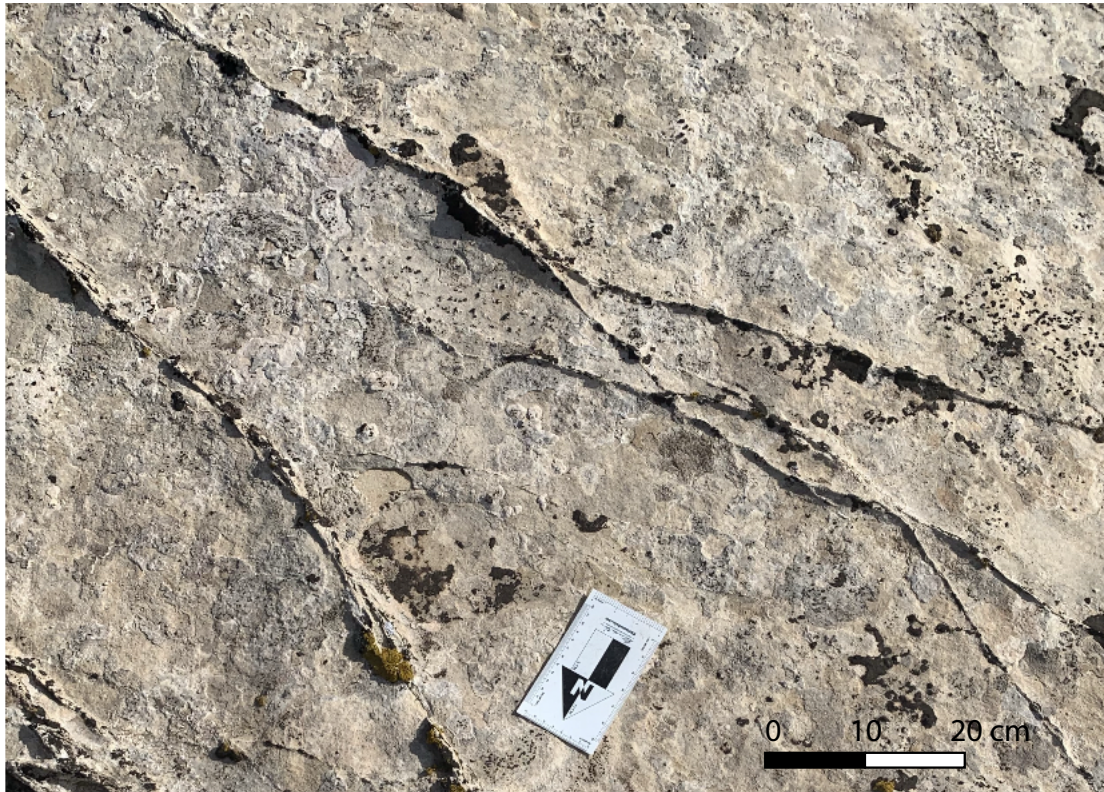


Figure 5.2: Example from Klondike Bluffs of deformation bands in the Moab Member showing an anastomosing zone of deformation bands and cm-wide cluster zones comprised of deformation bands. Notice how the bands are clustering in zones to form a raised relief.

The dataset acquired in Klondike west counts 13 circle samples with approximately 15 m spacing and 0.5 m sample radius, placed inside and outside the area bounded by the two intersecting faults (Fig 5.3). The circle samples have been analysed in accordance with the methods described in Chapter 4 to find geometric and topological characteristics.

Geometry

Most of the deformation bands are oriented WNW-ESE (Fig. 5.3), which is approximately parallel to the northwest-striking fault, with slight deviations observed in circle samples (CS) 4B and 8B, where they trend E-W. Furthermore, a larger spread in orientations relative to other circle samples is observed in CS 3B, 6B, 8B, 11B, 12B (Fig 5.2). No clear correlation is recognised between the spread and the deformation band intensity. The highest 2D intensity is found within the area bounded by the two intersecting faults, with a maximum intensity of 17.2 m^{-1} and 14.7 m^{-1} measured in CS 2B and CS 4B, respectively. The lowest 2D intensity is

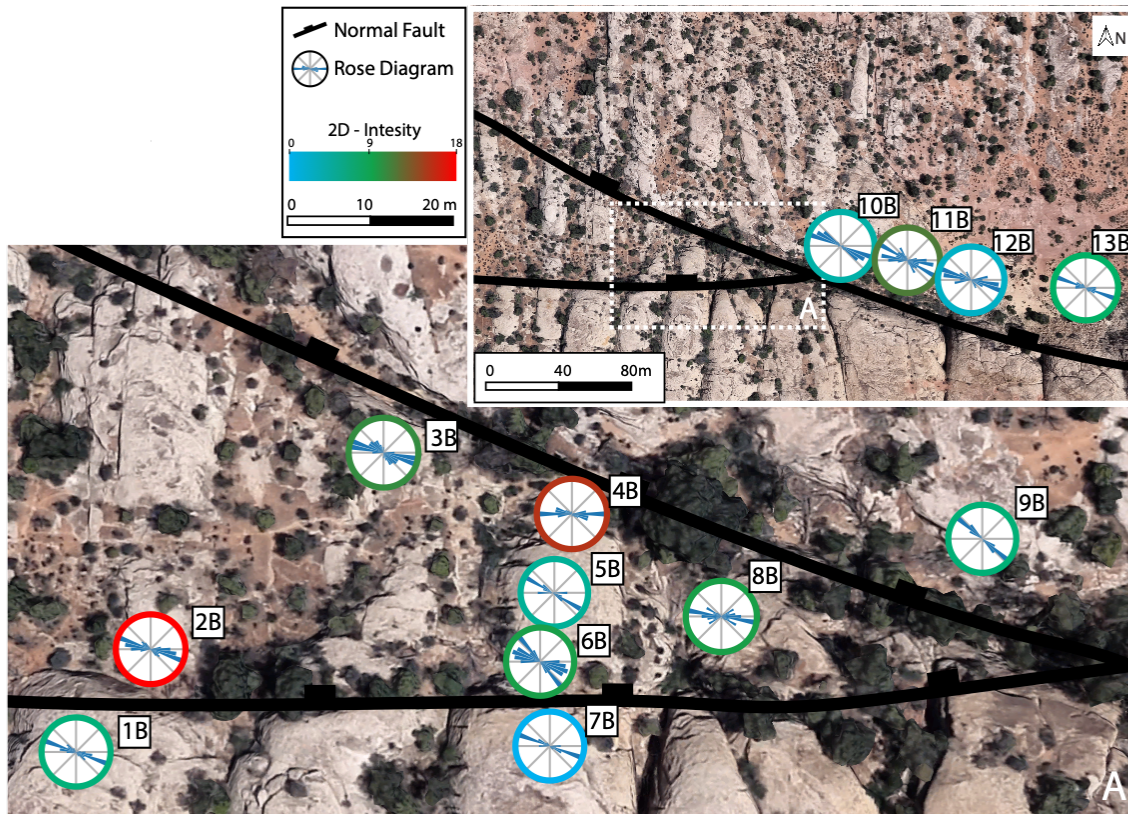


Figure 5.3: Overview of Klondike West, showing the studied intersection damage zone and the position of circle samples (not to scale). In the position of the circle samples are rose plots presenting the deformation band orientations coupled with 2D intensity (reflected by the circle colour). Aerial photo from Google Earth.

measured in the footwall to the W-striking fault in CS 7B (3.2 m^{-1}) and in the hangingwall to the NW-striking fault CS 9B (4.6 m^{-1}).

With an average branch length map (Fig. 5.6), the spatial variation in branch lengths throughout the damage zone is presented. Note that the average branch length derived from each circle sample is an average length of all branches within that sample. Overall, the branch lengths range from 7.7 cm (CS 7B) to 23 cm (CS 13B). There is a small tendency for inverse proportionality between 2D intensity and average branch length in samples 2B, 9B and 13B (Fig. 5.6). In these samples, it appears that high 2D intensity is associated with shorter branch lengths and vice versa. However, scatter plots (Fig. 5.5) of 2D intensity and branch length do not show any negative- or positive linear relationship.

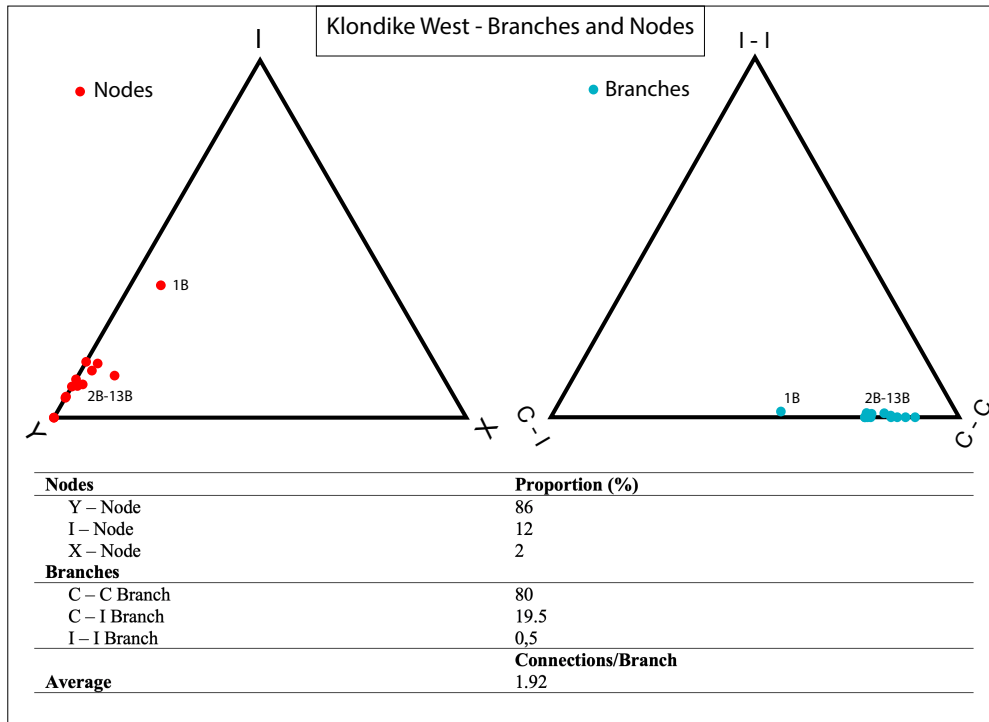


Figure 5.4: Ternary plots of node and branch distribution in Klondike East. The table contains information regarding the average proportion of nodes, branches and connections per branch

Topology

The node and branch plots (Fig. 5.4) clearly illustrate a damage zone dominated by Y-nodes and doubly connected branches (C – C). Average connections per branch for the whole damage zone is 1.92, which means an overall high connectivity for the deformation band network (Fig. 5.4) (the maximum number of connections per branch being 2; see chapter 4). No correlation is observed between 2D intensity and connectivity (Fig. 5.5). Maximum connectivity is observed in CS 9B and 10B, which are fully connected, while a minimum connectivity of 1.68 is observed in CS 1B. Consequently, CS 1B deviates from the other samples (Fig 5.4) with a higher proportion (37%) of I – nodes and partly connected branches (C – I branches) (43%).

Intensity maps further (Fig. 5.6) demonstrate topological variations throughout the damage zone. The 2D- and Y-node intensities appear to correlate; increased 2D intensity coincides with an increase in the number of Y-nodes. Scatterplots also display a positive relationship between the 2D-intensity and the number of Y–nodes (Fig. 5.5). The I–node intensity is rather low in the hangingwall to the NW striking fault, coinciding with low 2D intensities (Fig. 5.6). Thus, the number of I–nodes and the 2D intensity shows a moderate positive correlation (Fig. 5.6). The X-node proportion is at the other end of the spectrum with no occurrence (0%) in many

samples (Fig 5.6). The highest proportion (9%) of X-nodes is observed in CS 3B, which is found in the footwall to the northwest striking fault. X-nodes, however, do not appear to correlate strongly with the 2D intensity (Fig. 5.5).

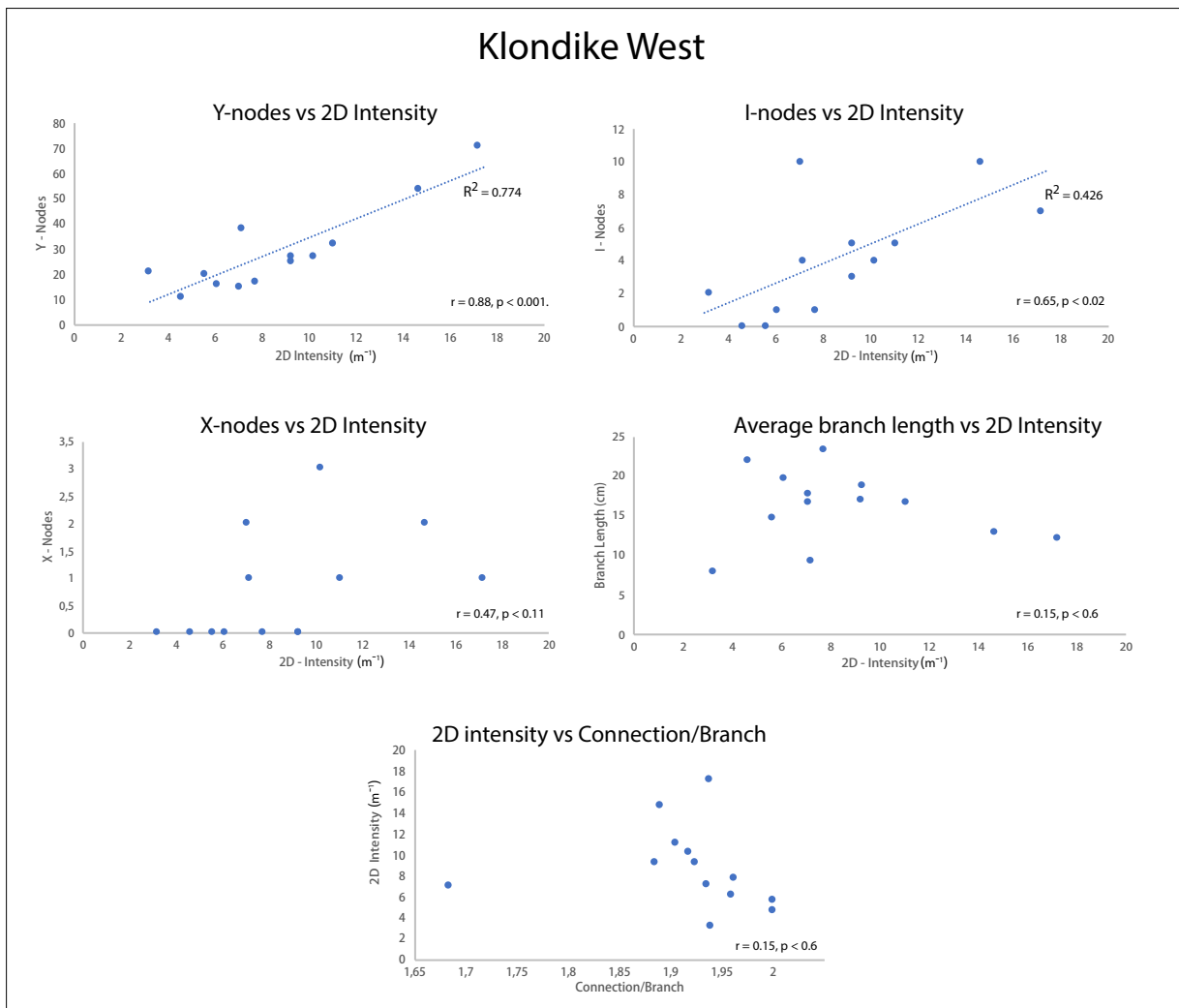


Figure 5.5: Scatterplots of 2D intensity plotted against number node types, connections/branch and branch length. A positive correlation is observed for 2D intensity and number of Y-nodes, and between 2D intensity and number of I-nodes. No clear correlation is identified for 2D intensity vs number X-nodes, branch length or connection/branch.

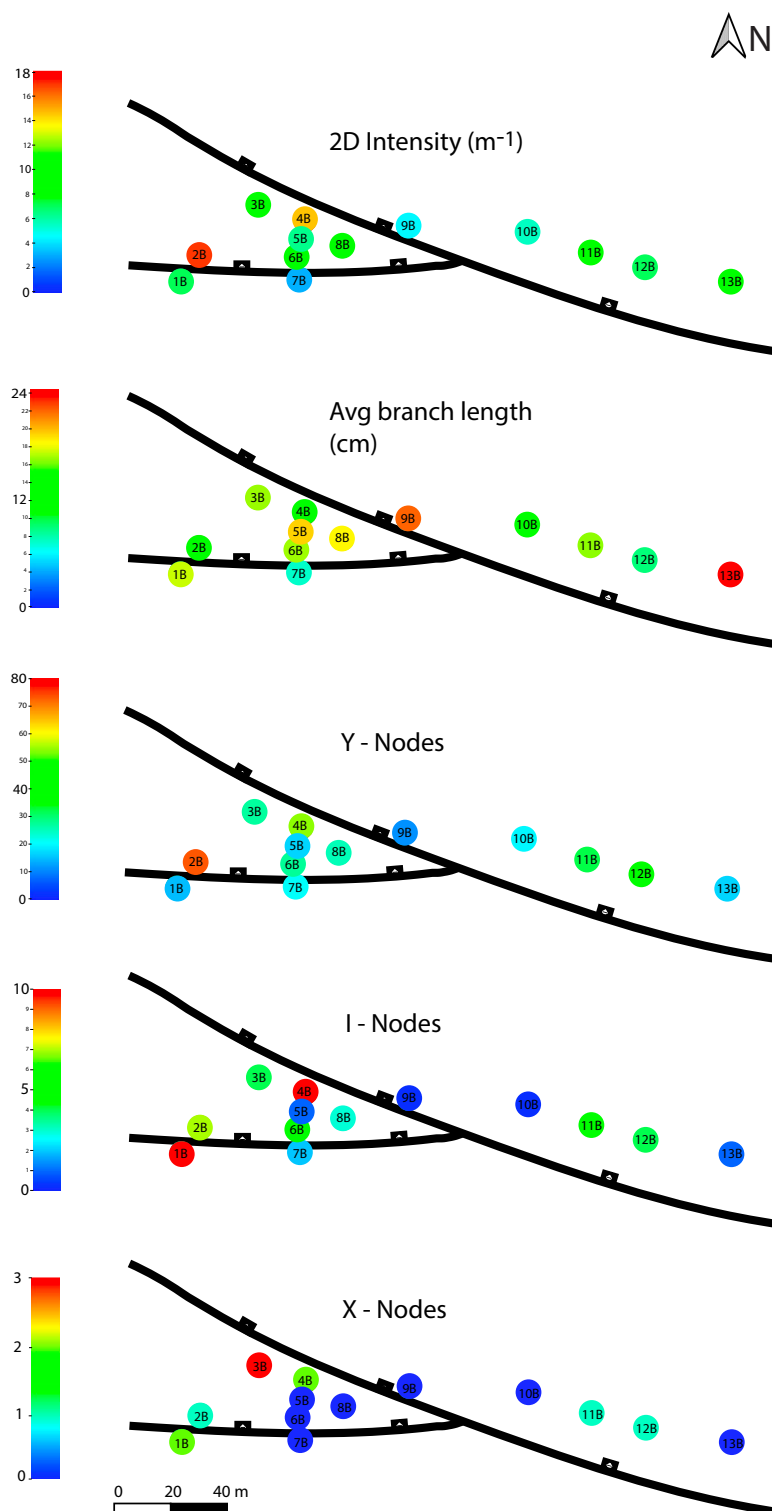


Figure 5.6: Intensity maps based on values from samples CS 1B to 13B displaying the overall distribution of 2D intensity, and Y-,I- and X-nodes. Average branch length maps display the average branch length within the circle samples. Blue colours reflect low intensity and red colour high intensity. Note that the colourbar scale is different for each map.

5.1.2 Klondike East

Klondike East is located 1 km east of Klondike west (Fig. 5.1 and 5.7). Structurally, the area is characterized by a WSW-striking normal fault that dips c. 70° to NW and is intersected by a WNW-striking normal fault with a c. 68° NNW-ward dip. The displacement along the WSW striking fault increases from c. 1 m displacement close to CS 1A to a maximum displacement of c. 12 m near the intersection point (Fig. 5.7). The WNW-striking fault has a displacement of c. 5 m near the intersection point, which gradually increases towards ESE to c. 10 m displacement near CS 10A. Overall, both faults show an increase in displacement in an easterly direction. The intersecting point is poorly exposed and severely fractured. The exact position is therefore determined by extrapolating the fault orientations.

The dataset for Klondike East comprises 41 circle samples (Fig. 5.7). Sample 1A to 10A, 11A to 13A and 14A to 16A were sampled with c. 20 m spacing, while the N-S transecting samples (17A to 24A, 25A to 30A, 31A to 37A and 38A to 41A) were picked with c. 3 m spacing.

Geometry

The majority of the deformation bands are trending between W-E and NW-SE, approximately parallel with the abutting WNW-striking fault. The spread of orientations within a single sample vary significantly. The largest orientation spread is found in CS 1A, in which some deformation band orientations are perpendicular to one another. It should be noted that this sample additionally displays a high proportion of X-Nodes – a relation that will be addressed later. A similar orientation spread is observed within CS 18A and 31A, both exhibiting an intermediate 2D intensity, while CS 1A indicate a fairly low 2D intensity (6 m^{-1}) (Fig. 5.10). No clear relationship between orientation spread and intensity is observed in these samples. The 2D intensity generally increase with increased proximity to the fault core (Fig. 5.10). Interestingly, some circle samples deviate from this trend and display a fairly low 2D intensity close to the fault core, such as 23A (4.4 m^{-1}). CS 22A is located c. 3 m north of CS 23A and display the highest 2D intensity (21.2 m^{-1}). Both samples are located in the footwall to the WSW-striking fault, adjacent to the intersection point. The lowest 2D intensity is found along the WSW-striking fault, in the transect covering the ENE part of the fault (Fig. 5.10) in samples CS 32A (5.9 m^{-1}), 33A (6.2 m^{-1}) and 34A (4 m^{-1}).

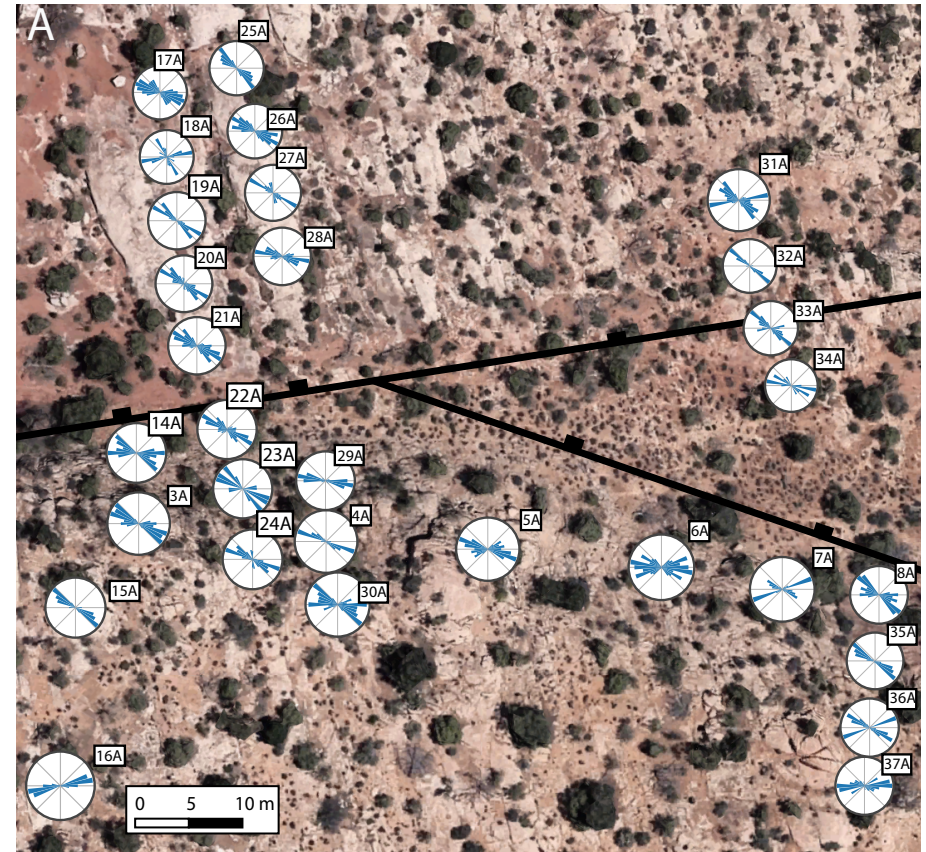
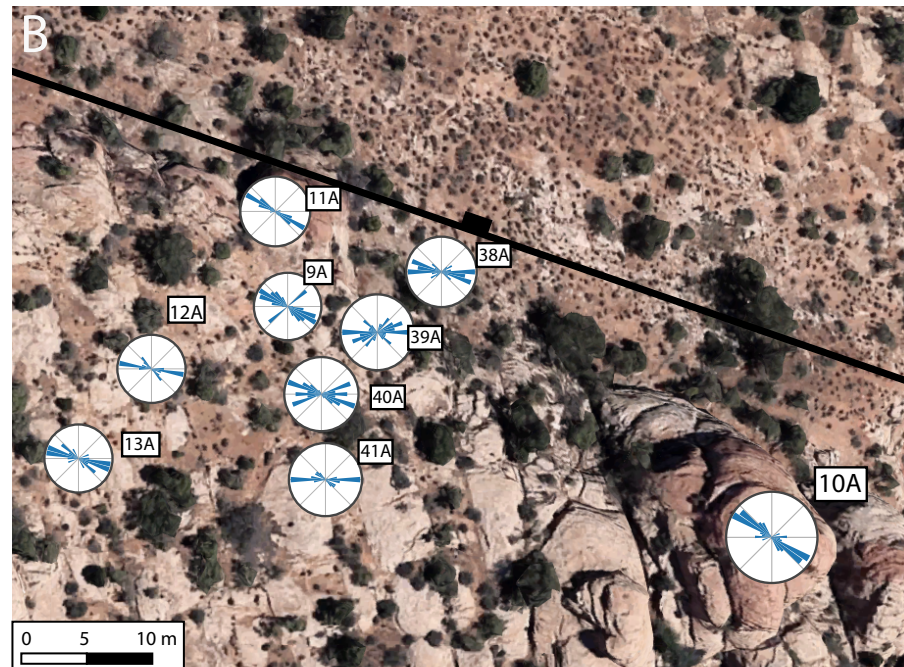
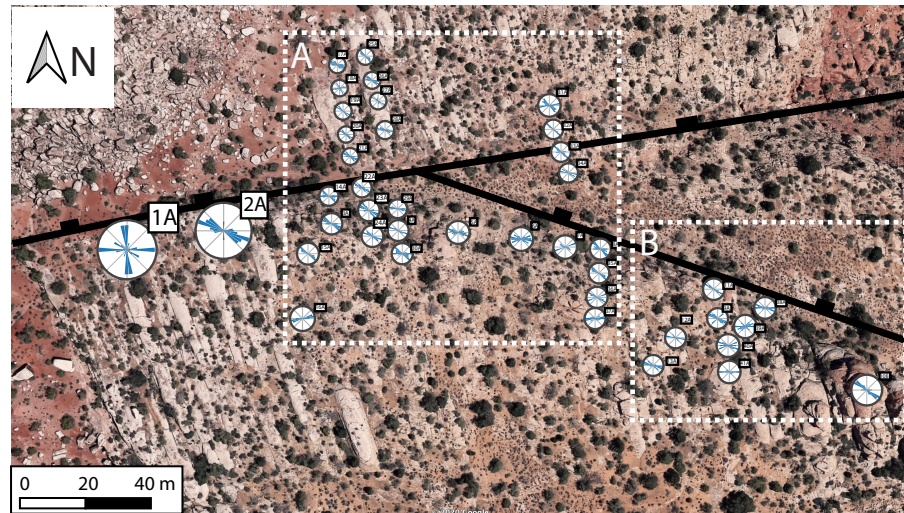
The average branch length ranges from 7.8 cm in CS 22A to 24 cm in CS 4A. The branch length map (Fig. 5.10) displays an area in the footwall to the WNW striking fault with high

values (CS 7A, 8A, and 34A to 37A) ranging from 18 to 23 cm. In contrast, most of these samples show a moderate 2D intensity, with CS 7A and 34A displaying fairly low intensities. The tendency of inverse proportionality between 2D intensity and average branch lengths is further recognized in CS 3A, 4A, 16A and 22A (FIG). Scatterplots of average branch length and 2D intensity do not show a relationship between the two (Fig. 5.9)

Topology

The branch and node data (Fig. 5.8) reveal a damage zone dominated by Y-nodes and doubly connected branches (C-C branches). This combination results in a high connectivity deformation band network with an average connection per branch of 1.96. 27% of the samples, distributed across the damage zone, display the maximum connectivity degree (2). No clear relationship is recognised between connectivity and 2D intensity (Fig. 5.9). The lowest connectivity is measured in CS 36A at 1.86, which nevertheless still reflects a high connectivity value. Accordingly, CS 36A displays the highest proportion of I-nodes (19%) and partly connected branches (C-I branches) (32%).

An overall low proportion of I- and X-nodes has been noted. However, the intensity maps display an overall correlation between increased 2D intensity and numbers of Y-, I- and X-nodes (Fig. 5.10). A strong positive correlation between the 2D intensity and the number of Y-nodes is recognized (Fig. 5.9). A moderate positive correlation is also observed for 2D intensity and number of I-nodes, while 2D intensity and number of X-nodes does not appear to correlate strongly with the 2D intensity (Fig. 5.9). The highest concentration of I-nodes is observed west of the intersection point, where the largest number of I-nodes is observed within CS 22A and CS 21A, respectively. The majority of X-nodes are located along or in close proximity to the faults. The highest number of X-nodes is counted in CS 22A, which coincides with the highest noted 2D intensity and shortest average branch length (Fig. 5.10). Three circle samples stand out in regard to orientation spread of deformation bands: 1A, 18A and 31A. These samples accommodate cross-cutting bands. The highest proportion of X-nodes is counted in CS 34A with 44%, while 40% X-nodes is noted for CS 1A.





 Normal Fault
 Rose Diagram

Figure 5.7: Aerial photo of Klondike East displaying the studied fault intersection with circle sample position and accompanied deformation band orientations (rose plots). Circle samples are not to scale. Aerial photo from Google Earth.

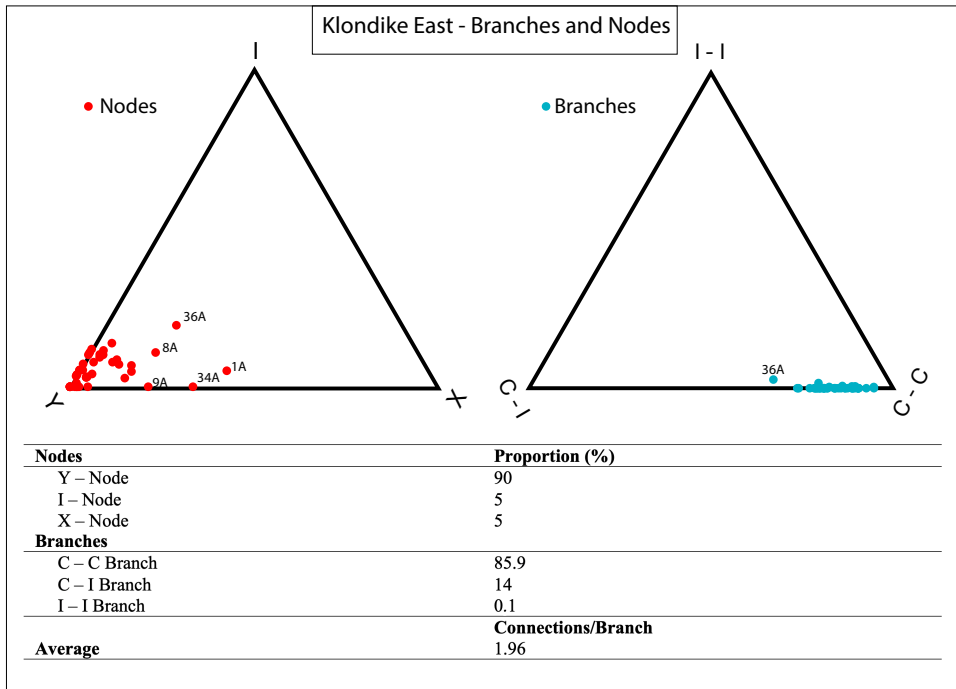


Figure 5.8: Ternary plots showing the node and branch distribution in Klondike East. The table contains information regarding the average proportion of nodes, branches and connections per branch

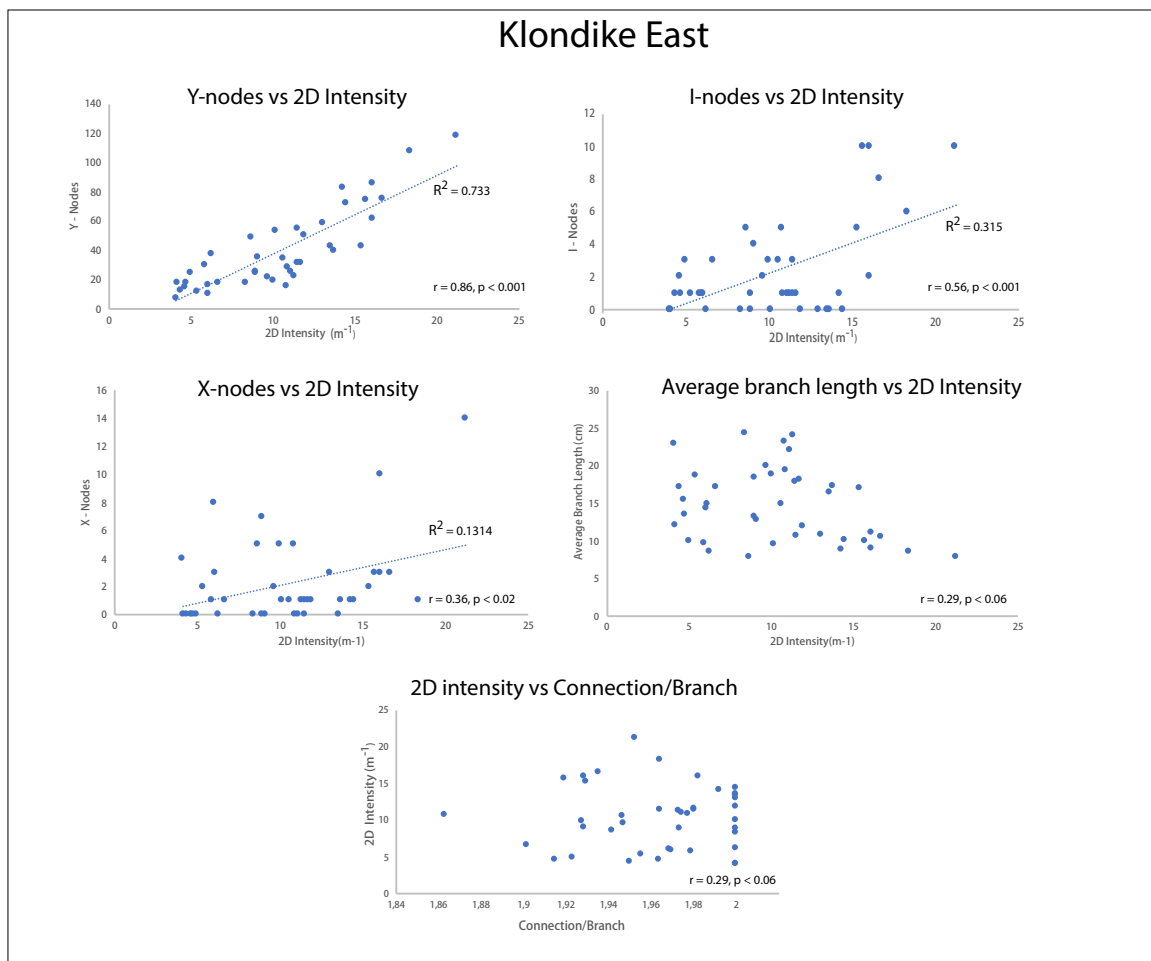


Figure 5.9: Scatterplots of 2D intensity plotted against number of node types, connections/branch and branch length. A positive correlation is observed for 2D intensity and number of Y-nodes and I-nodes. No clear correlation is identified for 2D intensity vs number of X-nodes, branch length or connection/branch (connectivity).

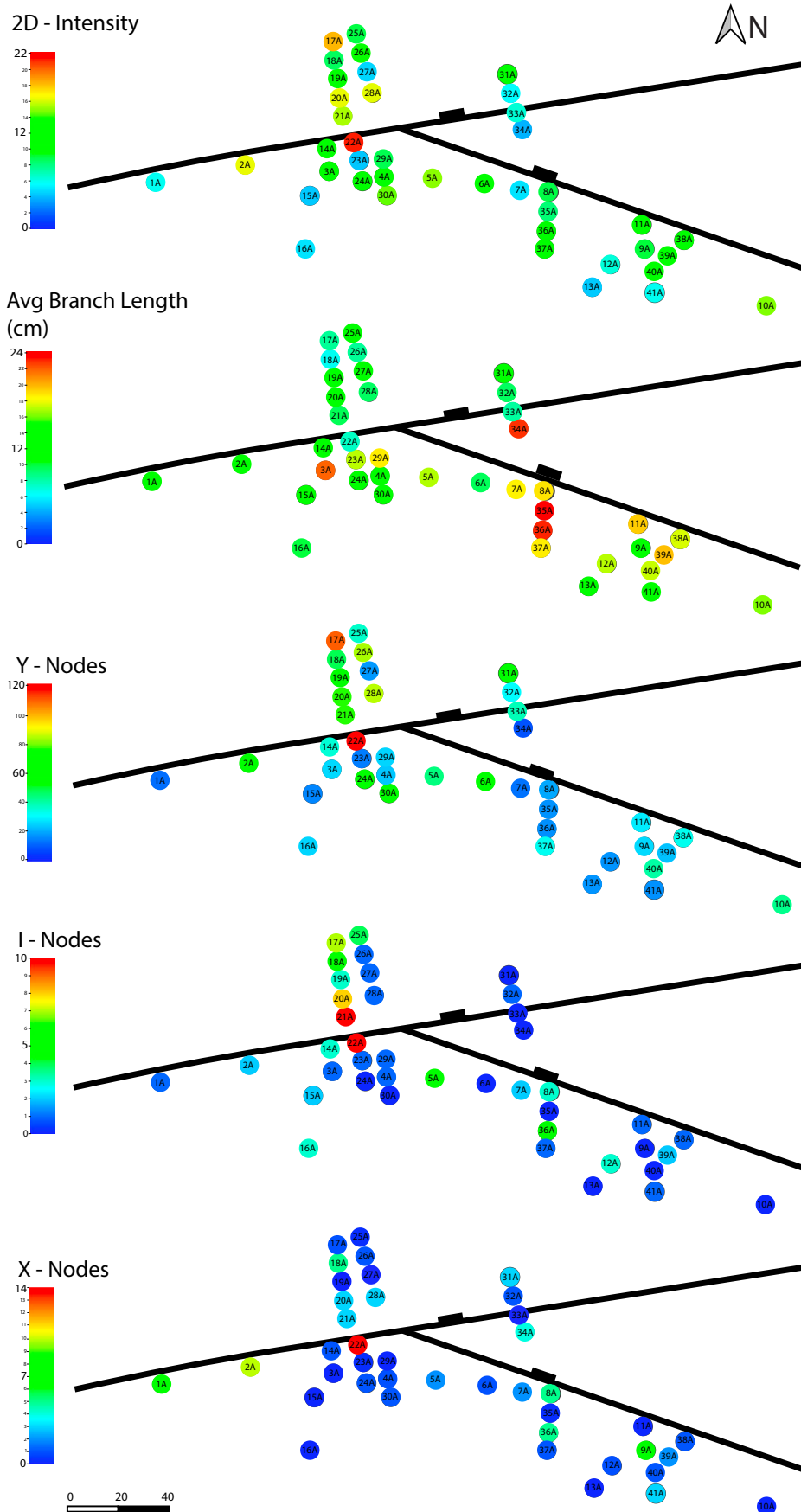


Figure 5.10: Intensity maps of the Klondike East fault intersection demonstrating variations in 2D intensity and node types. The average branch length map display the average branch length within the sample area. Note the different scales in the colour bars.

5.2 Big Hole Fault

The Big Hole Fault is an isolated normal fault in the Chimney Rock Fault Array (Fig.2.2). The fault is c. 4.1 km long, WSW-striking with a 64° N-ward dip (Fig. 5.11a). The displacement increases to a maximum of c. 29 m WSW of the study area, decreasing to c. 17 m near the studied deformation band clusters BC1 and BC2 (Fig. 5.11c,d), and down to c. 8 m displacement close to BC3 (Fig. 5.11b,e) (Shipton & Cowie, 2001; Shipton et al., 2002). The fault offsets the Navajo Sandstone, which in the Big Hole Wash is fine to medium grained with a honey-brown colouration (Fig. 5.12). The damage zone is constrained to the area where the deformation band intensity is high (very few deformation bands occur outside this zone) (Fig. 5.11a). It is exposed in the wash of a river, providing long continuous exposures of cataclastic deformation band clusters and occasional slip surfaces (Shipton et al., 2002; Shipton & Cowie, 2003). These deformation bands form clusters, three of which are presented in detail here (Fig. 5.11d,e) (Shipton et al., 2002).

The three sampled and analysed clusters (BC1, BC2, BC3) along the fault are all situated in the footwall to the Big Hole Fault. Two of the analysed clusters (BC1 and BC2) are located adjacent to each other, just 4 m apart (Fig. 5.11d), whereas the last cluster (BC3) is located further ENE along the fault (Fig. 5.11b,e). The adjacent clusters BC1 and BC2 are therefore described comparatively, whereas BC3 is described separately. All three clusters were sampled by using network grid sampling with a sampling radius of 0.25m.

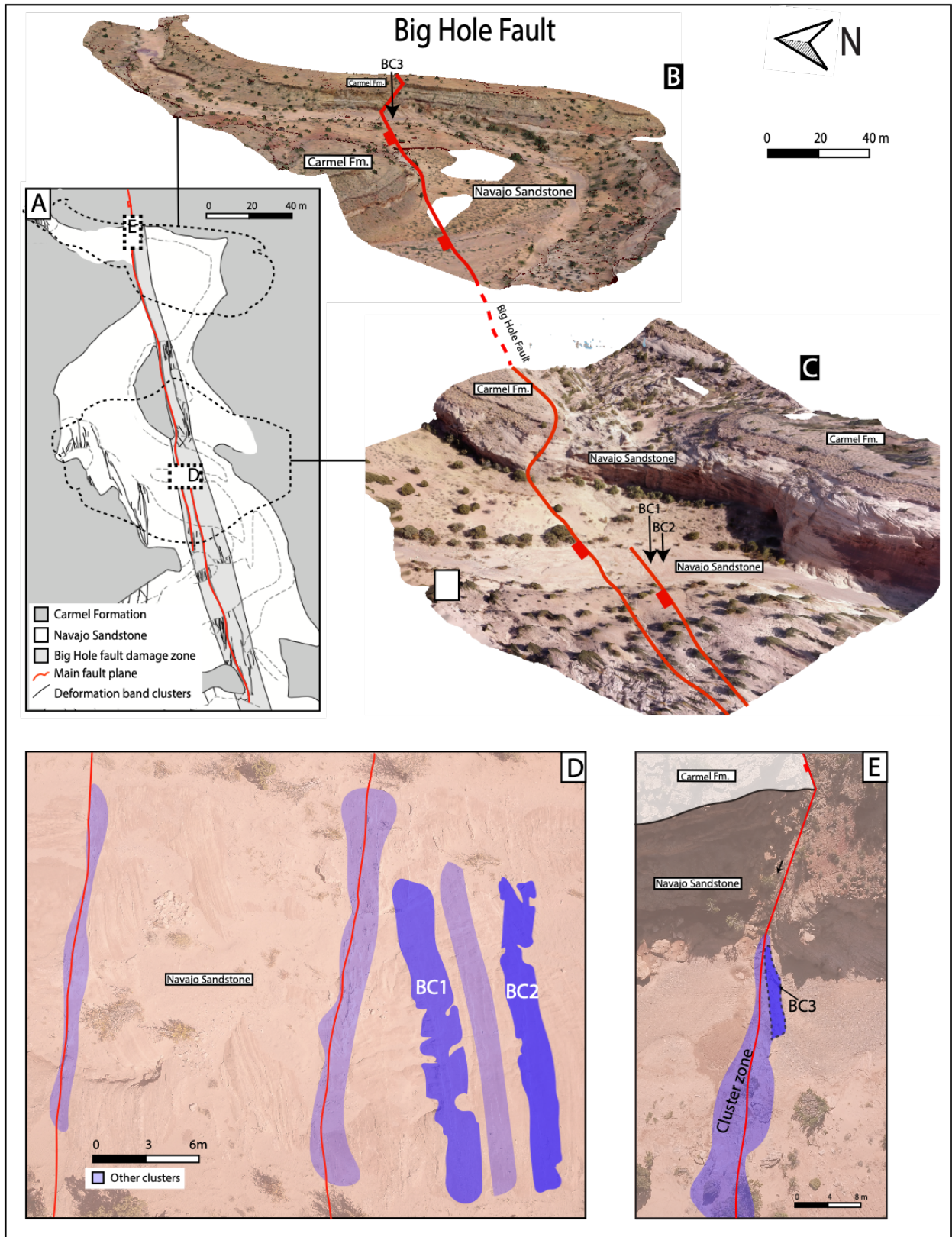


Figure 5.11: Outcrop details and structural features in the Big Hole Fault study area. Each inset figure features the position of the main fault and labelled stratigraphic units. (A) Overview map of the wash in the north-eastern part of the Big Hole Fault with structural features, modified from Shipton et al. (2002). (B) Virtual outcrop model of the eastern part of the study area where BC3 is located, provided by John Howell. (C) Virtual outcrop model of the western part of the study area where BC1 and BC2 is located. (D) Aerial photo of the studied clusters BC1 and BC2 and surrounding clusters. (E) Aerial photo at an oblique angle to the studied BC3 cluster.

5.2.1 BC1 and BC2 clusters

The adjacent clusters BC1 and BC2 trend approximately subparallel to the Big Hole Fault, with BC1 trending slightly more NE-SW than BC2, which are trending more ENE-WSW. Both clusters are well exposed in the wash, measuring c. 16 m in length and c. 2 m in width (Fig. 5.11b). The clusters possibly continue further, but with parts of the area being covered with debris, the study is restricted to the section in the wash. Following the cluster classification presented by Shipton & Cowie (2001), both clusters are classified as a Class 2 cluster with single deformation bands, multi-strand bands, and occasional slip surfaces (Fig. 5.12). The deformation bands in BC1 and BC2 are varying in thickness (0.1 to 3 mm) and they typically cluster to form centimetre-wide zones of several deformation bands. These cluster zones are sometimes recognised as raised relief in outcrop (Fig. 5.12). The deformation band network often displays an anastomosing geometry, where these anastomosing bands tend to confine tens of centimetre-wide and long lenses of pristine rock (Fig. 5.12).

Geometry

BC1 and BC2 cover areas of 40 m² and 38 m², respectively. Both clusters display deformation bands with a clear ENE-WSW trend, approximately parallel to the main fault zone. The spread in orientation is low, ranging between WSW-ENE and E-W (Fig 5.13). Line samples (Fig. 5.13e) demonstrate a reduction in deformation band frequency toward ENE. Although BC1

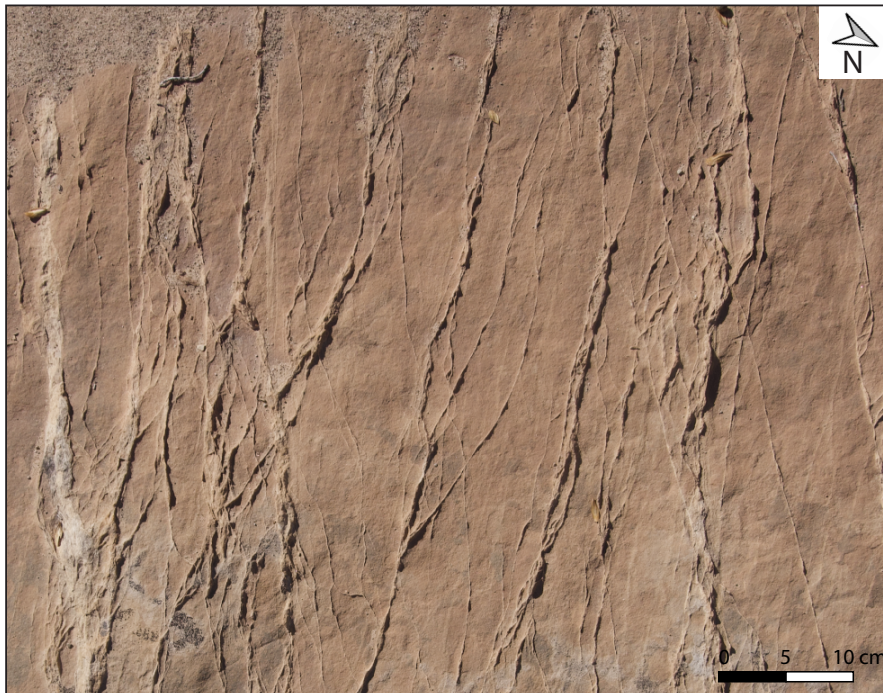


Figure 5.12: Deformation band network exposed along the Big Hole Fault in the Navajo Sandstone. The deformation bands in the area typically vary in thickness (0.1- to 3 mm) and cluster in cm-wide zones.

shows an overall higher deformation band frequency than BC2, they both appear to follow the same trend, with a gradual deformation band intensity decreasing towards ENE (Fig. 5.13e). A similar trend is further recognized in 2D intensity maps, which displays an overall lower 2D intensity in BC2 (Fig. 5.14c and 5.15c).

The average branch lengths for the two clusters are almost identical: 13 cm in BC1 and 13.7 cm in BC2. The average branch length maps show an inverse correlation between branch lengths and 2D intensity (Fig. 5.14c,d and 5.15c,d). Scatterplots show that high 2D intensities mainly correspond to short branches. Furthermore, identified blocks demonstrate the compartmentalization within the clusters, where high 2D intensity is coupled with small compartments and short branch lengths, and vice versa (Fig. 5.14b,d and 5.15b,d). Furthermore, the block analysis shows an average block size of 0.01 m² for both clusters, although the compartment proportion is significantly higher in BC1 (42% to 17%). Hence, larger compartments (1.23 m²) are observed in BC2 compared to BC1 (0,54 m²).

Topology

The compiled data (Fig. 5.14h and 5.15h) shows a dominance of Y-nodes and doubly connected branches, resulting in deformation band clusters with high connectivity; 1.96 for BC1 and 1.94 for BC2. Additionally, scatterplots demonstrate that high 2D intensity corresponds to high connectivity (Fig. 5.16). The intensity distribution of Y-nodes displays similar trends to the 2D intensity (Fig. 5.14c,e and 5.15c,e). Scatterplots of the whole network grid show a strong positive correlation between 2D intensity and the number of Y-nodes for both BC1 and BC2 (Fig. 5.16). The I- and X-nodes are more scattered throughout the cluster zones and are in many areas absent. Intensity maps indicate that the distribution of the two node types coincide with increased 2D intensity (Fig. 5.14c,f,g and 5.15c,f,g). Scatterplots further demonstrate a moderate correlation between 2D intensity and the number of I-nodes, both for BC1 and BC2 (Fig. 5.16). X-nodes display a similar correlation for BC1 and BC2 (Fig. 5.16). The two clusters display only minor differences in topological characteristics; BC1 has a slightly higher proportion of X- and I-nodes, which in addition are wider distributed throughout the cluster (Fig. 5.14f,g and 5.15f,g).

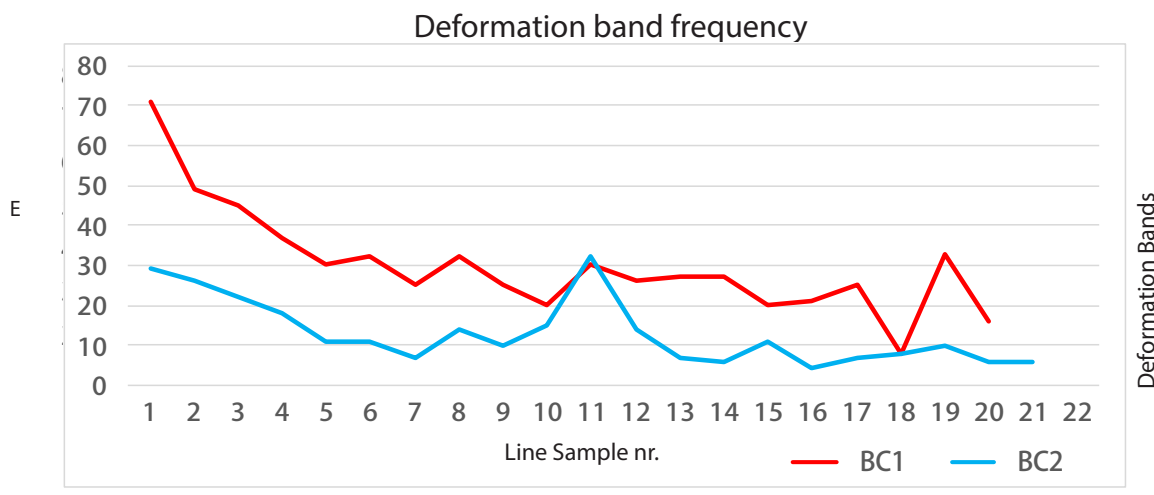
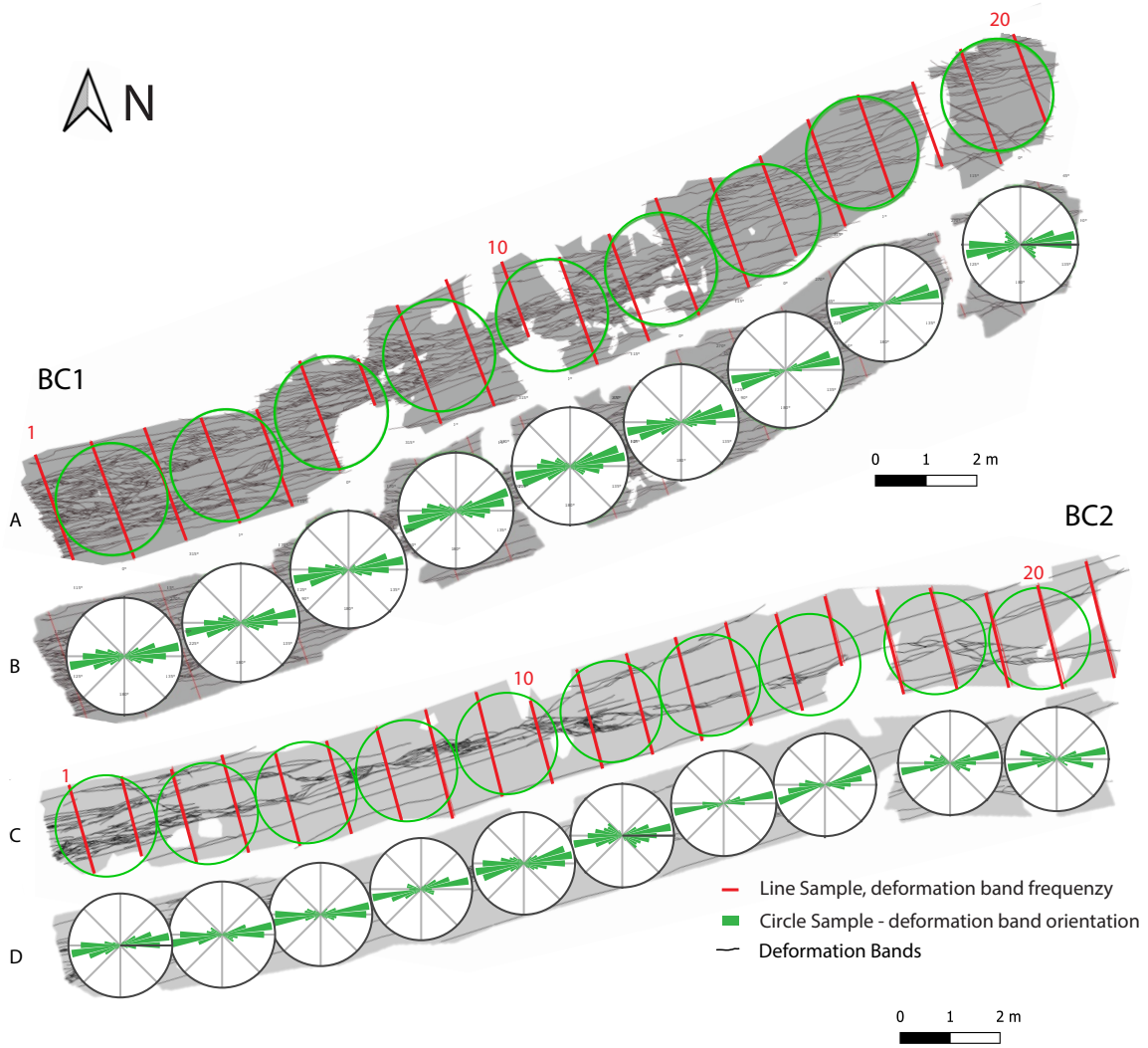


Figure 5.13: Overview map of BC1 and BC2 deformation band networks with deformation band orientations (rose plots) and frequencies. A) BC1 deformation band network with line sample- and rose plot locations. B) BC1 with deformation band orientations (rose plots). C) BC2 deformation band network with line sample- and rose plot locations.. D) BC2 deformation band orientations (rose plots). E) Diagram showing the frequency distribution of deformation bands within BC1 and BC2

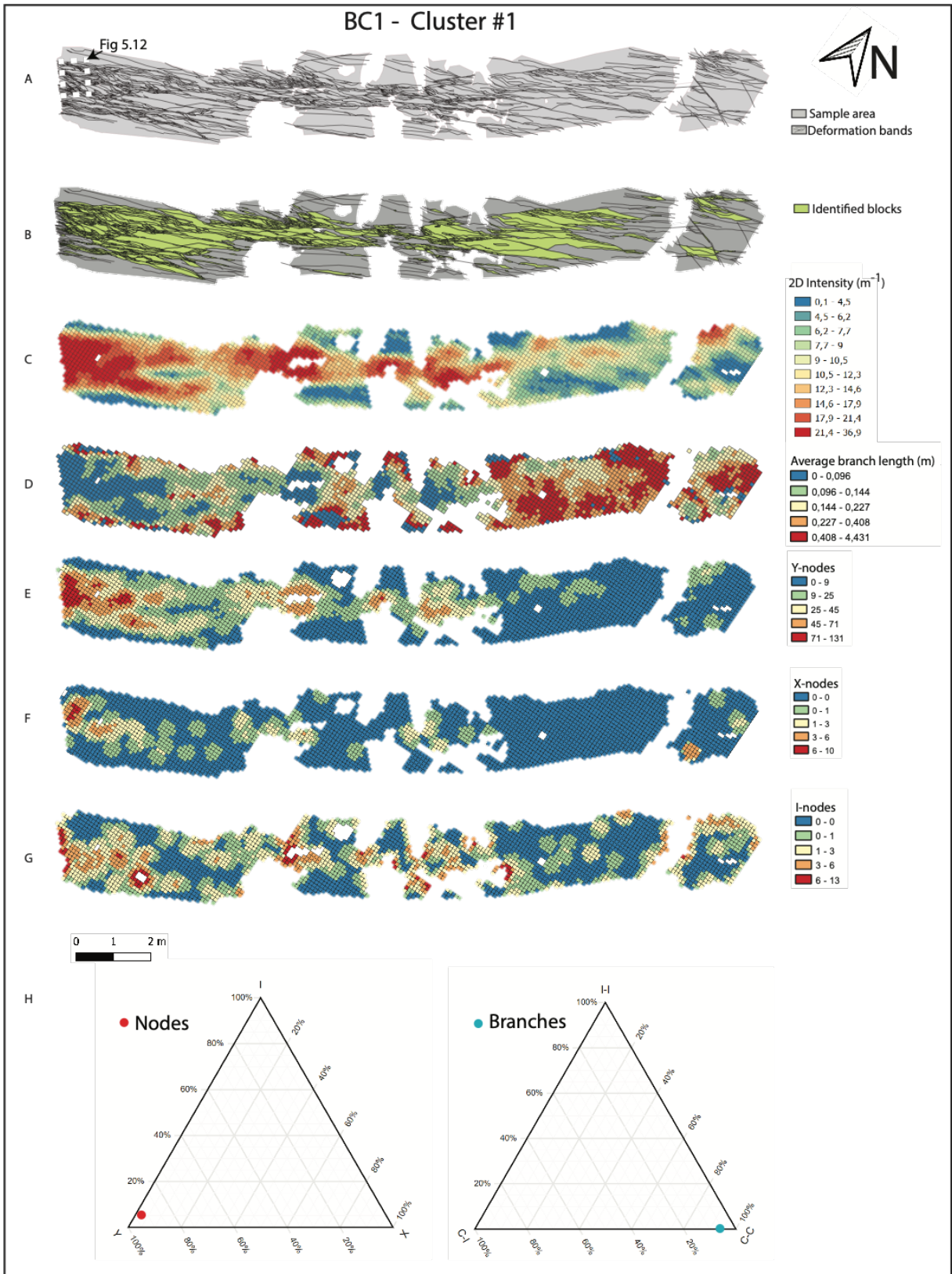


Figure 5.14: BC1: deformation band network outline and various intensity maps displaying differences and similarities in topological and geometrical characteristics. A) The BC1 deformation band network. B) Identified blocks within BC1. C) 2D intensity variation. D) Average branch length distribution. E) Number of Y-nodes. F) Number of X-nodes. G) Number of I-nodes. H) Ternary plot of node and branch distribution.

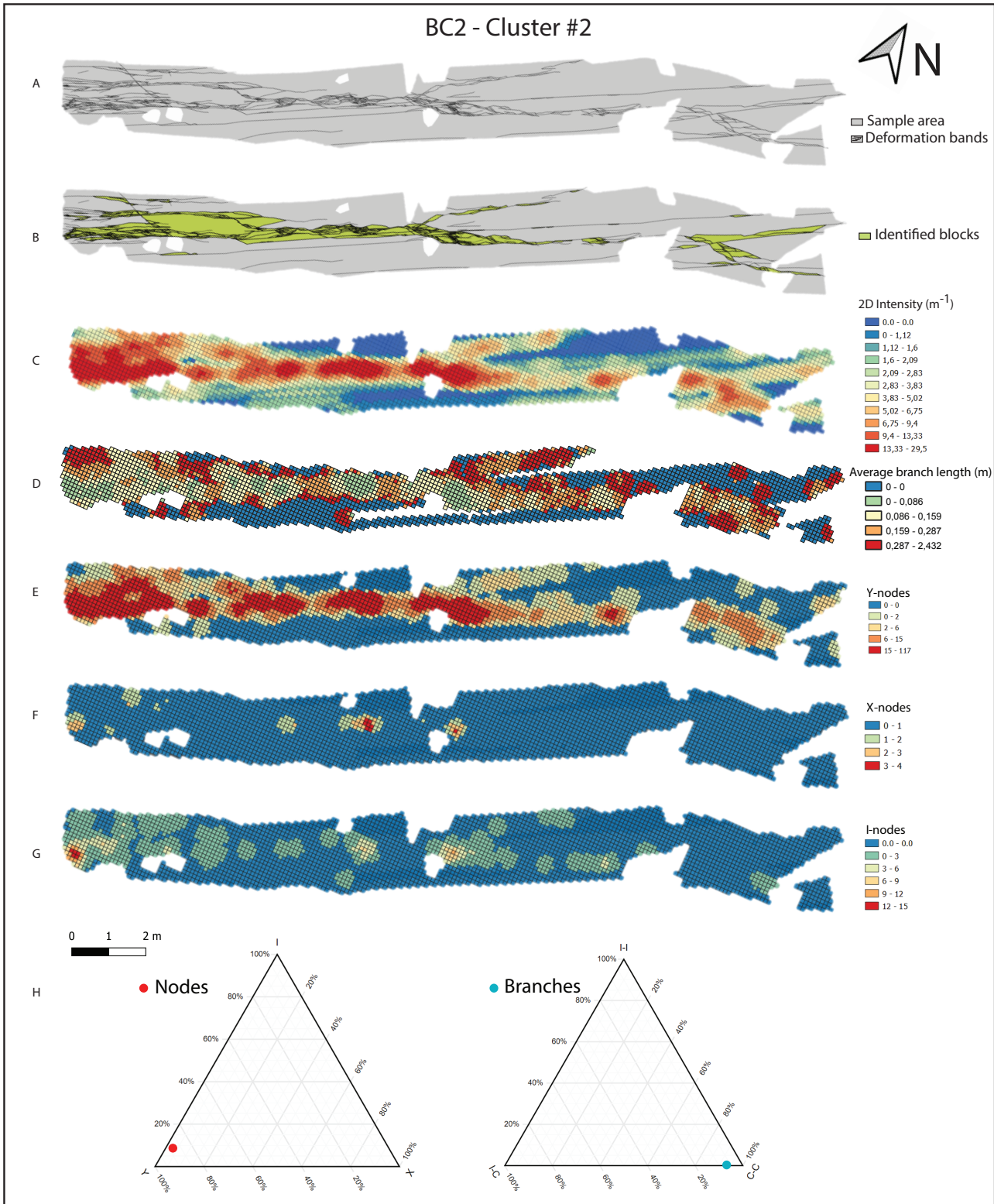


Figure 5.15: BC2: deformation band network outline and various intensity maps displaying differences and similarities in topological and geometrical characteristics. A) The BC2 deformation band network. B) Identified blocks within BC2. C) 2D intensity variation. D) Average branch length distribution. E) Number of Y-nodes. F) Number of X-nodes. G) Number of I-nodes. H) Ternary plot of node and branch distribution.

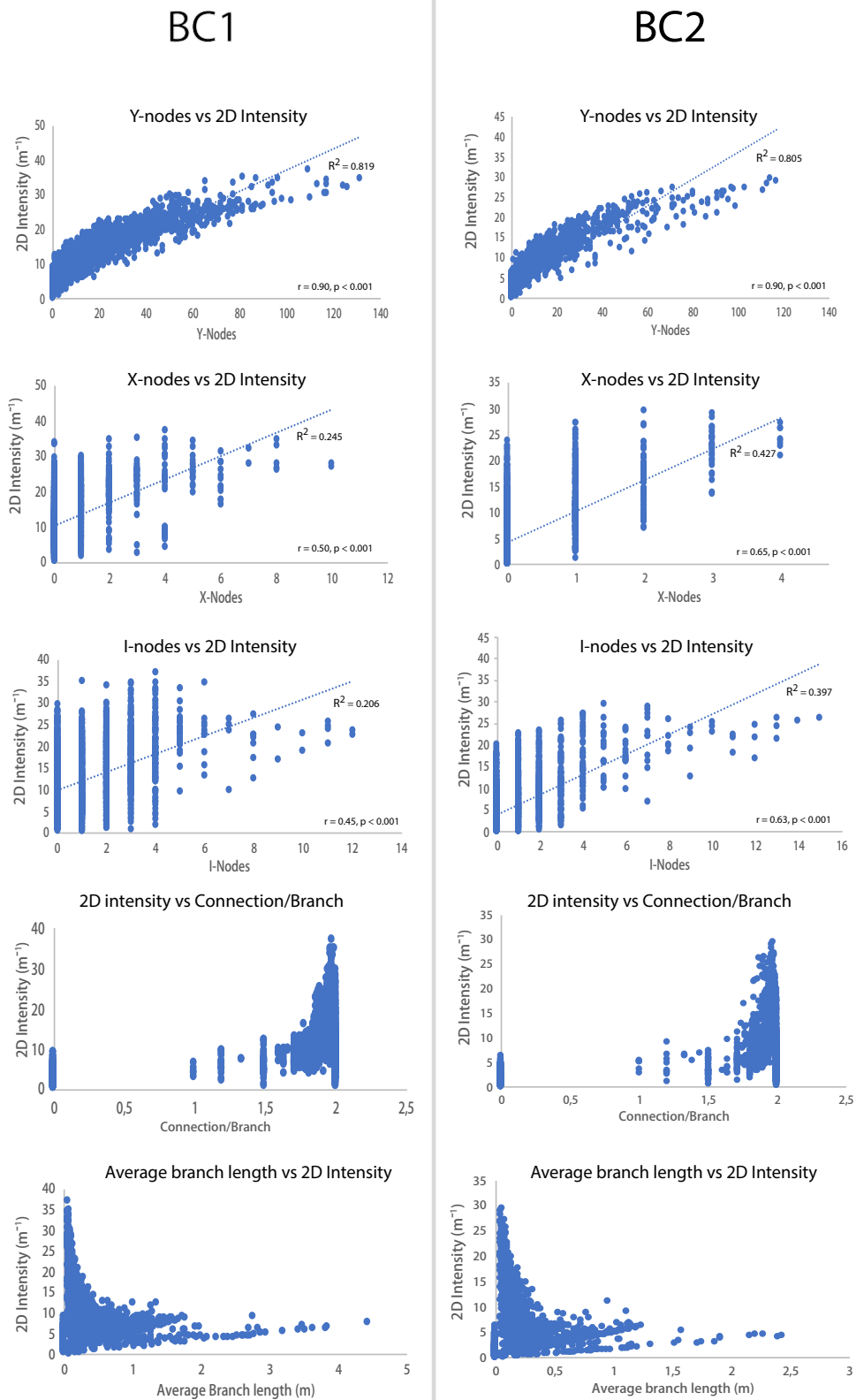


Figure 5.16: Data from BC1 and BC2 compiled in scatterplots of 2D intensity plotted against number of node types, connections/branch and branch length. A positive correlation is observed for 2D intensity and number of Y, X and I-nodes. High 2D intensity corresponds to high connectivity and shorter branch lengths.

5.2.2 BC3 cluster

The study of BC3 is restricted to the southern end of a larger cluster zone (Fig. 5.11b,e), which covers an area of about 16 m². The BC3 cluster is oriented E-W and is classified as a class 3 cluster according to Shipton & Cowie (2001). A class 3 cluster is characterized by an anastomosing network of both deformation bands and slip surfaces (Fig. 5.17). The deformation band thickness is variable (0.1- 1.5 mm), and the bands tend to cluster in centimetre-wide zones, occasionally forming a raised relief in outcrop. In addition, BC3 features slip surfaces, which are associated with zones of parallel to sub-parallel deformation bands (Fig. 5.17 and 5.18).

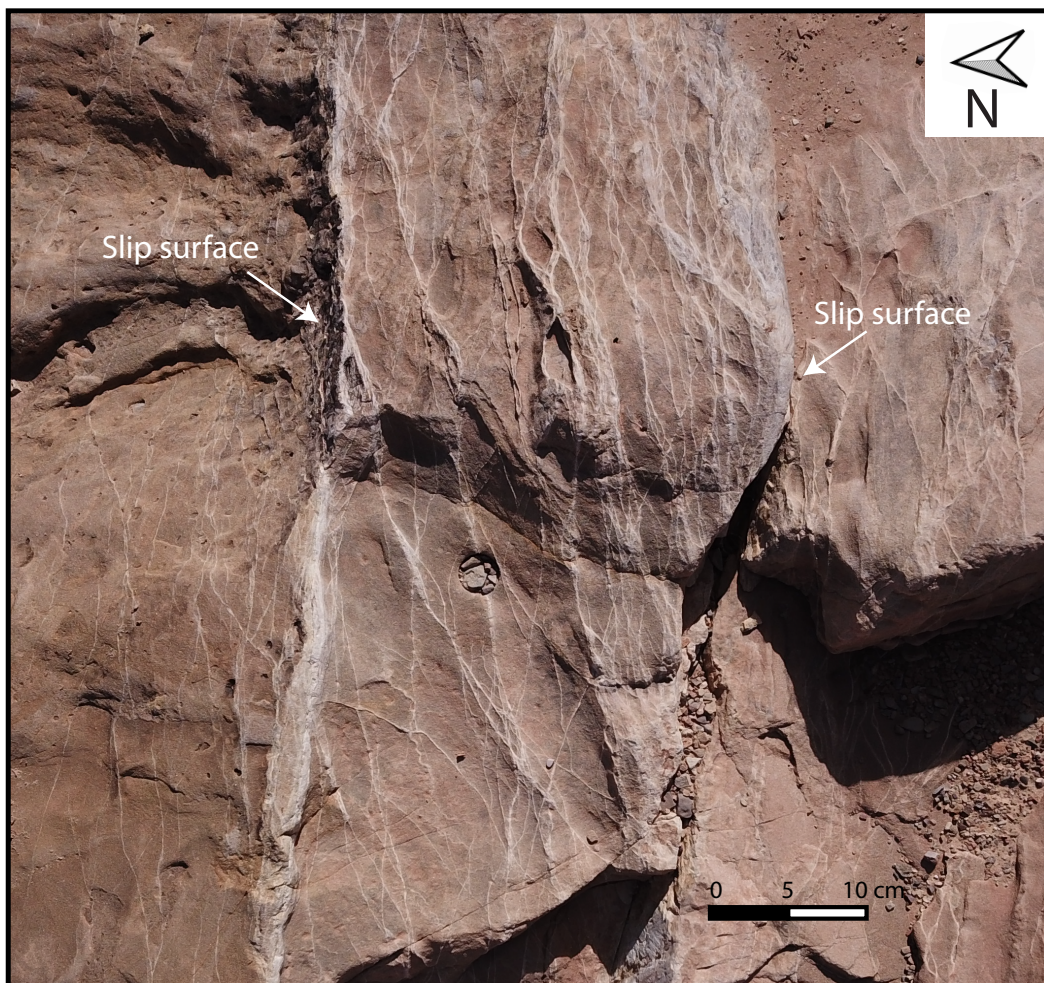


Figure 5.17: Anastomosing deformation bands within the BC3 in the Navajo Sandstone (Big Hole Fault), bounded by two synthetic slip surfaces. The band thickness is vary between 0.1 – 1.5 mm, and typically cluster to form cm wide raised relief in outcrop. The position of this photo is shown in Fig. 5.18.

Geometry

Overall the deformation bands in BC3 trend more or less parallel with the Big Hole fault (Fig. 5.18). However, rose plots display a larger spread in orientation compared to BC1 and BC2. The spread in orientation is fairly high in some areas where the 2D intensity and deformation band frequency are rather high (Fig. 5.18c and 5.20c). These high 2D intensity areas generally coincide with areas with developed slip surfaces (Fig. 5.20a,c). The highest 2D intensities are observed within the area that are bounded by the two slip surfaces, this area also displays a larger spread in deformation bands orientation (Fig. 5.18 and 5.20c). Furthermore, small compartments (5.19b) and a fairly low average branch length characterize these areas. The total deformation band network has an average branch length of 11.2 cm and an average compartment size of 0.014 m² (Fig. 5.20b). Overall it appears that high 2D intensities coincide with short branches (low average branch lengths) (Fig. 5.19).

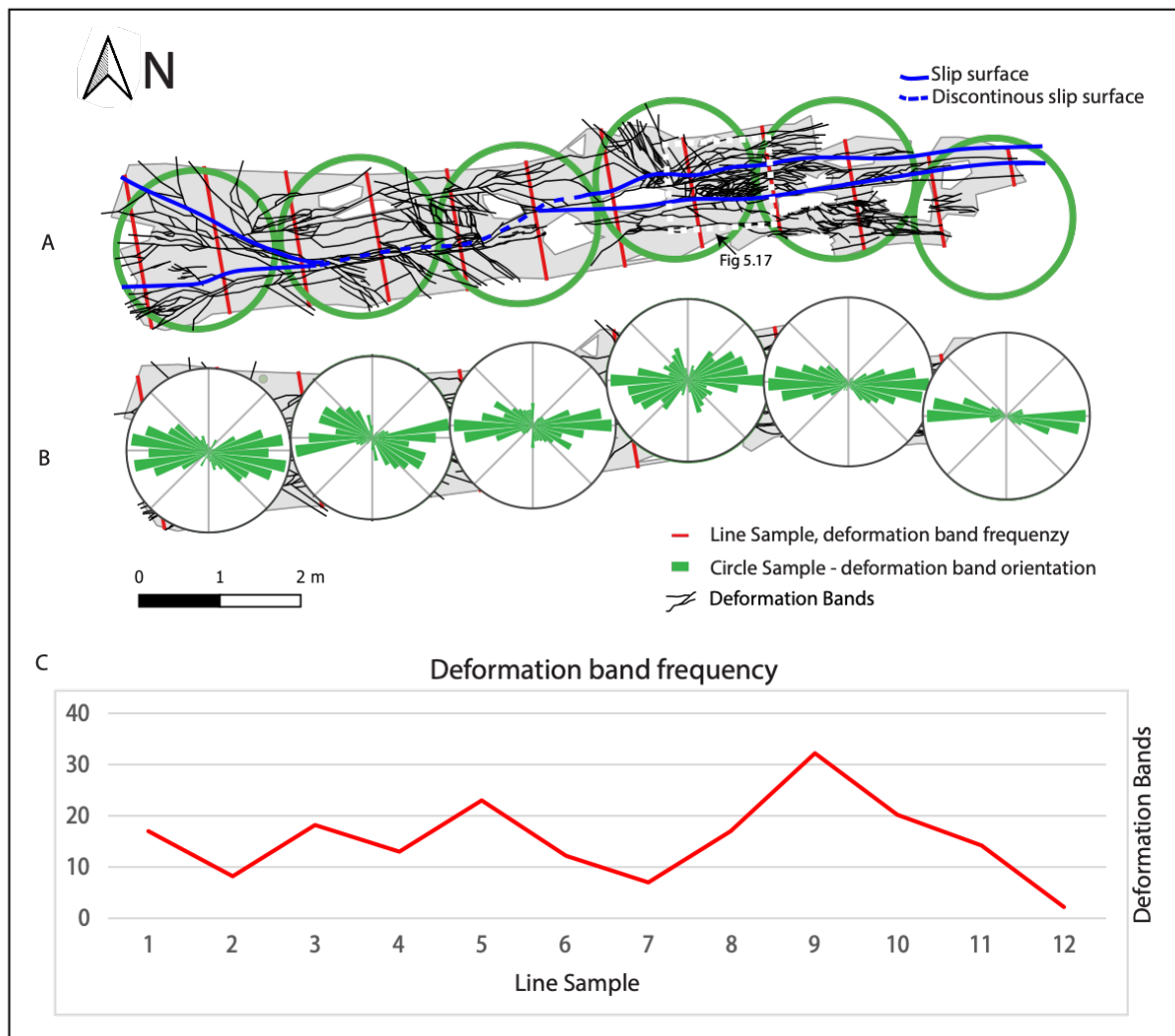


Figure 5.18: The BC3 deformation band network with deformation band orientations and frequency: A) Deformation band network with line sample- and rose plot positions. B) Deformation band orientations (rose plots). C) Diagram showing the frequency distribution of deformation bands.

Topology

BC3 is dominated by Y-nodes and doubly connected branches. X- and I-nodes constitute respectively 10.8% and 9.4% of the network (Fig 5.20h). The connectivity (connections per branch) of the deformation band network is thus high (1.93). The distribution of Y-, I- and X-nodes follows the 2D intensity distribution (5.20c,e,f,g). A strong correlation is noted between 2D intensity and number of Y-nodes, while there is a moderate correlation between 2D intensity and number of I-nodes and X-nodes (Fig. 5.19). While absent in most areas, the few areas containing a high X-node intensity often display an additional large spread in deformation band orientation, which often are in proximity to slip surfaces and/or slip surface intersections (Fig. 5.20f).

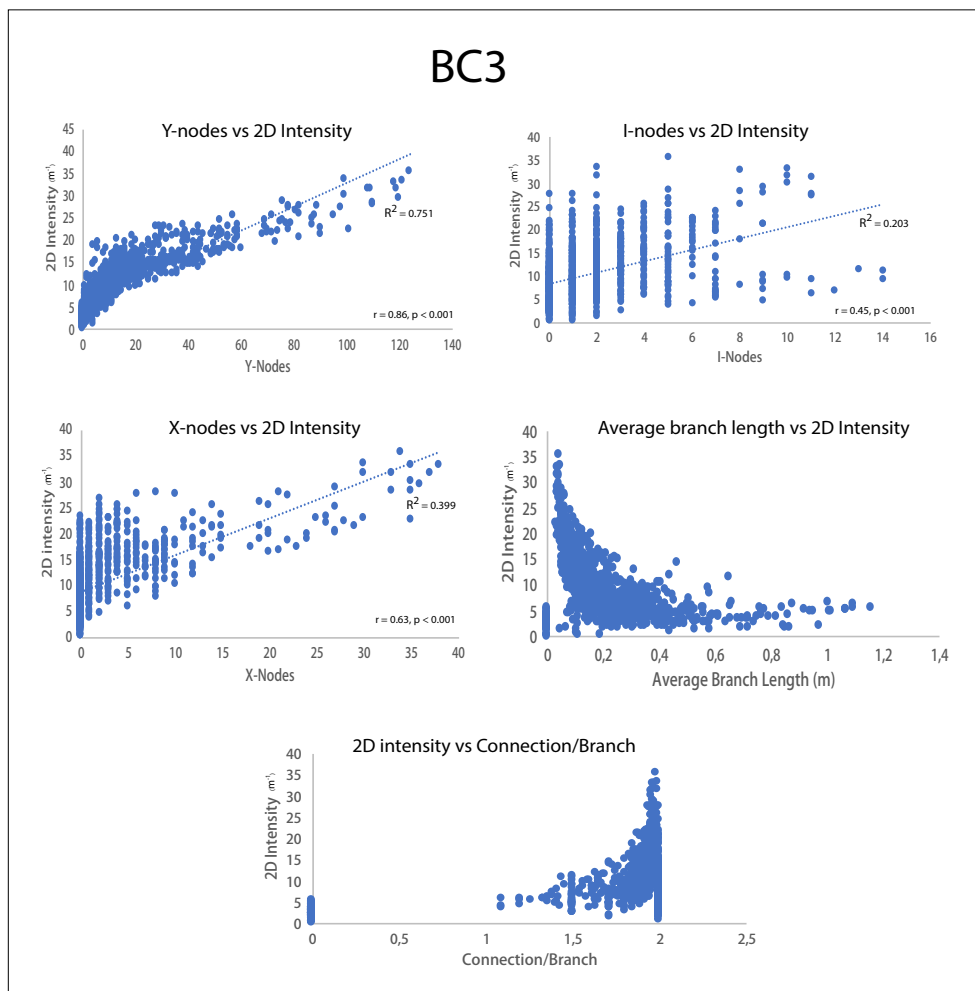


Figure 5.19: Data from BC1 and BC2 presented in scatterplots of 2D intensity plotted against number of node types, connections/branch and branch length. A positive correlation is observed for 2D intensity and number of Y, X and I-nodes. High 2D intensity corresponds to high connectivity and shorter branch lengths.

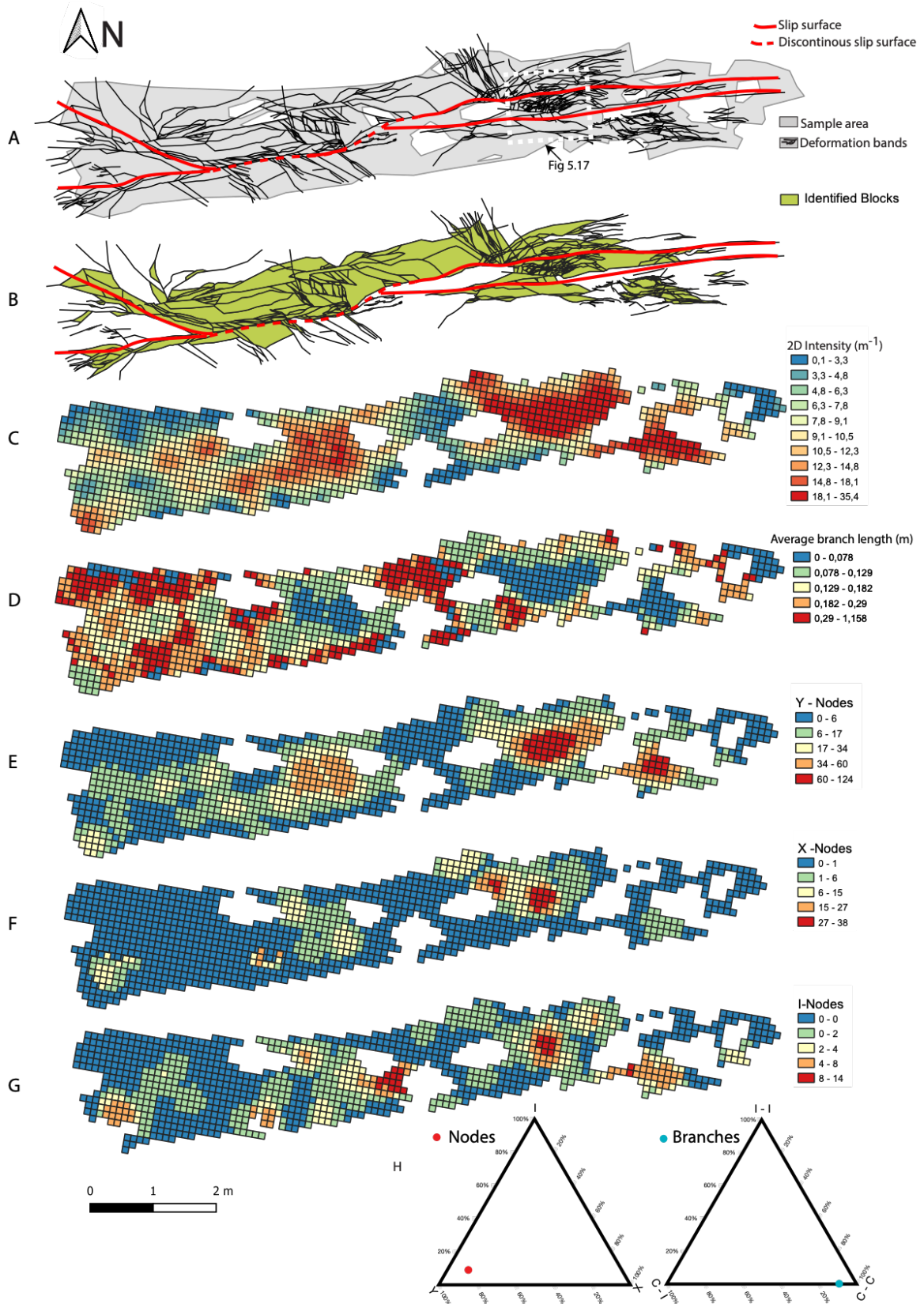


Figure 5.20: The BC3 deformation band network and various intensity maps displaying differences and similarities in topological and geometrical characteristics: A) the BC3 deformation band network. B) Identified blocks within BC3. C) 2D intensity variation. D) Average branch length distribution. E) Number of Y-nodes. F) Number of X-nodes. G) Number of I-nodes. H) Ternary plot of node and branch distribution

6 Discussion

This chapter addresses the topological similarities, differences, and spatial variability in the studied damage zones (Section 6.1). The documented topological trends are used to discuss the evolution of a deformation band network (Section 6.2), and the topological characteristics are compared to those of other types of structural networks (Section 6.3). Finally, the implications for fluid flow (Section 6.4) and the applicability of topology in well data analysis are reflected upon (Section 6.5).

6.1 Geometrical and topological similarities and differences between deformation band networks in intersection damage zones and wall damage zones.

Deformation bands in proximity to faults and slip surfaces commonly occur as interconnected networks (Aydin & Johnson, 1978). In this study, a topological approach is used to characterize these deformation band networks, assessing their connectivity, distribution, and orientation. Five deformation band networks were mapped in cm to mm detail for topological characteristics: three clusters in wall damage zones, and two intersection damage zone networks, located in the San Rafael Swell and the Paradox Basin, eastern Utah, respectively.

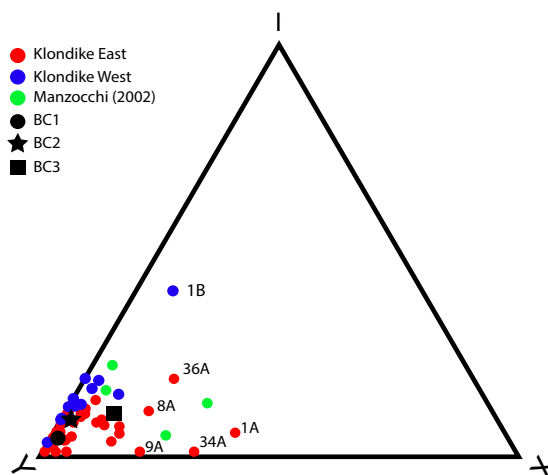


Figure 6.1: Ternary diagram displaying the nodal distribution of all the collected topological data in this thesis. In addition, the deformation band observations from Manzocchi (2002) is shown (green).

All five deformation band networks demonstrate a high proportion of Y-nodes and doubly connected branches. The nodal distribution is more or less identical throughout the deformation band networks, which all display consistently high Y-node proportion (Fig. 6.1). However, some spatial variations in topology occur within the networks. The observed topology in the five deformation band networks is consistent with findings in other studies that have pointed out how closely spaced bands tend to bifurcate and intersect, forming hard-linked deformation bands (e.g. Ayidin & Johnson 1978; Fossen & Hesthammer, 1997). The high Y-node proportion further coincides with observations by Manzocchi (2002), who plot deformation band networks with a fairly high Y-node proportion (Fig. 6.1). The high Y-node proportion can be explained by increased strain, causing bands during growth to link and form more densely spaced bands, which splay or abut (Fossen & Hesthammer, 1997). This is further demonstrated with a positive correlation between number of Y-nodes and 2D intensity (Fig. 5.5, 5.9, 5.16, and 5.19), indicating that increased strain will cause bands to bifurcate and abut.

The proportion of X-nodes is fairly low, corresponding well with Ayidin & Johnson (1978) observations that cross-cutting deformation bands (X-nodes) are rarely observed. One could argue that cross-cutting deformation bands will most likely offset and form two Y-nodes instead of one X-node. Thus, a higher proportion of Y-nodes relative to X-nodes is expected, as emphasised by Morley & Nixon (2016) in their study of faults. However, crossing deformation bands are rarely observed. For this reason, cross-cutting bands are not considered a valid explanation for the high Y-node proportion, but it could cause reductions in the total number of X-nodes. An interesting observation is the positive correlation between number of X-nodes and 2D intensity (Fig. 5.9, 5.16 and 5.19), which indicates that a higher amount of strain can be associated with more crossing deformation bands. Manzocchi (2002) plots topology of deformation band with a slightly higher X-node proportion than the majority of the results in this study (Fig. 6.1). The X-node discrepancy could be explained by a more subjective node and branch identification when the data resolution is low (Morley & Nixon, 2016). The data resolution in this study is fairly high. It is thus stressed that several deformation bands in this study appeared at m to cm scale to be crossing, but at mm scale some offset was usually revealed. This will result in a lower X-node count and may explain the higher X-node count by Manzocchi (2002). However, some of the data collected in Klondike deviate from the main trend and display a similar X-node proportion to the ones documented by Manzocchi (2002) (Fig 6.1). This could be explained by a possible sampling bias. The results show that X-nodes

mainly occur in areas associated with high strain. However, the circle samples from Klondike demonstrates that X-nodes can occur in low strain areas as well. Circle samples with low 2D intensity (low strain) coupled with presence of X-nodes will display a larger proportion of X-nodes, which may not be representing the overall node distribution in that area. The data from the circle samples therefore need to be studied with care. It is further stressed that circle samples can indicate a high strain (2D intensity) that might not be representative for the overall deformation band intensity in the area. This is due to limited exposure, and the fact that clusters can appear both close and further away from a fault (Schueller et al., 2013).

The proportion of I-nodes is overall low compared to the Y-node proportion, but generally higher than the X-node proportion (Fig. 6.1). Along with the other node types, number of I-nodes is also increasing with increased 2D intensity (Fig. 5.5, 5.9, 5.16 and 5.19). It is slightly counterintuitive that I-node concentration is increasing with 2D intensity though, as you would expect low strain to be associated with less interactions and more isolated branches (Morley & Nixon, 2016). The longer continuous transects exhibit clusters, where the overall 2D intensity is fairly high, and observations interestingly show that I-nodes form in these high 2D intensity areas (Fig. 6.2). An explanation could be that cluster compact and thicken as shear displacement accumulates (Fossen et al., 2018), where the density of deformation bands numbers within the clusters increase as the clusters mature (Johansen & Fossen, 2008). The probability of closely spaced deformation bands will then increase and linking bands may form between two overlapping bands due to increased stress magnitudes (Schultz & Balasko, 2003). These linking bands can form both soft-linked and hard-linked networks (Fossen & Hesthammer, 1997), and can as such explain the observed trend in this study: the hard-linked deformation band interaction described by Fossen & Hesthammer (1997) will contribute to more Y-nodes, while the development of soft-linked deformation bands, such as splaying deformation bands, will contribute to more I-nodes (Fig. 6.2). A second explanation for why I-nodes is associated with

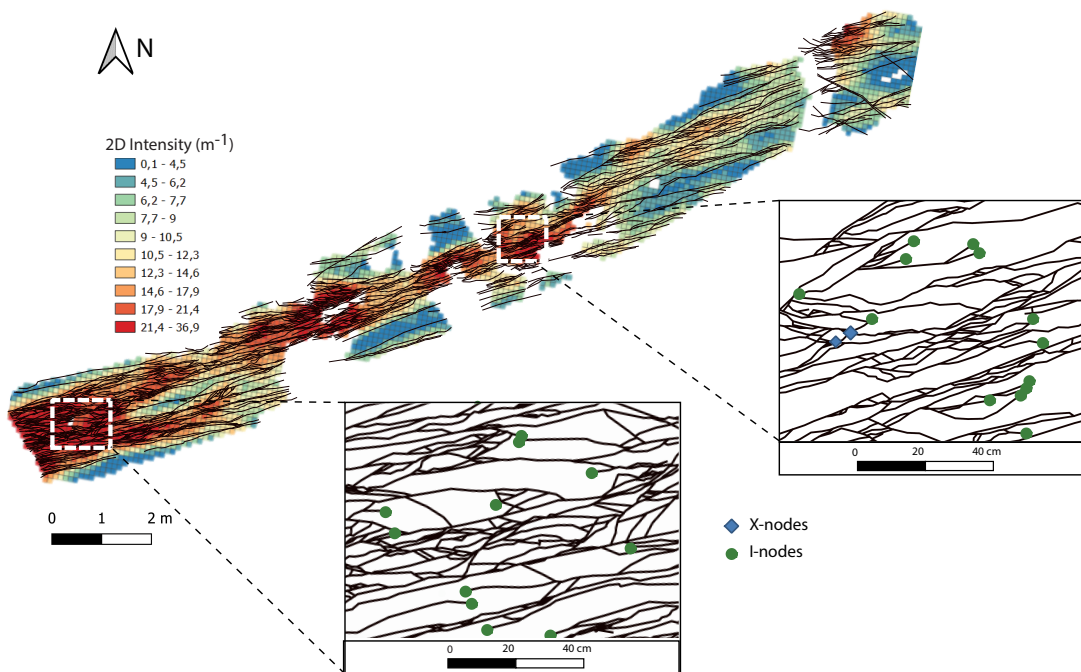


Figure 6.2: 2D intensity map of BC1, illustrates that high 2D intensity areas display a fairly high proportion of I-nodes, and some X-nodes. Both soft linked and splaying deformation bands can be identified.

areas of high deformation band intensity is through the sampling approach used in this thesis. The sampling method does not cover isolated deformation bands, which is defined as bands that do not interfere with other bands, and where the tip points are more than 40 cm away from each other (Fossen and Hesthammer, 1997). The sampling strategy used in this thesis would in most cases not capture this trend as the circle samples are only 0.5 m in radius and preferably placed in areas where more than one deformation band is present (as described in methods, chapter 4).

The high proportion of Y-nodes and doubly connected branches result in deformation band networks of high connectivity (connections per branch) (Sanderson & Nixon, 2015). The average connectivity in the studied damage zones is in the range of 1.92 and 1.96, observed in Klondike West and BC1, respectively. The values reflect an overall high connectivity for both damage zones. Moreover, the clusters along Big Hole Fault show a positive correlation between 2D intensity and connectivity (Fig. 5.16 and 5.19), which suggests that areas with high strain can be expected to display high connectivity. There is, however, a discrepancy from this trend, where relatively low deformation band intensities cause maximum connectivity. Yet, the high 2D intensities (20 to 40 m^{-1}) are consistently associated with high connectivity (Fig. 5.16 and

5.19). This implies that clusters, and in general areas of high strain, typically can be associated with deformation band networks with high connectivity. It is stressed that this trend of high intensity-high connectivity is not observed in any of the intersection damage zones. The studied intersection damage zones display an overall lower 2D intensity compared to wall damage zones and could therefore explain why these trends are not observed in intersection damage zones. The highest 2D intensities measured in intersection damage zones is 22 m^{-1} (Fig. 5.10), while intensities up to 37 m^{-1} is observed within the wall damage zone clusters (Fig. 5.14c). One explanation for this could be the different sampling approaches, where the clusters have been mapped with network grid, comprised of circle samples with 0.25 m in radius, while the intersection damage zones have been mapped with circle samples of 0.5 m in radius. However, the high 2D intensity is fairly consistent along the clusters (Fig. 5.14c and 5.15c), and this explanation is thus not covering. Another, more likely, explanation is related to the observed tendency of more widely oriented deformation bands in intersection damage zones; This results in a more complex deformation band network, where bands link and intersect with a wider range of orientations, forming a more compartmentalized zone than wall damage zones that typically develop dense clusters with densely spaced bands (Shipton & Cowie, 2003; Fossen et al., 2005).

The studied clusters from Big Hole Wash demonstrate that damage zones grow with a constant balance between the development of new deformation bands within the existing damage zone and new deformation bands forming outside the zone (Shipton & Cowie, 2003; Fossen et al., 2018). This is evident by comparing the results from BC1 and BC2 (Fig. 6.3), where BC1 is both wider and have a larger area with high 2D intensities compared to BC2. In addition, BC1 comprise 42% closed compartments/blocks in BC1, compared to 17% in BC2 (Fig. 5.14b and Fig. 5.15b). Moreover, the deformation band frequency decreases in both clusters towards ENE, even though the frequency is overall higher in BC1 (Fig. 6.3). These findings suggest that more mature clusters can be expected closer to the main fault. Furthermore, the results coincide with observations that clusters closest to the fault core, generally display higher intensities of deformation bands than the peripheral clusters (Schueller et al., 2013). This indicates the new clusters form peripherally, while the pre-existing clusters continue to grow and compact (more densely spaced bands) (Johansen & Fossen, 2008; Fossen et al., 2018).

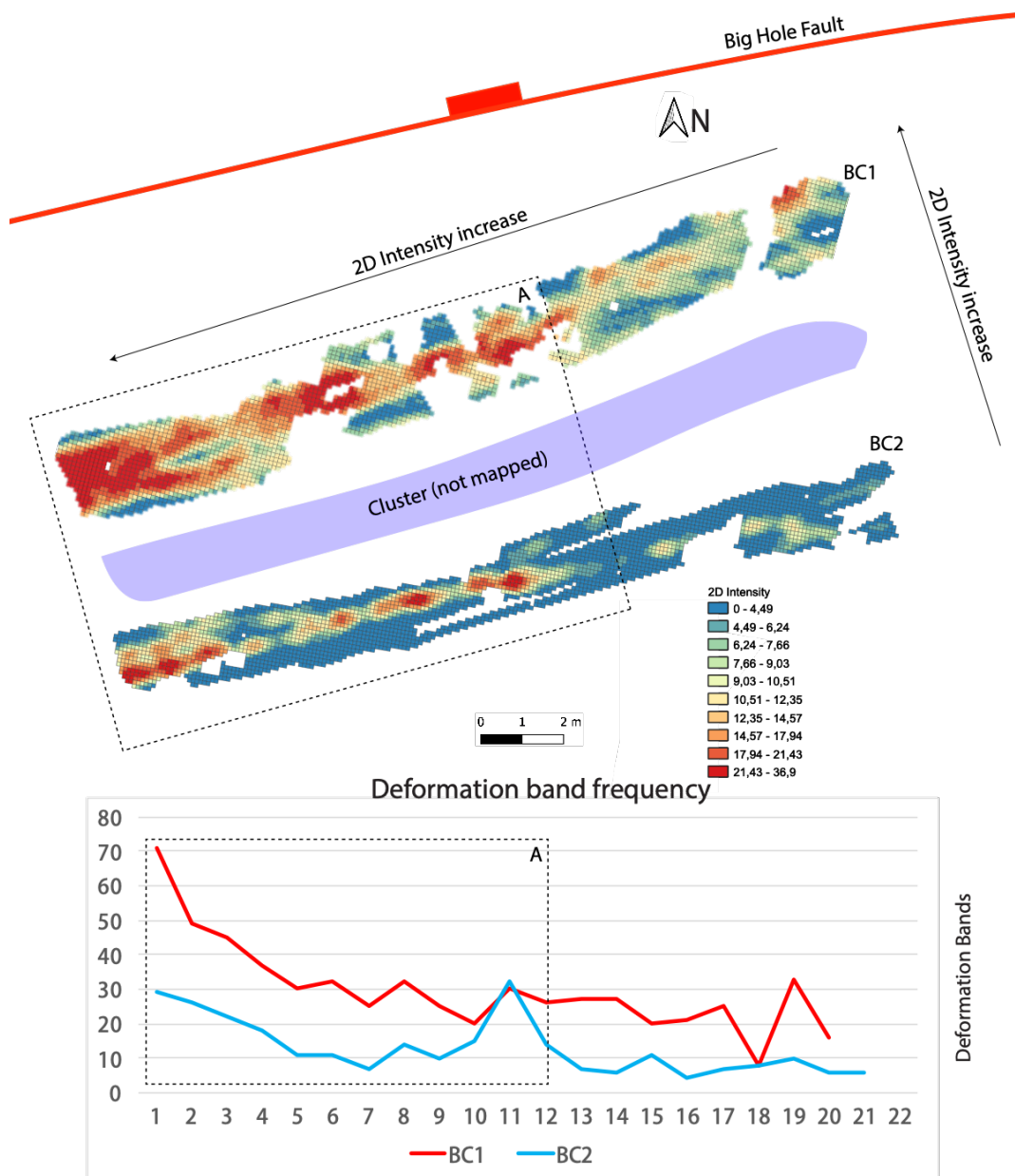


Figure 6.3: BC1 and BC2 2D intensity maps coupled with deformation band frequency. The dotted square highlights the area in the 2D intensity that correspond to the same area in the deformation band frequency plot. The deformation band frequency plot is compiled of line samples, for the line sample positions see Fig. 5.13

Mature clusters usually host closely spaced bands, which can result in local stress perturbation and mechanical interaction between deformation bands, influencing the orientation and the geometry of the deformation bands (Fossen & Hesthammer, 1997; Johansen & Fossen, 2008). Results in this study show no clear correlation between the orientation of deformation bands and the deformation band intensity in any of the five deformation band networks. It appears that the spread in orientation, however, is greater in deformation band networks in intersection

damage zones than in wall damage zones (Fig. 5.3, 5.7, 5.13). Areas exhibiting more complex deformation (e.g. bifurcation, linkage and bends) and wider damage zones commonly result from an increased stress and/or stress perturbation within the zone (e.g. Rawnsley et al., 1992; Aarland & Skjerven, 1998; Berg & Skar, 2005). This perturbed stress can cause a rotation in principal stresses, which will result in a rotation of smaller-scale discrete structures (e.g. Rawnsley et al., 1992; Fossen & Rotevatn, 2016). Such stress increase and stress perturbation occur at fault tips and at fault interaction points (e.g. Segall & Pollard, 1980; Childs et al., 1995; Johansen et al., 2005; Fossen et al., 2005). A likely explanation for the larger spread in deformation band orientation within intersection damage zones could thus be perturbed stresses as the two faults intersect, forming a more complex deformation band network. On a larger scale this implies that intersection damage zones are likely to host deformation bands with a larger spread in orientation, compared to single fault damage zones. A similar scenario with a large spread in orientation of deformation bands have been observed by Johansen et al. (2005) and Fossen et al. (2005) in single tip fault interactions in the Moab Member. A comparable trend is recognized on a smaller scale in BC3, where a large spread in deformation band orientation is localized in zones surrounding intersecting slip surfaces (Fig. 5.20). These areas additionally display high 2D intensities, which coincide with the tendency of more widely oriented deformation bands in areas with the highest deformation band intensity, as observed by Johansen & Fossen (2008).

All five deformation band networks display a tendency for inverse correlation between the length of deformation bands (branch length) and deformation band intensity (2D intensity), where the highest 2D intensity correlates with short branch lengths, and vice versa. These findings support the theory that deformation bands grow, link, and form more densely spaced bands as strain increases (Fossen & Hesthammer, 1997), where increased linkage is represented by short deformation bands and more nodes.

In summary, these topological and geometrical findings indicate that an increase in finite strain can be associated with bifurcating and abutting deformation bands, and deformation band networks with shorter bands, which again corresponds to a dense deformation band network, with high connectivity.

6.2 Sequential growth of deformation band networks

Deformation band networks evolve and change characteristics and geometry as strain increases during fault displacement and damage zone widening (Shipton & Cowie, 2001). The findings of this study enhance our knowledge on the development and dynamics of deformation band networks, with emphasis on topological and geometrical characteristics. The results fit with the widely accepted model by Ayidin (1978) and Ayidin & Johnson (1978) where faults in porous sandstones nucleate from areas with densely packed deformation bands, and increased strain is associated with an increased number of deformation bands (e.g. Ayidin & Johnson, 1983; Mair et al., 2000; Shipton & Cowie, 2001; Hesthammer & Fossen, 2001; Fossen et al., 2007; Fossen et al., 2018).

This study has not quantified variations in topology at stages of fault growth or linkage. However, based on the identified correlations between strain, branch lengths, connectivity, and node distribution a conceptual model of how the topological characteristics of a deformation band network change over time is suggested. Prior to slip surface or fault nucleation, deformation bands occur more isolated and less connected. As the strain increases over time, new bands develop within and outside the existing damage zone, resulting in a wider damage zone (Fig. 6.4a,d) (Shipton & Cowie, 2003; Schueller et al., 2013). Simultaneously, the band length increases, and they start to overlap. Consequently, increased stress at deformation band tips cause linking and splaying bands to develop (Fig. 6.4b,e) (Schultz & Balasko, 2003). As a result, connectivity and Y-node proportions increase (Fig. 6.4g), while branch length decreases. With continued stress and higher strain, interconnected slip surfaces can form within areas of high deformation band intensity (typically clusters), and by doing so it produces damage further away from the main fault (Fig. 6.4c) (Shipton & Cowie, 2003).

Deformation band networks in intersection damage zones generally display a larger spread in orientation than deformation band networks in wall damage zones (Fig. 6.4D,E,F). However, their topological characteristics are more or less identical. In the lights of this, one could argue that deformation band networks in intersection damage zones grow in similar fashion to deformation band networks in wall damage zones, but stress rotation occurs due to fault interaction causing a rotation of the deformation bands (Fig. 6.4d, e, f) (e.g. Segall & Pollard, 1980; Childs et al., 1995; Johansen et al., 2005; Fossen et al., 2005; Fossen & Rotevatn, 2016). This fault interaction can also cause more bands to cross-cut pre-existing deformation bands (Fig. 6.4f) (Johansen et al., 2005).

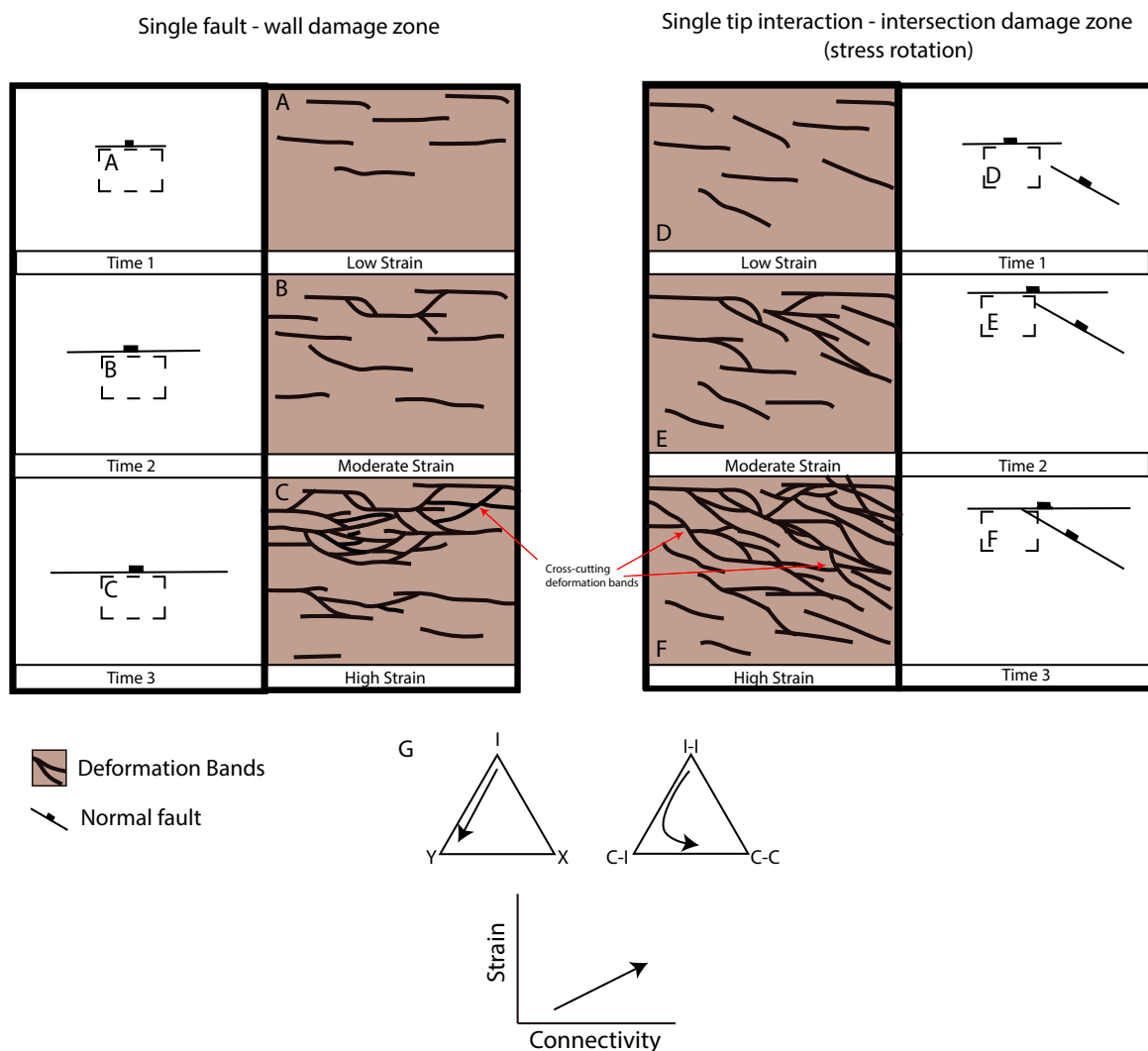


Figure 6.4: Illustration, showcasing the growth of a deformation band networks along a single fault (A-C) and single tip fault interaction (D-F). The figure illustrates how increased strain causes bands to overlap and link. A-C demonstrates the sequential growth of deformation band networks along a growing isolated fault. D-F) demonstrates the sequential growth of a deformation band network where two faults interact during simultaneous growth, which is known to produce more complex and extensive deformation compared to faults that interact separated in time (Fossen et al., 2005). G) The ternary diagram and arrows show how the topological character changes with increased strain. Notice how the topological characteristics are similar for the two different networks.

6.3 How does the topology of a deformation band network compare to other structural networks?

According to Manzocchi (2002), X-nodes rarely dominate any type of structural network (joints, fractures and faults), though some networks are more dominated by I-nodes than Y-nodes (e.g. Huseby et al., 1997; Manzocchi, 2002; Morley & Nixon, 2016). From observations in this thesis, combined with those from previous studies, it appears that deformation band networks display the highest Y-node proportion of any structural network. The high Y-node proportion might be explained by strain hardening mechanisms, which cause deformation bands to grow from single bands to swarms of bands (Ayidin, 1978). Dense deformation band networks form as a result of strain localisation during band formation and strain hardening on single bands (Kaproth et al., 2010). Deformation shifts between bands to accommodate bulk strain, which causes deformation to localise in undeformed host rock and expand the damage zone (Ayidin & Johnson, 1983; Mair et al., 2000; Shipton & Cowie, 2001). With increased strain this initiates linking of bands, which might explain why these networks have such a high Y-node proportion. This is different to other structural networks that typically form by strain softening mechanisms, such as faults that grow by crack propagation and linking in low-porosity and nonporous rocks (Fossen et al., 2005; Fossen et al., 2007).

The suggested topological evolution of deformation band networks (section 6.2), resembles the topological evolution of fault networks, described by Nixon et al. (2012), where fault networks are shown to evolve from individual faults that grow in length and displacement and start to link as strain increases. Additionally, they emphasise that the connectivity of fault networks increases with strain. Morley & Nixon (2016) further illustrates that as strain is increasing within a fault network the Y-node proportion increases, similar to the trend of a deformation band network.

6.4 Implications for fluid flow

The majority of deformation bands show a reduction in permeability. The largest permeability reduction is commonly observed within cataclastic deformation bands, which is the deformation band type studied in this thesis (Fossen et al., 2007). The permeability reduction for a single band commonly ranges between two to four orders of magnitude, while a cluster can show reductions up to five orders of magnitude (Antonellini & Aydin, 1994; Fossen & Bale, 2007). The impact of this reduction on fluid flow in subsurface reservoirs is, however, an

ongoing subject of study. The common consensus suggests that deformation bands have negligible effects on reservoir performance, except for dense networks that are well connected and with very low permeabilities (Fossen et al., 2005; Fossen & Bale, 2007; Rotevatn et al., 2009; Rotevatn et al., 2013; Ballas et al., 2015; Fossen et al., 2018). Nevertheless, the arrangement, orientation, and connectivity of deformation bands may prove an important controlling factor on flow pattern and reservoir sweep (Fossen & Bale, 2007; Rotevatn et al., 2013; Fossen et al., 2018). The results from this project provide valuable insights to the configuration and connectivity of deformation band networks, and how these parameters vary between and within damage zones.

Observations show deformation band networks with high connectivity reflected by abutting and splaying deformation bands. The results further demonstrate that increased strain causes more closely spaced deformation bands, higher connectivity and the development of clusters (Schueller et al., 2013). Fossen & Bale (2007) discuss the possibilities for fluids to divert around, between or through bands when the connectivity is low. It is thus reasonable to assume that deformation bands that exhibit high connectivity may act as baffles to fluid flow and channelize fluids along strike (Fossen et al., 2005). However, the actual impact on fluid flow depends strongly on the permeability contrast between the bands and the host rock (Rotevatn & Fossen, 2011; Rotevatn et al., 2013). A deformation band network featuring bands with a low permeability contrast relative to the host rock matrix will in most cases have negligible effects on fluid flow (Rotevatn & Fossen, 2011). Networks comprised of bands with a high permeability contrast can on the other hand exhibit significant control on fluid flow (Rotevatn et al., 2009; Rotevatn & Fossen, 2011). If we look at this from a reservoir production perspective, in a scenario where an injector and producer is placed on opposite sides of a fault, a wall damage zone comprised of high permeability deformation band network will favour fluid flow across the fault (Rotevatn et al., 2009). With lower deformation band permeability (more than three orders of magnitude) the wall damage zone will most likely start to channelize fluids along strike and increase the flow tortuosity, and as a result likely enhance the recovery (Fossen & Bale, 2007; Rotevatn et al., 2009; Rotevatn & Fossen, 2011). The same principles can be applied to deformation band networks in intersection damage zones. However, as the results have shown, these areas host deformation bands with larger orientation spread, complicating the prediction of how low permeability bands will affect the flow in these areas. Furthermore, it is important to note that this study is conducted on a planar 2D surface, and the overall effect on fluid flow depends on the three-dimensional continuity of deformation bands; apparent hard-

linked bands observed on a planar 2D surface does not necessarily exhibit hard-linked bands in a three-dimensional plane, and vice versa (Fossen & Hesthammer, 1997). Considering the high connectivity measured throughout the damage zones, it is though likely that deformation bands will splay, abut and cross-cut in 3D within areas that accumulate a high amount of strain, as is common for cluster zones (Fossen et al., 2018).

The clusters studied along the Big Hole Fault demonstrate varying thickness and intensity along strike, which coincide with the observations by Fossen & Bale (2007) and Torabi & Fossen (2009) that deformation bands and clusters exhibit rapid changes in thickness and permeability, both within a single band and within clusters. BC1 and BC2 illustrate such a variation, where both clusters display a considerably lower deformation band intensity in one end (ENE) (Fig. 6.3). These variations might have an implication on how fluids move within the damage zone as the weakest point in a deformation band network may act as conduit to fluid flow (Fossen et al., 2007). This observation suggests that flow along a single fault likely would align parallel to subparallel with the fault, as the arrangement of deformation bands cause the permeability to be higher along strike (Fossen & Bale, 2007). However, changes in cluster thickness and deformation band intensity along strike can influence the flow tortuosity, where fluids occasionally can migrate across a cluster and subsequently move along strike (Fossen & Bale, 2007; Schuller et al., 2013)

In summary, the results show that deformation band networks in both intersection damage zones and wall damage zones exhibit high connectivity. Their influence on fluid flow is thus dependent on the petrophysical properties in the bands (Fossen et al., 2005; Rotevatn et al., 2009). Wall damage zone deformation band networks with low permeability bands will potentially channelize fluids along strike. The intersection damage zone, on the other hand, is far more complex with deformation bands trending both parallel and oblique to the faults. These deformation band networks are therefore likely to act as baffles to fluid flow if the deformation band permeability contrast is high relative to that of the host rock. Predicting the fluid flow behavior is thus associated with high risk. One way of mitigating the risk would be to acquire core data and measure the permeability contrasts between the bands and the host rock, which can indicate to some degree whether the deformation band network pose a potential control on fluid flow. If so, fluid flow within fault intersecting damage zones is far less predictable due to the larger spread in orientation and resulting complexity. Consequently, care should be taken when placing a well in intersection damage zones, as also emphasized by Fossen et al. (2005).

6.5 The applicability of topology in well data analysis

There are instances where seismic resolution is too low for mapping of e.g. faults in a reservoir, as in basins where salt layers obscure the reflective response. Here, well data is essential for structural analysis. The question rises whether the application of topological analysis on deformation bands from resistivity image logs or core data can enhance our ability to predict: (1) the complexity of a deformation band network, and by that the networks ability to direct- or act as a baffle to fluid flow; (2) the proximity of a well to a potential fault; and (3) the type of damage zone the well is set in; All factors that are crucial in mapping fluid flow patterns. As a well represents an arbitrarily oriented scanline through the subsurface, the 1-dimensional frequency distribution of deformation bands can in theory help predict if a well is moving towards or away from a fault. The applicability of this method is discussed by Sanderson & Nixon (2015) in their studies of fractures. Predicting orientations of deformation bands within a well is though a method of high uncertainty since the sample sizes would be too small to provide the required information of orientation and spread. Nevertheless, classifying node-types is a readily applicable method in core-analysis. The usefulness of topology in cores and well data to predict proximity to faults and type of damage zone is though limited, as the topological characteristics for wall damage zones and intersection damage zones generally are similar. For example, a high proportion of I-nodes and X-nodes in a core suggests a high intensity and thus likely an area with high strain, which could further indicate that the well is in proximity to a fault or a slip surface. Studies, however, show that high intensity cluster zones can occur similarly at a large distance from the main fault (Schueller et al, 2013). To base predictions solely on topological studies in well data would thus be of significant uncertainty.

7 Conclusions and further work

7.1 Conclusions

This thesis characterizes deformation band networks in wall damage zones and intersection damage zones through a 2D-topological analysis of high-resolution outcrop photos. The studied rocks comprise outcrops of the Jurassic aeolian Navajo Sandstone and Moab Member in the Colorado Plateau, SE Utah. The main findings of the study are summarized here:

- Deformation band networks in both intersection damage zones and wall damage zones are dominated by bifurcating and abutting bands, which is reflected by a high Y-node proportion. Crossing bands (X-nodes) rarely occur within deformation band networks, but when they do, it is usually in areas of high strain. In these high strain areas, isolated bands (I-nodes) commonly occur as short, partly connected bands, which is due to soft linkage and splaying of bands with increased strain.
- Although topologically similar, the geometry and distribution of bands in intersection damage zones versus wall damage zones are different; intersection damage zones generally display deformation bands with a larger spread in orientation compared to wall damage zones. In addition, the clusters in wall damage zones display higher deformation band intensities compared to intersection damage zones.
- Increased strain causes deformation bands to overlap and link (soft linkage and hard linkage) and is associated with higher deformation band connectivity. This is reflected in shorter deformation bands and an increased number of Y-, X- and I –nodes in the high strain areas.
- The two parallel clusters BC1 and BC2 demonstrate through deformation band intensity patterns and deformation band frequency, that a damage zone grows through continuous formation of deformation bands both within the existing damage zone and outside the damage zone. This is evident by a comparative deformation band frequency trend between BC1 and BC2, where both clusters show the same frequency- and intensity distribution trend, suggesting that the formation of new clusters and maturation of pre-existing clusters occur contemporaneously. This observation is in accordance with the damage zone growth models presented by Shipton & Cowie (2001), Shipton & Cowie (2003) and Schuller et al. (2013).
- Deformation band networks with high connectivity, combined with high permeability contrasts, can influence the fluid flow. Predicting fluid flow patterns in subsurface

reservoirs along isolated normal faults is evidently simpler than predicting the fluid flow behaviour in intersection damage zones. This is due to the larger orientation spread of deformation bands in intersection damage zones. Deformation band networks along an isolated normal faults typically form dense elongated clusters (sub)parallel to the fault, channelizing fluids along strike. Intersection damage zones exhibit more complex orientations, and predictions for fluid flow within these areas are thus more uncertain. Depending on the permeability contrasts between bands and the host rock the intersection damage zones may act as barrier or baffle to fluid flow.

- Quantifying node types in well data is applicable, but the value of this information is limited. This study demonstrates that the topological characteristics of intersection damage zones and wall damage zones are too similar to allow for any prediction of damage zones type or the wells proximity to a fault.

7.2 Further work

This study has focused on topological analysis of deformation band network properties in wall damage zones and intersections damage zones. It would be relevant to apply the same analytic approach to deformation band networks in other types of damage zones, as this would add valuable information to the presented network growth model (Fig. 6.4). Moreover, this study quantifies networks solely in aeolian rocks. It would be interesting to additionally investigate deformation band networks in carbonates and volcanoclastics to compare the network characteristics and look for potential trends that apply to all networks. Another relevant approach would be to study deformation band network properties at a range of different scales to search for self-similarity patterns, meaning that parts of a deformation band network may show the same statistical properties at different scales. Moreover, the findings in this study could be implemented on a larger scale for relevant fault intersection and reservoirs.

Finally, a highly relevant and applicable addition would be to integrate the recorded deformation band intensities, connectivity, and geometries into fluid flow simulations, as this would lead to an enhanced understanding of the networks controlling factor on fluid flow.

8 References

- Adler, P. M., & Thovert, J.-F. (1999). Fractures and fracture networks (Vol. 15): *Springer Science & Business Media*.
- Antonellini, M., & Aydin, A. (1994). Effect of faulting on fluid flow in porous sandstones: petrophysical properties. *AAPG bulletin*, 78(3), 355-377.
- Antonellini, M. A., Aydin, A., & Pollard, D. D. (1994). Microstructure of deformation bands in porous sandstones at Arches National Park, Utah. *Journal of structural geology*, 16(7), 941-959.
- Antonellini, M. A., & Pollard, D. D. (1995). Distinct element modeling of deformation bands in sandstone. *Journal of structural geology*, 17(8), 1165-1182.
- Armstrong, R. L. (1968). Sevier orogenic belt in Nevada and Utah. *Geological Society of America Bulletin*, 79(4), 429-458.
- Aydin, A. (1978). Small faults formed as deformation bands in sandstone. In *Rock Friction and Earthquake Prediction* (pp. 913-930): Springer.
- Aydin, A., Borja, R. I., & Eichhubl, P. (2006). Geological and mathematical framework for failure modes in granular rock. *Journal of structural geology*, 28(1), 83-98.
- Aydin, A., & Johnson, A. M. (1978). Development of faults as zones of deformation bands and as slip surfaces in sandstone. *Pure and applied Geophysics*, 116(4-5), 931-942.
- Aydin, A., & Johnson, A. M. (1983). Analysis of faulting in porous sandstones. *Journal of structural geology*, 5(1), 19-31.
- Baker, A. A. (1935). Geologic structure of southeastern Utah. *AAPG bulletin*, 19(10), 1472-1507.
- Ballas, G., Fossen, H., & Soliva, R. (2015). Factors controlling permeability of cataclastic deformation bands and faults in porous sandstone reservoirs. *Journal of structural geology*, 76, 1-21.
- Barbeau, D. (2003). A flexural model for the Paradox Basin: implications for the tectonics of the Ancestral Rocky Mountains. *Basin Research*, 15(1), 97-115.
- Beach, A., Welbon, A. I., Brockbank, P. J., & McCallum, J. E. (1999). Reservoir damage around faults; outcrop examples from the Suez Rift. *Petroleum Geoscience*, 5(2), 109-116.
- Berg, S. S., & Skar, T. (2005). Controls on damage zone asymmetry of a normal fault zone: outcrop analyses of a segment of the Moab fault, SE Utah. *Journal of structural geology*, 27(10), 1803-1822.
- Bésuelle, P. (2001). Evolution of strain localisation with stress in a sandstone: brittle and semi-brittle regimes. *Physics and Chemistry of the Earth, Part A: Solid Earth and Geodesy*, 26(1-2), 101-106.
- Biddle, K. T., & Christie-Blick, N. (1985). Glossary—strike-slip deformation, basin formation, and sedimentation.
- Blakey, R. C. (1989). Triassic and Jurassic geology of the southern Colorado Plateau. *Geologic evolution of Arizona: Arizona Geological Society Digest*, 17, 369-396.
- Boccaletti, S., Latora, V., Moreno, Y., Chavez, M., & Hwang, D.-U. (2006). Complex networks: Structure and dynamics. *Physics reports*, 424(4-5), 175-308.
- Budnik, R. T. (1986). Left-lateral intraplate deformation along the Ancestral Rocky Mountains: implications for late Paleozoic plate motions. *Tectonophysics*, 132(1-3), 195-214.
- Baars, D., & Stevenson, G. (1981). Tectonic evolution of the Paradox basin, Utah and Colorado. In: *Geology of the Paradox Basin* (Ed. by D.L. Wiegand), pp. 23-31. Association of Geologists, Rocky Mount.

- Caine, J. S., Evans, J. P., & Forster, C. B. (1996). Fault zone architecture and permeability structure. *Geology*, *24*(11), 1025-1028.
- Case, J. (1991). *Geologic Map of the Northwestern Part of the Uncompahgre Uplift, Grand County, Utah, and Mesa County, Colorado, with Emphasis on Proterozoic rocks*: US Geological Survey.
- Cavailles, T., & Rotevatn, A. (2018). Deformation bands in volcanoclastic rocks—Insights from the Shihtiping tuffs, Coastal Range of Taiwan. *Journal of structural geology*, *113*, 155-175.
- Cawood, A. J., Bond, C. E., Howell, J. A., Butler, R. W., & Totake, Y. (2017). LiDAR, UAV or compass-clinometer? Accuracy, coverage and the effects on structural models. *Journal of Structural Geology*, *98*, 67-82.
- Chester, F., & Logan, J. M. (1986). Implications for mechanical properties of brittle faults from observations of the Punchbowl fault zone, California. *Pure and applied Geophysics*, *124*(1-2), 79-106.
- Cheung, C. S., Baud, P., & Wong, T. f. (2012). Effect of grain size distribution on the development of compaction localization in porous sandstone. *Geophysical Research Letters*, *39*(21).
- Childs, C., Manzocchi, T., Walsh, J. J., Bonson, C. G., Nicol, A., & Schöpfer, M. P. (2009). A geometric model of fault zone and fault rock thickness variations. *Journal of structural geology*, *31*(2), 117-127.
- Childs, C., Watterson, J., & Walsh, J. (1995). Fault overlap zones within developing normal fault systems. *Journal of the Geological Society*, *152*(3), 535-549.
- Choi, J.-H., Edwards, P., Ko, K., & Kim, Y.-S. (2016). Definition and classification of fault damage zones: A review and a new methodological approach. *Earth-Science Reviews*, *152*, 70-87.
- Cowie, P. A., & Scholz, C. H. (1992). Displacement-length scaling relationship for faults: data synthesis and discussion. *Journal of structural geology*, *14*(10), 1149-1156.
- Crabaugh, M., & Kocurek, G. (1993). Entrada Sandstone: an example of a wet aeolian system. *Geological Society, London, Special Publications*, *72*(1), 103-126.
- Cruikshank, K. M., & Aydin, A. (1995). Unweaving the joints in Entrada Sandstone, Arches National Park, Utah, USA. *Journal of structural geology*, *17*(3), 409-421.
- Dickinson, W. R. (2004). Evolution of the North American cordillera. *Annu. Rev. Earth Planet. Sci.*, *32*, 13-45.
- Doelling, H. H., Ross, M. L., & Mulvey, W. E. (2002). *Geologic map of the Moab 7.5' quadrangle, Grand County, Utah*: Utah Geological Survey, Utah Department of Natural Resources.
- Du Bernard, X., Eichhubl, P., & Aydin, A. (2002). Dilation bands: A new form of localized failure in granular media. *Geophysical Research Letters*, *29*(24), 29-21-29-24.
- Duffy, O. B., Bell, R. E., Jackson, C. A.-L., Gawthorpe, R. L., & Whipp, P. S. (2015). Fault growth and interactions in a multiphase rift fault network: Horda Platform, Norwegian North Sea. *Journal of structural geology*, *80*, 99-119.
- Dumitru, T. A., Gans, P. B., Foster, D. A., & Miller, E. L. (1991). Refrigeration of the western Cordilleran lithosphere during Laramide shallow-angle subduction. *Geology*, *19*(11), 1145-1148.
- Eaton, G. P. (1982). The Basin and Range province: Origin and tectonic significance. *Annual Review of Earth and Planetary Sciences*, *10*(1), 409-440.
- Elston, D. P., Shoemaker, E. M., & Landis, E. (1962). Uncompahgre front and salt anticline region of Paradox Basin, Colorado and Utah. *AAPG bulletin*, *46*(10), 1857-1878.
- Evans, J. P. (1990). Thickness-displacement relationships for fault zones. *Journal of structural geology*, *12*(8), 1061-1065.
- Evans, J. P., & Bradbury, K. K. (2004). Faulting and Fracturing of Nonwelded Bishop Tuff, Eastern California Deformation Mechanisms in Very Porous Materials in the Vadose Zone. *Vadose Zone Journal*, *3*(2), 602-623.

- Faulkner, D., Mitchell, T., Jensen, E., & Cembrano, J. (2011). Scaling of fault damage zones with displacement and the implications for fault growth processes. *Journal of Geophysical Research: Solid Earth*, 116(B5).
- Flowers, R. M. (2010). The enigmatic rise of the Colorado Plateau. *Geology*, 38(7), 671-672.
- Fossen, H., & Bale, A. (2007). Deformation bands and their influence on fluid flow. *AAPG bulletin*, 91(12), 1685-1700.
- Fossen, H., & Hesthammer, J. (1997). Geometric analysis and scaling relations of deformation bands in porous sandstone. *Journal of structural geology*, 19(12), 1479-1493.
- Fossen, H., & Hesthammer, J. (2000). Possible absence of small faults in the Gullfaks Field, northern North Sea: implications for downscaling of faults in some porous sandstones. *Journal of structural geology*, 22(7), 851-863.
- Fossen, H., Hesthammer, J., Johansen, T. E. S., & Sygnabere, T. O. (2003). Structural geology of the Huldra field, northern North Sea—A major tilted fault block at the eastern edge of the Horda platform. *Marine and Petroleum Geology*, 20(10), 1105-1118.
- Fossen, H., Johansen, T. E. S., Hesthammer, J., & Rotevatn, A. (2005). Fault interaction in porous sandstone and implications for reservoir management; examples from southern Utah. *AAPG bulletin*, 89(12), 1593-1606.
- Fossen, H., & Rotevatn, A. (2016). Fault linkage and relay structures in extensional settings—A review. *Earth-Science Reviews*, 154, 14-28.
- Fossen, H., Schultz, R. A., Shipton, Z. K., & Mair, K. (2007). Deformation bands in sandstone: a review. *Journal of the Geological Society*, 164(4), 755-769.
- Fossen, H., Schultz, R. A., & Torabi, A. (2011). Conditions and implications for compaction band formation in the Navajo Sandstone, Utah. *Journal of structural geology*, 33(10), 1477-1490.
- Fossen, H., Soliva, R., Ballas, G., Trzaskos, B., Cavalcante, C., & Schultz, R. A. (2018). A review of deformation bands in reservoir sandstones: geometries, mechanisms and distribution. *Geological Society, London, Special Publications*, 459(1), 9-33.
- Freeman, W. E., & Visher, G. S. (1975). Stratigraphic analysis of the Navajo Sandstone. *Journal of Sedimentary Research*, 45(3), 651-668.
- Gudmundsson, A., Simmenes, T. H., Larsen, B., & Philipp, S. L. (2010). Effects of internal structure and local stresses on fracture propagation, deflection, and arrest in fault zones. *Journal of structural geology*, 32(11), 1643-1655.
- Hanke, J. R., Fischer, M. P., & Pollyea, R. M. (2018). Directional semivariogram analysis to identify and rank controls on the spatial variability of fracture networks. *Journal of structural geology*, 108, 34-51.
- Hintze, L., & Kowallis, B. (2009). *Geological history of Utah*. Brigham Young University Geology Studies.
- Hirschmuller, H. (2007). Stereo processing by semiglobal matching and mutual information. *IEEE transactions on pattern analysis and machine intelligence*, 30(2), 328-341.
- Hite, R. J. (1968). Salt deposits of the Paradox Basin, southeast Utah and southwest Colorado. *Saline deposits: Geol. Soc. America Spec. Paper*, 88, 319-330.
- Horsfield, W. (1980). Contemporaneous movement along crossing conjugate normal faults. *Journal of structural geology*, 2(3), 305-310.
- Huseby, O., Thovert, J., & Adler, P. (1997). Geometry and topology of fracture systems. *Journal of Physics A: Mathematical and General*, 30(5), 1415.
- Johansen, T. E. S., & Fossen, H. (2008). Internal geometry of fault damage zones in interbedded siliciclastic sediments. *Geological Society, London, Special Publications*, 299(1), 35-56.
- Johansen, T. E. S., Fossen, H., & Kluge, R. (2005). The impact of syn-faulting porosity reduction on damage zone architecture in porous sandstone: an outcrop example from the Moab Fault, Utah. *Journal of structural geology*, 27(8), 1469-1485.

- Jourde, H., Flodin, E. A., Aydin, A., Durlofsky, L. J., & Wen, X.-H. (2002). Computing permeability of fault zones in eolian sandstone from outcrop measurements. *AAPG bulletin*, 86(7), 1187-1200.
- Kaproth, B. M., Cashman, S. M., & Marone, C. (2010). Deformation band formation and strength evolution in unlithified sand: the role of grain breakage. *Journal of Geophysical Research: Solid Earth*, 115(B12).
- Kim, Y.-S., Peacock, D. C., & Sanderson, D. J. (2004). Fault damage zones. *Journal of structural geology*, 26(3), 503-517.
- Kim, Y. S., & Sanderson, D. J. (2006). Structural similarity and variety at the tips in a wide range of strike-slip faults: a review. *Terra Nova*, 18(5), 330-344.
- Kluth, C. F., 1986, Plate tectonics of the Ancestral Rocky Mountains, in Peterson, J. A., ed., Paleotectonics and sedimentation in the Rocky Mountain region, United States: *American Association of Petroleum Geologists Memoir 41*, p. 353-369
- Knipe, R. (1992). Faulting processes and fault seal. In *Structural and tectonic modelling and its application to petroleum geology* (pp. 325-342): Elsevier.
- Knipe, R., Fisher, Q., Jones, G., Clennell, M., Farmer, A., Harrison, A., . . . White, E. (1997). Fault seal analysis: successful methodologies, application and future directions. In *Norwegian Petroleum Society Special Publications* (Vol. 7, pp. 15-38): Elsevier.
- Krantz, R. W. (1988). Multiple fault sets and three-dimensional strain: theory and application. *Journal of structural geology*, 10(3), 225-237.
- Latora, V., & Marchiori, M. (2002). Is the Boston subway a small-world network? *Physica A: Statistical Mechanics and its Applications*, 314(1-4), 109-113.
- Maerten, L. (2000). Variation in slip on intersecting normal faults: Implications for paleostress inversion. *Journal of Geophysical Research: Solid Earth*, 105(B11), 25553-25565.
- Mair, K., Main, I., & Elphick, S. (2000). Sequential growth of deformation bands in the laboratory. *Journal of structural geology*, 22(1), 25-42.
- Mandl, G., De Jong, L., & Maltha, A. (1977). Shear zones in granular material. *Rock mechanics*, 9(2-3), 95-144.
- Manzocchi, T. (2002). The connectivity of two-dimensional networks of spatially correlated fractures. *Water Resources Research*, 38(9), 1-1-1-20.
- Mauldon, M., Dunne, W., & Rohrbaugh Jr, M. (2001). Circular scanlines and circular windows: new tools for characterizing the geometry of fracture traces. *Journal of Structural Geology*, 23(2-3), 247-258.
- McGrath, A. G., & Davison, I. (1995). Damage zone geometry around fault tips. *Journal of structural geology*, 17(7), 1011-1024.
- Mollema, P. N., & Antonellini, M. (1999). Development of strike-slip faults in the dolomites of the Sella Group, Northern Italy. *Journal of structural geology*, 21(3), 273-292.
- Morgan, P., & Swanberg, C. (1985). On the Cenozoic uplift and tectonic stability of the Colorado Plateau. *Journal of Geodynamics*, 3(1-2), 39-63.
- Morley, C., & Nixon, C. (2016). Topological characteristics of simple and complex normal fault networks. *Journal of structural geology*, 84, 68-84.
- Nixon, C. W., Sanderson, D. J., & Bull, J. M. (2012). Analysis of a strike-slip fault network using high resolution multibeam bathymetry, offshore NW Devon UK. *Tectonophysics*, 541, 69-80.
- Nuccio, V. F., & Condon, S. M. (1996). Burial and thermal history of the Paradox Basin, Utah and Colorado, and petroleum potential of the Middle Pennsylvanian Paradox Basin. *US Geological Survey Bulletin*, 2000-0, 41pp.
- Nyberg, B., Nixon, C. W., & Sanderson, D. J. (2018). NetworkGT: A GIS tool for geometric and topological analysis of two-dimensional fracture networks. *Geosphere*, 14(4), 1618-1634.

- Ortega, O., & Marrett, R. (2000). Prediction of macrofracture properties using microfracture information, Mesaverde Group sandstones, San Juan basin, New Mexico. *Journal of Structural Geology*, 22(5), 571-588.
- Parnell, J., Watt, G. R., Middleton, D., Kelly, J., & Baron, M. (2004). Deformation band control on hydrocarbon migration. *Journal of Sedimentary Research*, 74(4), 552-560.
- Peacock, D. (2002). Propagation, interaction and linkage in normal fault systems. *Earth-Science Reviews*, 58(1-2), 121-142.
- Peacock, D., Dimmen, V., Rotevatn, A., & Sanderson, D. (2017a). A broader classification of damage zones. *Journal of structural geology*, 102, 179-192.
- Peacock, D., Knipe, R., & Sanderson, D. (2000). Glossary of normal faults. *Journal of structural geology*, 22(3), 291-305.
- Peacock, D., Nixon, C., Rotevatn, A., Sanderson, D., & Zuluaga, L. (2017b). Interacting faults. *Journal of structural geology*, 97, 1-22.
- Peacock, D., & Sanderson, D. (1991). Displacements, segment linkage and relay ramps in normal fault zones. *Journal of structural geology*, 13(6), 721-733.
- Pollard, D. D., & Aydin, A. (1984). Propagation and linkage of oceanic ridge segments. *Journal of Geophysical Research: Solid Earth*, 89(B12), 10017-10028.
- Randles, T., Clarke, S., & Richards, P. (2012). *Development of Crestal Collapse Structures above Dissolving Salt Anticlines: Application to Seismic Interpretation within Salt-Controlled Basins*. Paper presented at the AAPG 2012 Conference.
- Rath, A., Exner, U., Tschegg, C., Grasemann, B., Laner, R., & Draganits, E. (2011). Diagenetic control of deformation mechanisms in deformation bands in a carbonate grainstone. *AAPG bulletin*, 95(8), 1369-1381.
- Rawnsley, K., Rives, T., Petti, J.-P., Hencher, S., & Lumsden, A. (1992). Joint development in perturbed stress fields near faults. *Journal of structural geology*, 14(8-9), 939-951.
- Rotevatn, A., & Fossen, H. (2011). Simulating the effect of subseismic fault tails and process zones in a siliciclastic reservoir analogue: Implications for aquifer support and trap definition. *Marine and Petroleum Geology*, 28(9), 1648-1662.
- Rotevatn, A., Fossen, H., Hesthammer, J., Aas, T. E., & Howell, J. A. (2007). Are relay ramps conduits for fluid flow? Structural analysis of a relay ramp in Arches National Park, Utah. *Geological Society, London, Special Publications*, 270(1), 55-71.
- Rotevatn, A., Sandve, T., Keilegavlen, E., Kolyukhin, D., & Fossen, H. (2013). Deformation bands and their impact on fluid flow in sandstone reservoirs: the role of natural thickness variations. *Geofluids*, 13(3), 359-371.
- Rotevatn, A., Thorsheim, E., Bastesen, E., Fossmark, H. S., Torabi, A., & Sælen, G. (2016). Sequential growth of deformation bands in carbonate grainstones in the hangingwall of an active growth fault: implications for deformation mechanisms in different tectonic regimes. *Journal of structural geology*, 90, 27-47.
- Rotevatn, A., Tveranger, J., Howell, J., & Fossen, H. (2009). Dynamic investigation of the effect of a relay ramp on simulated fluid flow: geocellular modelling of the Delicate Arch Ramp, Utah. *Petroleum Geoscience*, 15(1), 45-58.
- Sanderson, D. J., & Nixon, C. W. (2015). The use of topology in fracture network characterization. *Journal of structural geology*, 72, 55-66.
- Schueller, S., Braathen, A., Fossen, H., & Tveranger, J. (2013). Spatial distribution of deformation bands in damage zones of extensional faults in porous sandstones: Statistical analysis of field data. *Journal of structural geology*, 52, 148-162.
- Schultz, R. A., & Balasko, C. M. (2003). Growth of deformation bands into echelon and ladder geometries. *Geophysical Research Letters*, 30(20).
- Segall, P., & Pollard, D. (1980). Mechanics of discontinuous faults. *Journal of Geophysical Research: Solid Earth*, 85(B8), 4337-4350.

- Shipton, Z., & Cowie, P. (2001). Damage zone and slip-surface evolution over μm to km scales in high-porosity Navajo sandstone, Utah. *Journal of structural geology*, 23(12), 1825-1844.
- Shipton, Z. K. (1999). *Fault displacement profiles and off-fault deformation: Interpreting the record of fault growth at the Chimney Rock fault array, Utah, USA*. University of Edinburgh, Edinburgh, UK.
- Shipton, Z. K., & Cowie, P. A. (2003). A conceptual model for the origin of fault damage zone structures in high-porosity sandstone. *Journal of structural geology*, 25(3), 333-344.
- Shipton, Z. K., Evans, J. P., Robeson, K. R., Forster, C. B., & Snelgrove, S. (2002). Structural heterogeneity and permeability in faulted eolian sandstone: Implications for subsurface modeling of faults. *AAPG bulletin*, 86(5), 863-883.
- Sibson, R. (1977). Fault rocks and fault mechanisms. *Journal of the Geological Society*, 133(3), 191-213.
- Soliva, R., Ballas, G., Fossen, H., & Philit, S. (2016). Tectonic regime controls clustering of deformation bands in porous sandstone. *Geology*, 44(6), 423-426.
- Soliva, R., Schultz, R. A., Ballas, G., Taboada, A., Wibberley, C., Sallet, E., & Benedicto, A. (2013). A model of strain localization in porous sandstone as a function of tectonic setting, burial and material properties; new insight from Provence (southern France). *Journal of structural geology*, 49, 50-63.
- Spencer, J. E. (1996). Uplift of the Colorado Plateau due to lithosphere attenuation during Laramide low-angle subduction. *Journal of Geophysical Research: Solid Earth*, 101(B6), 13595-13609.
- Sternlof, K. R., Karimi-Fard, M., Pollard, D., & Durlinsky, L. (2006). Flow and transport effects of compaction bands in sandstone at scales relevant to aquifer and reservoir management. *Water Resources Research*, 42(7).
- Stevenson, G., & Baars, D. (1986). The Paradox: A Pull-Apart Basin of Pennsylvanian Age. In: J.E. Peterson (Editor), *Paleotectonics and Sedimentation in the Rocky Mountain Region, United States. Am. Assoc. Pet. Geol., Mem., 41: 513-539*.
- Sundal, A., Miri, R., Hellevang, H., Tveranger, J., Midtkandal, I., Zuchuat, V., . . . Braathen, A. (2017). Movement of CO₂ charged fluids in low permeability rocks during deformation: migration patterns in the Carmel Formation, Utah. *Energy Procedia*, 114, 4537-4544.
- Tondi, E., Antonellini, M., Aydin, A., Marchegiani, L., & Cello, G. (2006). The role of deformation bands, stylolites and sheared stylolites in fault development in carbonate grainstones of Majella Mountain, Italy. *Journal of structural geology*, 28(3), 376-391.
- Torabi, A., & Berg, S. S. (2011). Scaling of fault attributes: A review. *Marine and Petroleum Geology*, 28(8), 1444-1460.
- Torabi, A., & Fossen, H. (2009). Spatial variation of microstructure and petrophysical properties along deformation bands in reservoir sandstones. *AAPG bulletin*, 93(7), 919-938.
- Trudgill, B. (2011). Evolution of salt structures in the northern Paradox Basin: Controls on evaporite deposition, salt wall growth and supra-salt stratigraphic architecture. *Basin Research*, 23(2), 208-238.
- Ujiie, K., Maltman, A. J., & Sánchez-Gómez, M. (2004). Origin of deformation bands in argillaceous sediments at the toe of the Nankai accretionary prism, southwest Japan. *Journal of structural geology*, 26(2), 221-231.
- Vermilye, J. M., & Scholz, C. H. (1998). The process zone: A microstructural view of fault growth. *Journal of Geophysical Research: Solid Earth*, 103(B6), 12223-12237.
- Walsh, J., Bailey, W., Childs, C., Nicol, A., & Bonson, C. (2003). Formation of segmented normal faults: a 3-D perspective. *Journal of structural geology*, 25(8), 1251-1262.
- Wilson, J. E., Goodwin, L. B., & Lewis, C. J. (2003). Deformation bands in nonwelded ignimbrites: Petrophysical controls on fault-zone deformation and evidence of preferential fluid flow. *Geology*, 31(10), 837-840.

- Zuluaga, L. F., Fossen, H., & Rotevatn, A. (2014). Progressive evolution of deformation band populations during Laramide fault-propagation folding: Navajo Sandstone, San Rafael monocline, Utah, USA. *Journal of structural geology*, 68, 66-81.
- Aarland, R., & Skjerven, J. (1998). Fault and fracture characteristics of a major fault zone in the northern North Sea: analysis of 3D seismic and oriented cores in the Brage Field (Block 31/4). *Geological Society, London, Special Publications*, 127(1), 209-229.

Appendix I: Abbreviations and calculations in NetworkGT

Appendix I

Appendix I: A full summary of abbreviations, parameters and formulas used in topology parameters and block analysis calculations in NetworkGT. Modified from Nyberg et al. (2018).

Parameter	Description	Calculation
Area (A)	Sample area	A
Number of nodes (N_n)	Number of I, Y and X nodes	$N_I + N_Y + N_X$
Number of connections (N_c)	Number of X and Y nodes	$N_Y + N_X$
Number of edge nodes	N_E	N_E
Number of branches (N_B) Calculated from nodes	Total number of branches, calculated from nodes	$\frac{N_I + 3N_Y + 4N_X}{2}$
Number of lines (N_L)	Total number of lines, calculated from nodes	$\frac{N_I + 2N_Y}{2}$
Connection/line	Connections per line	$\frac{2(N_Y + N_X)}{N_L}$
Connection/branch (C_B)	Connections per branch	$\frac{3N_Y + 4N_X}{N_B}$
Total trace length $\sum L$	Sum of branch lengths	$\sum L$
Average line length (B_L)	Average line length	$\frac{\sum L}{N_L}$
Average branch length (B_c)	Average branch length	$\frac{\sum L}{N_B}$
Connecting node frequency	Frequency of connecting nodes within the sample area	$\frac{N_C}{A}$
Branch frequency	Frequency of branches within the sample area	$\frac{N_B}{A}$
Line frequency	Frequency of lines within sample area	$\frac{N_L}{A}$
1D intensity (P_{10})	Intensity of deformation bands within a circular sample area	$\frac{N_E}{2\pi r} \cdot \frac{\pi}{2}$
2D intensity (P_{21})	Intensity of deformation bands within a sample area	$\frac{\sum L}{A}$
Dimensionless intensity (B_{21})	Product of average branch length and intensity	$P_{21} \cdot L_B$
Number of branches (calculated from branches)	Number of C-C, C-I and I-I	$N_{CC} + N_{CI} + N_{II}$
Block analysis		
Number of clusters (K_{ij})	Number of clusters in sample area	K_{ij}
Number of intersecting clusters (K_i)	Number of clusters that intersects the bounding polygon	K_i
Number of branches (block calculation) (B)	Number of branches, calculated from nodes and E nodes	$\frac{N_I + N_E + 3N_Y + 4N_X}{2}$
Number of nodes (block calculation) (block calculation) (N)	Number of I, Y, X and E nodes	$N_I + N_E + N_Y + N_X$
Number of whole blocks	Whole blocks within the sample area	$B - N + K_{ij}$
Number of half blocks (H_B)	Potential blocks that are only partially within the sample area	$\frac{N_E - K_i + 1}{2}$
Number of theoretical blocks (T_b)	Total number of whole and half blocks	$W_b + H_b$
Theoretical block size	Average area of theoretical block	$\frac{T_b}{A}$

Appendix II: Geometrical and topological data

Appendix II

Geometrical and topological data from Klondike West, derived with NetworkGT. For circle sample position, see Fig. 5.3.

Circle Sample ID	Area (m2) E	I	X	Y	No. Nodes	No. Branches	No. Lines	No. Connections	Connect/Line	Average Line Length(m)	Average Branch Length (m)	Connect/Branch	Branch Freq	Line Freq	NcFreq	2D Intensity m-1	Dimensionless Intensity	C - C	C - I	I-I	Total Trace Length (m)	
1B	0,78527	11	10	2	15	27	31,5	12,5	17	2,72	0,445	0,177	1,68254	40,114	15,918	21,649	7,080	1,24961	17,5	13,5	0,5	5,560
2B	0,78527	30	7	1	71	79	112	39	72	3,69231	0,346	0,121	1,9375	142,626	49,665	91,688	17,205	2,07546	93	18,5	0,5	13,511
3B	0,78527	13	4	3	27	34	48,5	15,5	30	3,87097	0,517	0,165	1,91753	61,762	19,738	38,203	10,213	1,68898	38	10,5	0	8,020
4B	0,78527	18	10	2	54	66	90	32	56	3,5	0,360	0,128	1,88889	114,610	40,750	71,313	14,677	1,87956	73	16	1	11,525
5B	0,78527	9	1	0	16	17	24,5	8,5	16	3,76471	0,564	0,196	1,95918	31,200	10,824	20,375	6,104	1,19422	19	5,5	0	4,793
6B	0,78527	14	5	0	27	32	43	16	27	3,375	0,454	0,169	1,88372	54,758	20,375	34,383	9,250	1,5627	33	9,5	0,5	7,264
7B	0,78527	3	2	0	21	23	32,5	11,5	21	3,65217	0,220	0,078	1,93846	41,387	14,645	26,742	3,221	0,25066	29	3,5	0	2,529
8B	0,78527	14	3	0	25	28	39	14	25	3,57143	0,520	0,187	1,92308	49,665	17,828	31,836	9,268	1,72964	30	9	0	7,278
9B	0,78527	5	0	0	11	11	16,5	5,5	11	4	0,658	0,219	2	21,012	7,004	14,008	4,612	1,01226	14	2,5	0	3,622
10B	0,78527	10	0	0	20	20	30	10	20	4	0,440	0,147	2	38,203	12,734	25,469	5,602	0,82159	25	5	0	4,399
11B	0,78527	15	5	1	32	38	52,5	18,5	33	3,56757	0,470	0,166	1,90476	66,856	23,559	42,024	11,068	1,83235	41	11	0,5	8,691
12B	0,78527	8	4	1	38	43	61	21	39	3,71429	0,268	0,092	1,93443	77,680	26,742	49,665	7,172	0,66214	53	8	0	5,632
13B	0,78527	10	1	0	17	18	26	9	17	3,77778	0,674	0,233	1,96154	33,110	11,461	21,649	7,726	1,80289	20	6	0	6,067
SUMMARIZED	10,209	160	52	10	374	436	607	213	384	47,206	5,9371	2,0769	24,9316	772,984	271,245	489,004	113,200	17,762	486	118,5	3	88,892
AVERAGE	0,785	#####	4	0,769	28,769	33,538	46,692	16,385	29,538	3,631	0,4567	0,1598	1,9178	59,4603	20,8650	37,616	8,708	1,366312308	37,3	9,1154	0,2308	6,838

Node proportion

Circle Sample ID	I	X	Y
1B	0,37037	0,074	0,56
2B	0,08861	0,013	0,9
3B	0,11765	0,088	0,79
4B	0,15152	0,03	0,82
5B	0,05882	0	0,94
6B	0,15625	0	0,84
7B	0,08696	0	0,91
8B	0,10714	0	0,89
9B	0	0	1
10B	0	0	1
11B	0,13158	0,026	0,84
12B	0,09302	0,023	0,88
13B	0,05556	0	0,94

Branch proportion

Circle Sample ID	C - C	C - I	I - I
1B	0,55555556	0,42857143	0,01587302
2B	0,83035714	0,16517857	0,00446429
3B	0,78350515	0,21649485	0
4B	0,81111111	0,17777778	0,01111111
5B	0,7755102	0,2244898	0
6B	0,76744186	0,22093023	0,01162791
7B	0,89230769	0,10769231	0
8B	0,76923077	0,23076923	0
9B	0,84848485	0,15151515	0
10B	0,83333333	0,16666667	0
11B	0,78095238	0,20952381	0,00952381
12B	0,86885246	0,13114754	0
13B	0,76923077	0,23076923	0

Node and branch proportions from Klondike East

Klondike East							
Node proportions				Branch proportions			
CS	I	X	Y	CS	C-C	C-I	I-I
1A	0,05	0,40	0,55	1A	0,82	0,18	0,00
2A	0,03	0,14	0,84	2A	0,89	0,11	0,00
3A	0,04	0,00	0,96	3A	0,81	0,19	0,00
4A	0,04	0,04	0,92	4A	0,78	0,22	0,00
5A	0,10	0,04	0,86	5A	0,79	0,21	0,00
6A	0,00	0,02	0,98	6A	0,90	0,10	0,00
7A	0,07	0,13	0,80	7A	0,80	0,20	0,00
8A	0,11	0,18	0,71	8A	0,77	0,23	0,00
9A	0,00	0,21	0,79	9A	0,87	0,13	0,00
10A	0,00	0,00	1,00	10A	0,87	0,13	0,00
11A	0,03	0,00	0,97	11A	0,80	0,20	0,00
12A	0,14	0,05	0,82	12A	0,79	0,20	0,02
13A	0,00	0,00	1,00	13A	0,89	0,11	0,00
14A	0,08	0,03	0,90	14A	0,79	0,21	0,00
15A	0,12	0,00	0,88	15A	0,81	0,19	0,00
16A	0,11	0,00	0,89	16A	0,82	0,18	0,00
17A	0,05	0,01	0,94	17A	0,89	0,11	0,00
18A	0,08	0,08	0,83	18A	0,88	0,11	0,01
19A	0,05	0,00	0,95	19A	0,89	0,10	0,01
20A	0,09	0,03	0,87	20A	0,82	0,17	0,00
21A	0,11	0,03	0,85	21A	0,81	0,19	0,00
22A	0,07	0,10	0,83	22A	0,90	0,10	0,00
23A	0,07	0,00	0,93	23A	0,85	0,15	0,00
24A	0,00	0,02	0,98	24A	0,90	0,10	0,00
25A	0,10	0,00	0,90	25A	0,84	0,16	0,00
26A	0,01	0,01	0,98	26A	0,94	0,05	0,00
27A	0,05	0,00	0,95	27A	0,80	0,20	0,00
28A	0,10	0,03	0,87	28A	0,86	0,14	0,01
29A	0,04	0,00	0,96	29A	0,84	0,16	0,00
30A	0,00	0,01	0,99	30A	0,91	0,09	0,00
31A	0,00	0,05	0,95	31A	0,89	0,11	0,00
32A	0,03	0,03	0,94	32A	0,93	0,07	0,00
33A	0,00	0,00	1,00	33A	0,95	0,05	0,00
34A	0,00	0,33	0,67	34A	0,86	0,14	0,00
35A	0,00	0,00	1,00	35A	0,74	0,26	0,00
36A	0,19	0,19	0,62	36A	0,66	0,32	0,03
37A	0,03	0,03	0,94	37A	0,81	0,19	0,00
38A	0,03	0,03	0,94	38A	0,79	0,21	0,00
39A	0,08	0,08	0,85	39A	0,74	0,26	0,00
40A	0,00	0,02	0,98	40A	0,84	0,16	0,00
41A	0,05	0,14	0,81	41A	0,88	0,13	0,00

Appendix II

Geometrical and topological data from BC1, BC2 and BC3, derived with NetworkGT.

BC1																							
Circumferenc	Area (m2 E	I	X	Y	No. Nodi	No. Branche	No. Lines	No. Connectio	Connect/Lin	Average Line Length (m)	Average Branch Length (m)	Connect/Branch	Branch Freq	Line Freq	NcFreq	1D Intensity	2D Intensity (m-1)	Dimensionless Inten	C - C	C - I	I - I	Total Trace Length (m)	
77,78141	35,831	341	180	70	2987	3237	4710,5	1583,5	3057	3,86107	0,38921	0,13084	1,96179	131,46432	44,19356	85,31715	0	17,20065	2,25051	4399,5	306	5	616,3167
Block analysis																							
Average block size																							
min																							
max																							
Block proportion																							
BC2																							
Circumferenc	Area (m2 E	I	X	Y	No. Nodi	No. Branche	No. Lines	No. Connectio	Connect/Lin	Average Line Length (m)	Average Branch Length (m)	Connect/Branch	Branch Freq	Line Freq	NcFreq	1D Intensity	2D Intensity (m-1)	Dimensionless Inten	C - C	C - I	I - I	Total Trace Length (m)	
71,41839	40,4182	40	127	34	1235	1396	1984	681	1269	3,72687	0,402	0,13798	1,93599	49,08686	16,84887	31,39679	0	6,77324	0,9346	1850,5	125,5	8	273,76178
Block analysis																							
Average block size																							
min																							
max																							
Block proportion																							
BC3																							
Circumferenc	Area (m2 E	I	X	Y	No. Nodi	No. Branche	No. Lines	No. Connectio	Connect/Lin	Average Line Length (m)	Average Branch Length (m)	Connect/Branch	Branch Freq	Line Freq	NcFreq	1D Intensity	2D Intensity (m-1)	Dimensionless Inten	C - C	C - I	I - I	Total Trace Length (m)	
37,64876	15,9403	114	112	128	950	1190	1737	531	1078	4,06026	0,36672	0,11211	1,93552	108,969	33,31177	67,62728	0	12,21609	1,3695	1576	158	3	194,72829
Block analysis																							
Average block size																							
min																							
max																							
Block proportion																							